Development of Fast Neutral Particle Diagnostics and Study of Suprathermal Ion Behaviors in LHD Plasmas

Evgeny Alexandrovitch VESHCHEV

Doctor of Philosophy

Department of Fusion Science
School of Physical Sciences
The Graduate University for Advanced Studies
Japan
2007

ABSTRACT

Analysis of energy-resolved spectra of neutral particles escaped from plasma can provide important knowledge about ion confinement and ion distribution function during different types of plasma heating such as neutral beam injection (NBI), ion cyclotron heating (ICH) or electron cyclotron heating (ECH). Such knowledge is very important for the successful development of a fusion reactor. Effective ion heating and good fast ion confinement are essential for ignition. Compared with tokamaks, studying the fast particle confinement properties in heliotrons is more complex mainly due to more complex magnetic configuration. Such a complex 3D geometry, e.g. of the Large Helical Device (LHD), may lead to appearance of additional types of confined particles (such as helically trapped particles), additional confinement effects (presence of loss-cones) and may result in more complicated drift motions. For studying fast ion confinement properties in plasma, a variety of neutral particle analyzing diagnostics have been developed on modern fusion devices. On LHD these are one-chord Compact Neutral Particle Analyzer (CNPA) and six-chord Silicon-Detector NPA (SDNPA), *etc*. E || B type CNPA utilizes one array of 40 detectors and measures energy and time resolved neutral particle fluxes in the energy range 1-170 keV. CNPA can be used in a combination with Tracer Encapsulated Solid Pellet (TESPEL) injector. Sightline of CNPA is very close to the nominal TESPEL trajectory, and thus active localized measurements can be made by the pellet charge exchange method. SDNPA can provide the measurements in the energy range 25-4000 keV and the aim of it is to make angle-resolved passive measurements of fast particles.

According to some theoretical estimations, in heliotron devices the transition particles may be lost from the confinement region through loss cones. The loss cones of fast particles from LHD plasma could not be measured so far by the existing diagnostics mainly due to the poor angular resolution (to make angle resolved measurements either a long time discharge or several shots with exactly similar parameters are required). To clarify the situation with loss-cones and to improve the angular resolution versus the existing SDNPA analyzer, a novel diagnostic with a much better angular resolution is required. The overview of currently used NPA diagnostics on tokamaks and heliotrons will be made in the Introductory chapter I. Among the preceding multi-sightline NPA systems used on magnetic confinement fusion devices the maximum sightline NPA systems with 6 chords of view are on LHD (currently operating SDNPA) and on former TFTR (discontinued). Thus a novel 20-sightline diagnostic based on a Angular Resolved Multi-Sightline NPA (ARMS-NPA) described in this Ph.D. thesis may become a new powerful tool in fast ion physics investigations. It can provide energy-, angle-, and time-resolved spectra of escaped fast neutral particles from the plasma. In addition to that a precise radial scan of the plasma column can be realized. The data

obtained by this new ARMS-NPA diagnostic in addition to CNPA and SDNPA experiments will help in understanding of fast particle physics in helical systems.

First measurements by ARMS-NPA diagnostic with real plasma have been made on LHD for a variety of plasma heating conditions. Angularly resolved measurements were made for co-, counter- and perpendicularly directed NBI, for ICRH and ECH regimes. Measurements were made for a wide range of varied plasma parameters such as electron density, magnetic axis position, positive and negative magnetic field directions, magnetic field strength. Obtained data demonstrate angular dependence of fast particle distribution on the type of heating and plasma parameters. Magnetic axis shift effect on the loss-cones has been noticed. Inward shifted magnetic axis configuration lead to improved fast ion confinement and uniform angular distribution (disappearance of the loss-cone).

Since the naturally occurring charge exchange neutral particle source is not localized in contrast to the diagnostic neutral beam or pellet charge exchange methods, the correct interpretation of such measurements in a complex toroidal asymmetric geometry requires a careful numerical modeling of the neutral flux formation and the knowledge of the charge-exchange target distributions, relevant cross sections and the magnetic surface structure. The measured chordintegral neutral flux calculation scheme for the LHD magnetic surface geometry is given. Calculation results are shown for measurable atomic energy spectra corresponding to heating-induced fast ion distributions from simplified Fokker-Planck models. The behavior of calculated and experimental suprathermal particle distributions in NBI and ICRF heated plasmas is discussed in the context of the experimental data interpretation. The geometry effect on the measured spectra interpretation is discussed. Results of experimental measurements are also compared with simulation results made by different codes with taking fast particle orbits into account.

TABLE OF CONTENTS

1. Introduction

1.1 OVERVIEW of NPA DIAGNOSTICS

Analysis of energy-resolved spectra of neutral particles escaped from plasma can provide important knowledge about ion confinement and ion distribution function during different types of plasma heating such as neutral beam injection (NBI), ion cyclotron heating (ICH) or electron cyclotron heating (ECH). Understanding of the fast particle confinement in plasma is one of the key necessities for the successful development of a fusion reactor. For this purpose several advanced diagnostics such as Compact Neutral Particle Analyzer (CNPA) [1], Time-Of-Flight Neutral Particle Analyzer (TOF-NPA) [2] and Silicon Detector - based Neutral Particle Analyzer (SDNPA) [3] have been developed on Large Helical Device (LHD).

40 channel CNPA has only one fixed chord of observation and is intended primarily for active localized measurements and works in combination with Tracer Encapsulated Solid Pellet (TESPEL) injector [4]. In addition to that it can be used for passive neutral flux measurements. CNPA utilizes only one detector array and measures only energy resolved particles in the energy range 1÷170keV (Fig.1).

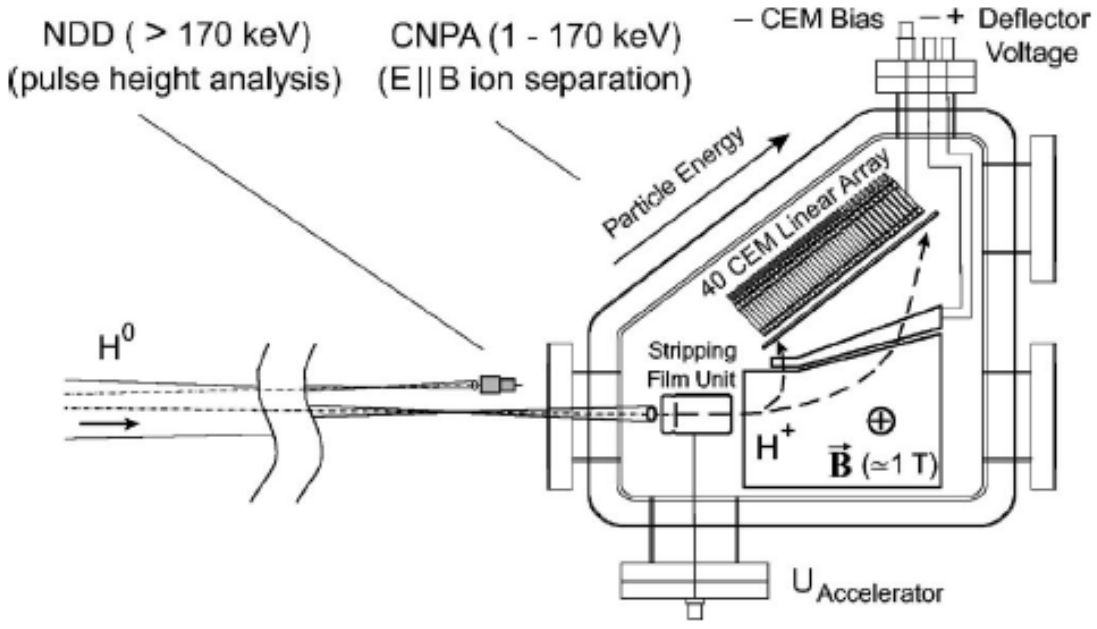

Fig.1 Measurement of escaping neutral particle energy spectra with CNPA (1÷170keV) and the observable energy range extension by neutral diamond detector NDD placed in the inlet duct near the viewing cone vertex.

Similar principle of fast particle measurements is used on Joint European Torus (JET) neutral particle analyzer [5]. The neutrals emitted from plasma are ionized in a gas stripping cell. Generated ions be means of magnetic field **B** and parallel to it electric field **E** are analyzed both in energy and mass (Fig.2). Every analyzer has two rows of 10 detectors each. They are used to detect both H and D in the same shot in this analyzer. Range of possible measured energies for H atoms are in range 0.3 - 320keV and for D atoms 0.15 – 160keV. The whole NPA diagnostic consists of 5 analyzers, four of them are mounted on a vertical tower Fig.3. Two of the analyzers can be rotated in poloidal direction as it is shown on Fig.3 and the whole set of 4 analyzers ca be rotated in toroidal direction. The fifth analyzer was installed in another location with a line-of-sight near to the last closed magnetic surface. From 1989 NPA tower was removed and a single NPA was installed at the bottom of the machine with an almost vertical line of sight to the plasma center.

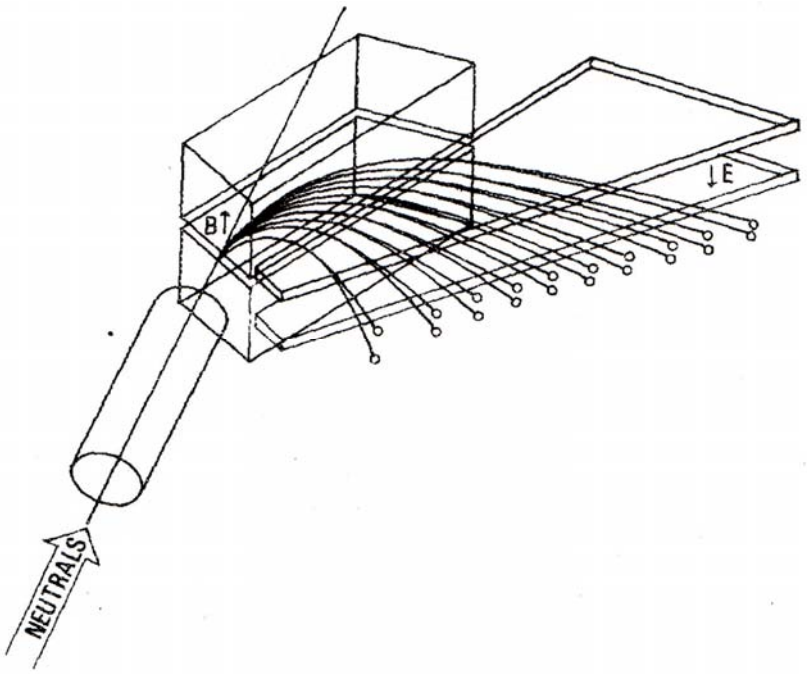

Fig.2 Schematic analyzer concept.

One of NPA system on National Spherical Torus Experiment utilizes **E**‖**B** spectrometer [6] which measures the energy spectra of H minority and bulk D species simultaneously with 39 energy channels per mass species and can scan plasma over a wide range of tangency angles as it is shown on Fig.4. The disadvantage of this diagnostic is the impossibility to obtain the whole plasma column scan simultaneously.

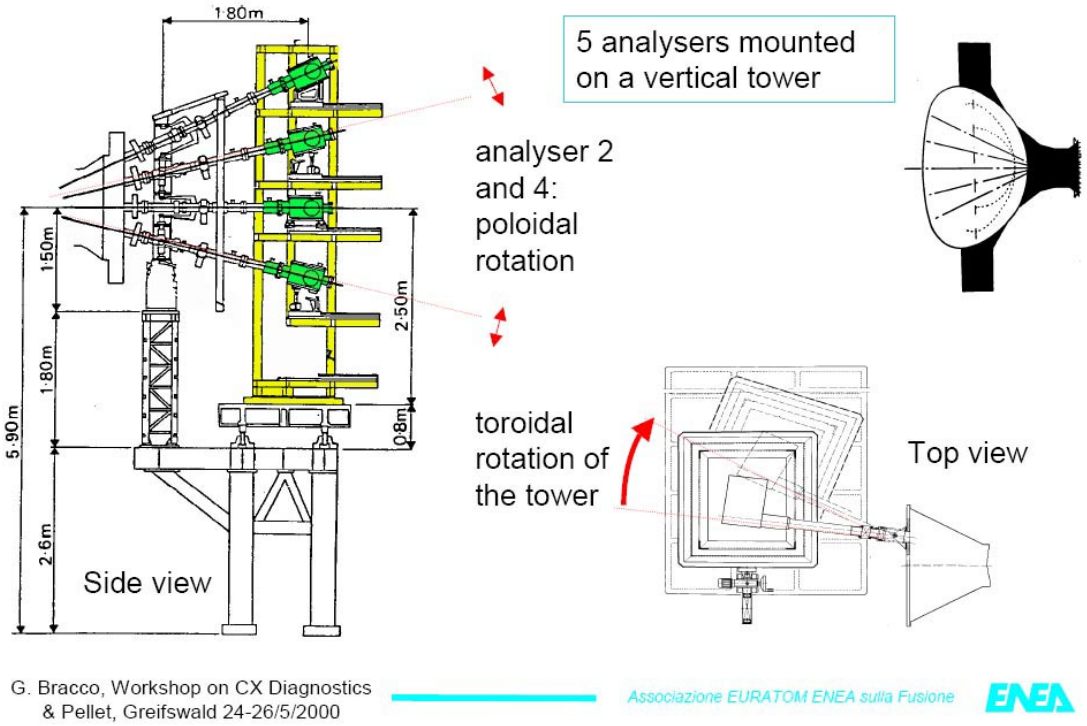

Fig.3 Side and top view of the JET NPA system.

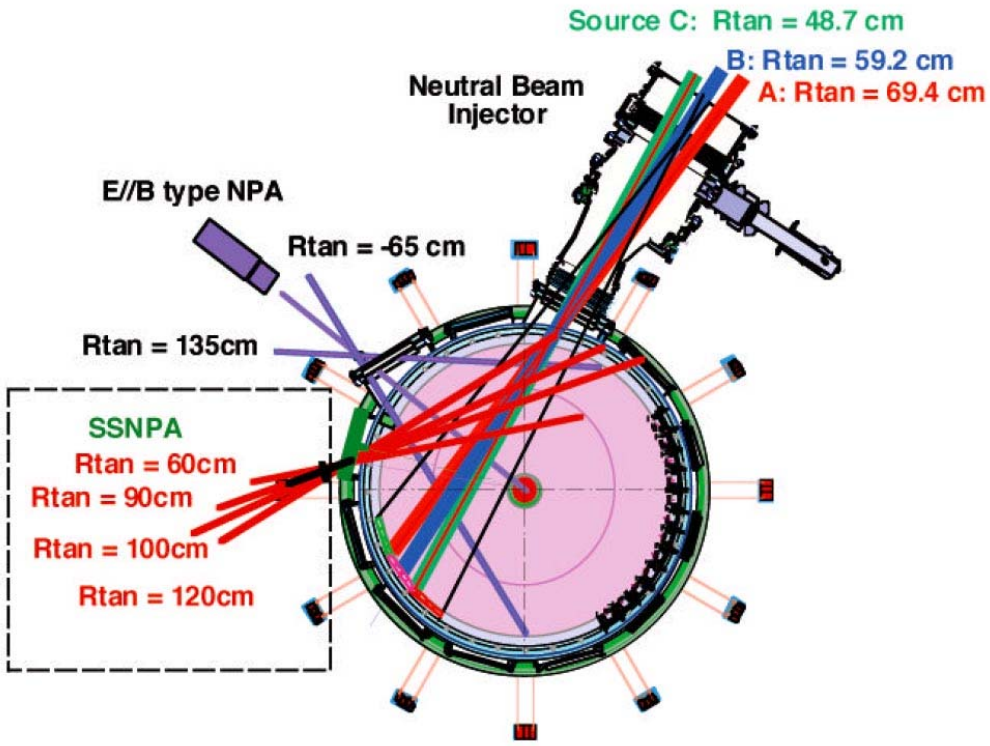

Fig.4 Possible viewing chords of **E**$\|$**B** spectrometer are shown with viewing chords of SSNPA array and injection lines of NB on NSTX.

Another NPA system on National Spherical Torus Experiment is based on a solid state detector (SSNPA) and consists of four viewing chords through a common vacuum flange [7]. The tangency radii of the viewing chords are 60, 90, 100 and 120 cm (Fig.4). They view across NBI lines at co-going ions. Such a diagnostic is able to scan plasma only in 4 definite directions without the possibility of scanning the plasma column.

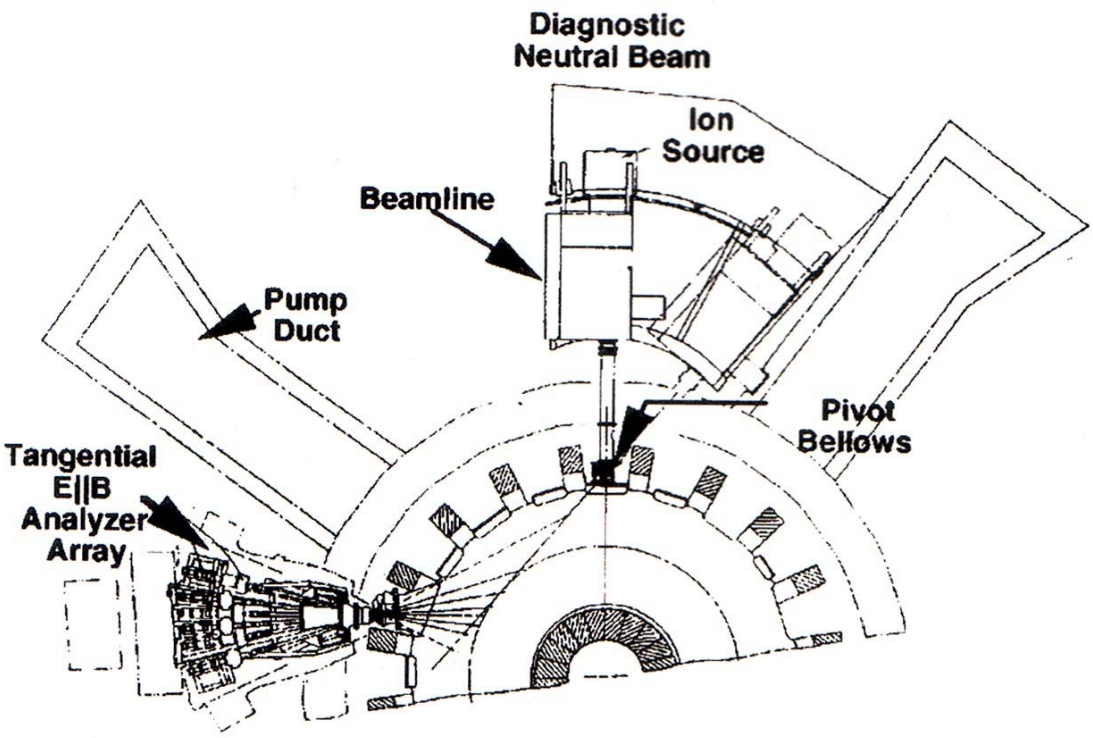

Fig.5 Layout of the tangential charge exchange array on TFTR (top view). Also shown is the diagnostic neutral beam, which can be scanned in the mid-plane from radial injection to 40º toroidally into the field of view of the horizontal charge exchange array.

Tokamak Fusion Test Reactor (TFTR) also utilizes $\mathbf{E} \| \mathbf{B}$ mass and analyzer in the range $0.5 \leq A(\text{amu})E(\text{keV}) \leq 600$ and its design enables simultaneous mass-resolved measurements of H, D and T energy spectra during a single discharge [8]. The Charge Exchange Neutral Analyzer (CENA) diagnostic consists of two autonomous analyzer systems and one shared Diagnostic Neutral Beam (DNB). The first system is has a fan-like field of view along six sightlines in the equatorial plane and can make plasma scan in both horizontal and vertical direction (Fig.5). The second system measures perpendicular ion energy distribution and along 12 vertical chords spaced approximately equidistant across the torus minor diameter (Fig.6).

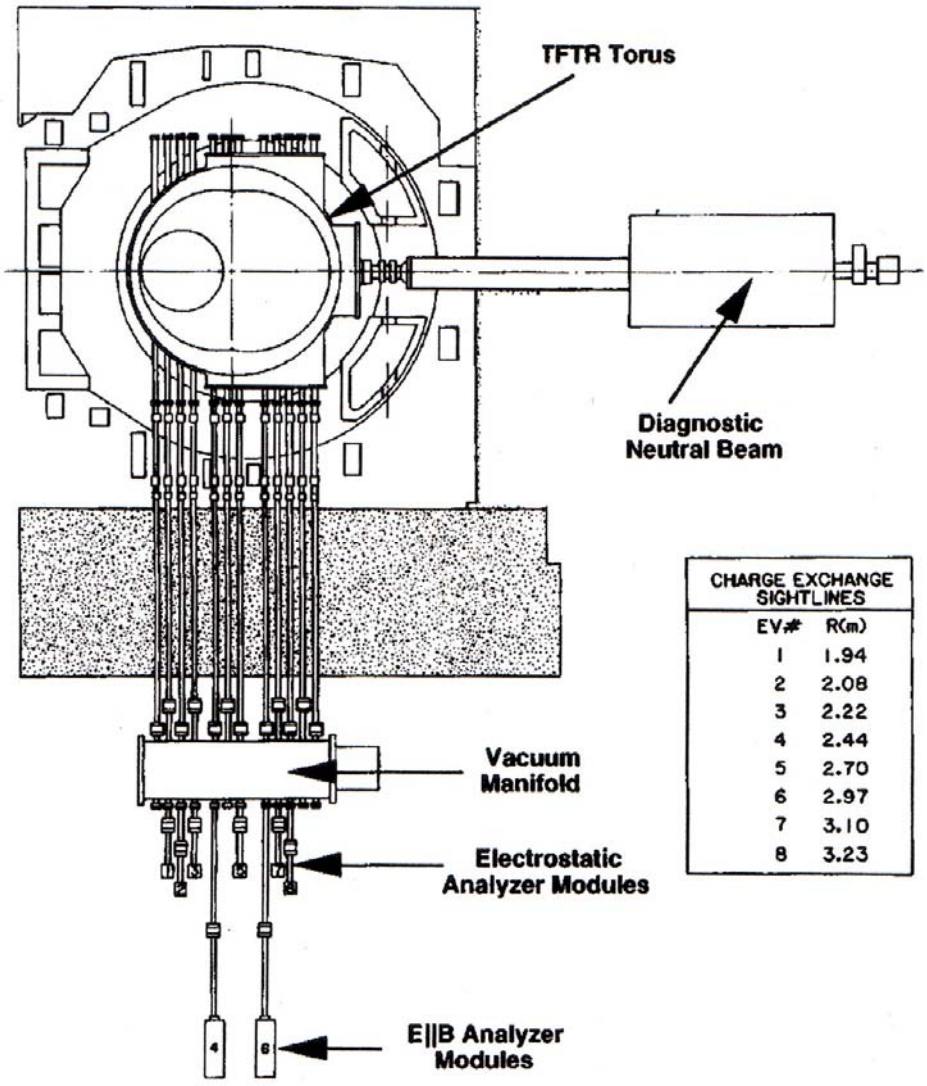

Fig.6 Elevation layout of the vertical charge exchange array on TFTR. This array consisted of two $\mathbf{E} \| \mathbf{B}$ spectrometers and six compact electrostatic analyzers whose sightlines intersected the diagnostic neutral beam when it was oriented for radial injection.

NPA diagnostic proposed for ITER consists of neutral beam diagnostic injector combined with 3 couples of neutral particle analyzers (NPA) (Fig. 7) [9]. The diagnostic beam is injected into the plasma almost horizontally perpendicular to the plasma axis. Each NPA couple consists of one middle energy NPA and one MeV energy NPA. They are placed along the same axis one after another in such a way that the flux of neutrals passing through the first (middle energy) NPA enters the second (MeV energy) one. Three units of NPA couples view the plasma through a vertical port. Their lines of sight intersect the diagnostic beam at the distance of 0.56m, 1.12m

and 1.62m from the plasma edge to have the measurements at three different points along the radius. One more couple of NPA's with the line of sight along the major radius crossing the plasma centre has been added.

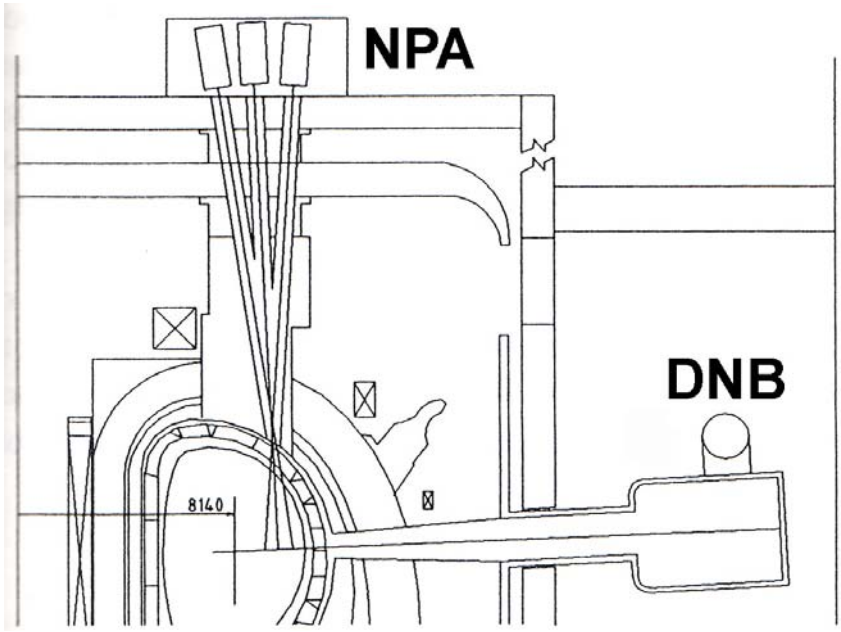

Fig.7 Set up of NPA diagnostics proposed in [15].DNB – diagnostic neutral beam injector.

A combination of horizontally scannable DNB and NPA [10] has been used on the compact helical system (CHS) [11,12] to provide information on whether the energetic ions with different pitch angle are confined in the plasma or immediately lost. The DNB can be scanned horizontally to vary the pitch angle of ions injected as test particles. The pitch angle of the confined energetic ions is measured with the NPA. The DNB and NPA systems are installed at the outboard side on CHS. Both systems are on the equatorial plane and are separated by 180° in the toroidal direction (Fig. 8). The beam line can be scanned from perpendicular injection to tangential injection both in the co- and counter-direction with a pivot point of R=1.58 m (the plasma major and average minor radii are R=1 m and a=0.2 m, respectively). The DNB beam line is scanned near the loss cone boundary from the tangential radius (R_T^{DNB}) of 17–31 cm. Injected energetic ions are measured with the NPA at tangential radii (R_T^{NPA}) from 18 to 74 cm. The DNB and NPA systems can be scanned horizontally by 0.1° increments using a pulse motor system. Beam energy (E_b) and extracted current of the positive beam (I_b) are 28–40 keV and 2–3 A, respectively.

The DNB divergence angle measured with a calorimeter is 0.83° –95° at *Eb* of 30–36 keV. The beam radius at the focal point is 4.2–4.9 cm, and the averaged minor radius of CHS plasma is typically 20 cm. The NPA system consists of an electrostatic deflection plate and 16 micro-channel plates. By changing the voltage of the parallel plate of the NPA, the energy spectrum in the range of 0.1–50 keV can be measured with a maximum count rate of 1×10^6 counts/s.

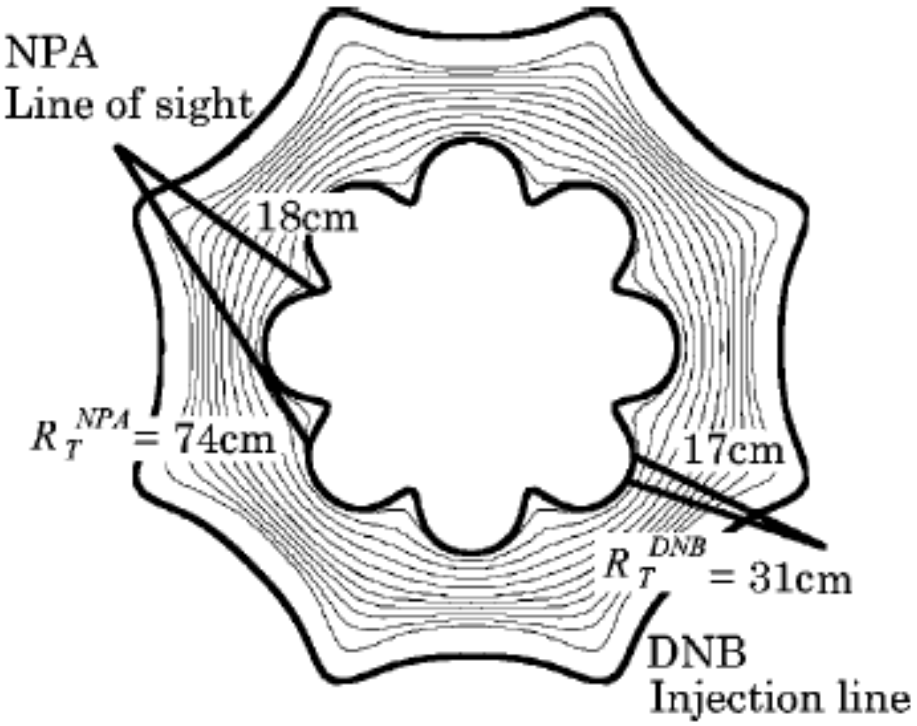

FIG. 8. Experimental set up of the DNB and NPA in CHS. The beam line and NPA line of sight on the equatorial plane are plotted.

To investigate the behavior of fast ions in Heliotron J [13], a charge-exchange (CX) neutral particle analyzer (NPA) system has been installed [14]. The experimental setup of the NBI and CX-NPA system is shown in Fig.9. Hydrogen beams are co-injected in the tangential direction with a maximum acceleration voltage of 30 kV and a maximum injection power of 0.7 MW. Here, the co-injection is defined as parallel to the equivalent toroidal plasma current. The angles between the magnetic axis and the beam lines of the NBI system are from 150 to 175 deg. The ion energy distribution functions are measured with a CX-NPA system. This CX-NPA is an $\mathbf{E}\|\mathbf{B}$-type one that can measure the energy spectra of hydrogen and deuterium ion species simultaneously with ten energy channels per mass species. The

energy ranges are from 0.4 to 80 keV for hydrogen and from 0.2 to 40 keV for deuterium. The energy resolution is from 4 to 10%. The viewing area of the CX-NPA is 6 or 12 mm in the vertical direction and 58 mm in the horizontal direction at the plasma center. In order to investigate the pitch angle distribution of the fast ions in plasmas, the CX-NPA system can change the measuring angle horizontally φ_{NPA} and vertically θ_{NPA} simultaneously with the range of φ_{NPA} from -10 to +18 deg and θ_{NPA} from -3 to +10 deg. The CX-NPA system can observe the pitch angle in the range from 98 to 135 deg on the magnetic axis in the standard configuration. As φ_{NPA} changes 1 deg, the pitch angle of detected particles and observed point changes about 1.5 deg and 12 mm, respectively.

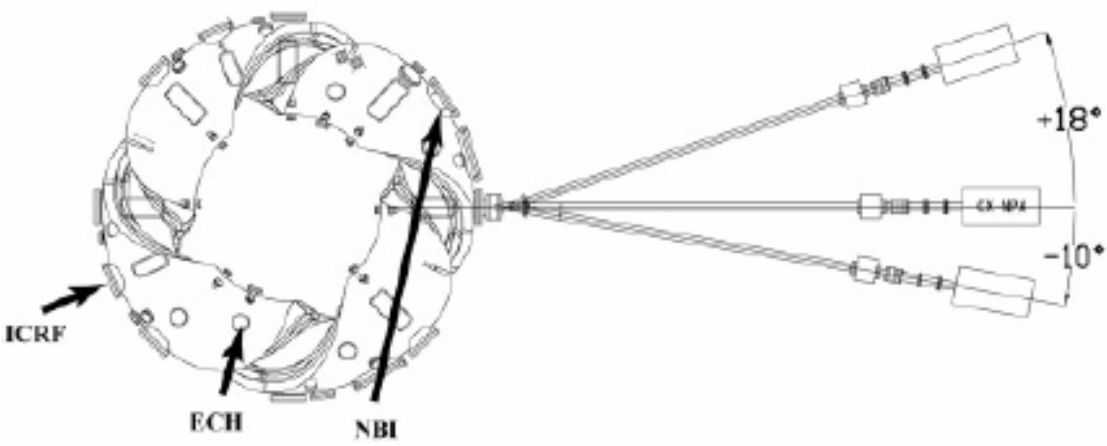

Fig.9 Top view of the Heliotron J and CX-NPA system.

The Mega Ampere Spherical Tokamak (MAST) is equipped with 78channel dual mass NPA diagnostic Fig.10 [15] which measures particles in the energy range $0.5<E(\text{keV})/A(\text{amu})<70$. The NPA spatial scanning system has a tangency range from R_{NPA}~ 133cm in the co-beam direction to R_{NPA}~ -46cm in the counter-beam direction, and can view both NBI lines which are injected at a tangency radius Rtan, of 70cm as shown in Fig.10. Although such a system can scan plasma in quite a wide range of angles, it cannot provide the simultaneous scan of the whole plasma in from directions of equatorial plane.

On Alcator C-Mod for measuring of energetic hydrogen minority ions with energies ~ 50 – 350keV there is a four-channel compact neutral analyzer (CNPA) [16] based on operating small Si diode detectors in pulse-height analysis (PHA) mode.

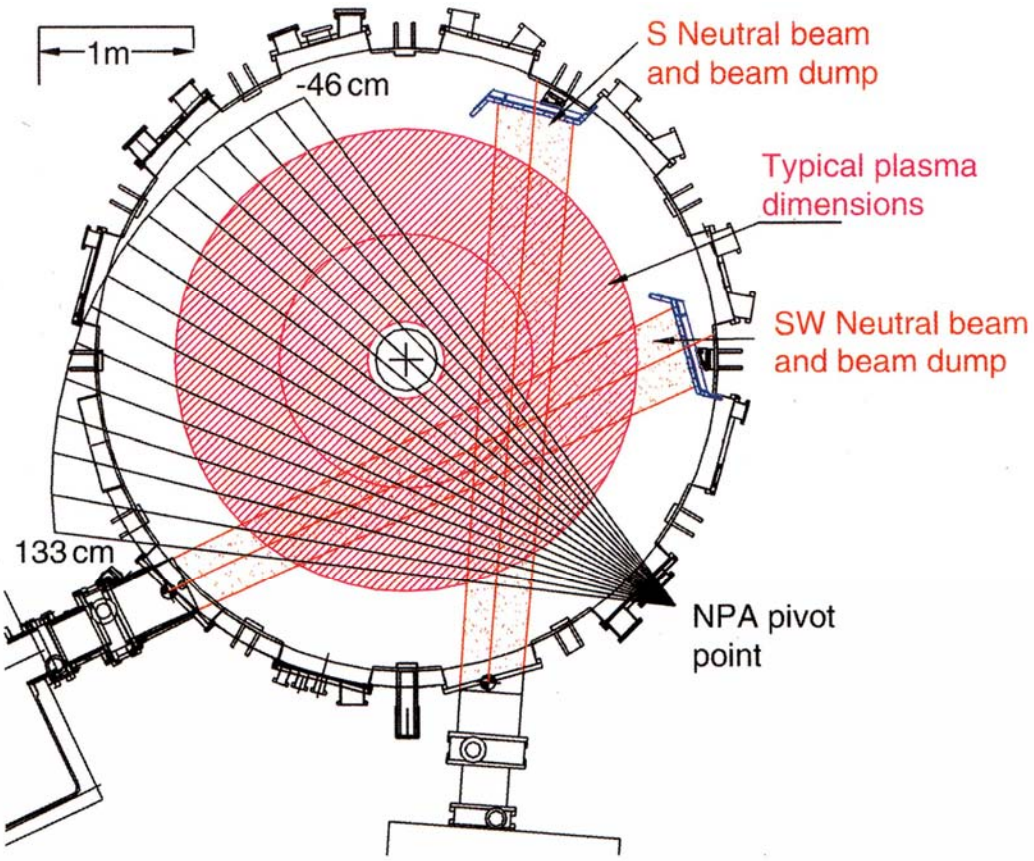

Fig.10 MAST NBI and NPA layout.

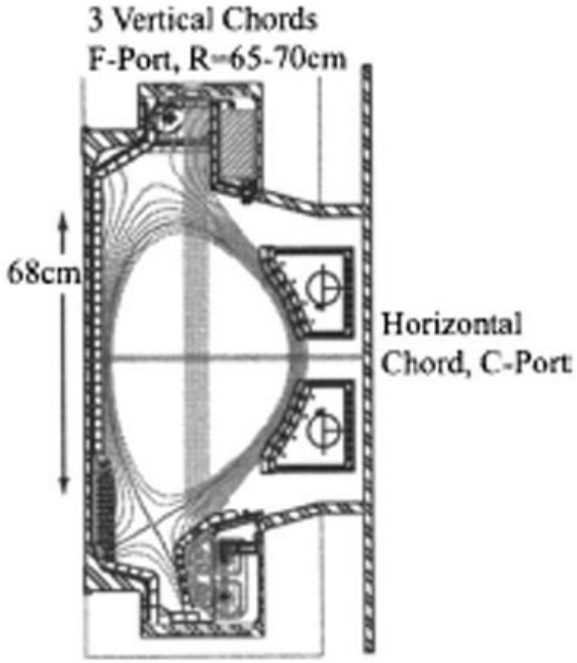

Fig.11 Schematic view of the three channel vertical detector array and the system of sightlines in plasma.

The CNPA consists of three vertical and one horizontal sightlines as it is illustrated on Fig.11. The sightlines of the diagnostic are arranged such that three vertical chords view the phase space of the neutral distribution that is predicted to be most energetic, while the remaining horizontal channel sees neutrals that should be slower.

Another system used on Alcator C-Mod for neutral measurements is a neutral particle analyzer based on the time-of-flight technique and magnetic-type neutral particle analyzer [17]. Time-of-flight NPA is mounted behind magnetic-type NPA and shares the same line of sight (Fig.12). Both of them can be scanned, poloidally down to the X point and tangentially to $R/R_0 = 0.7$.

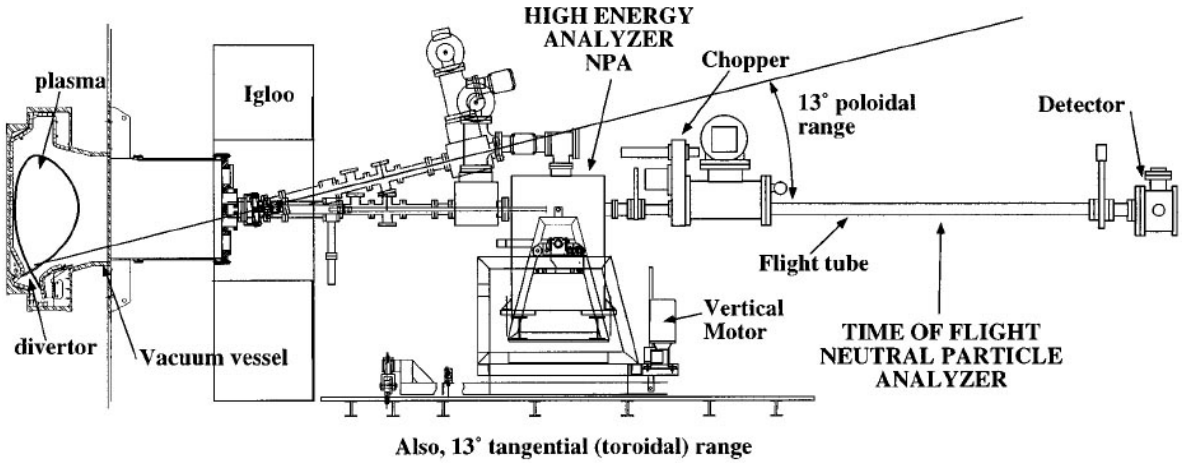

Fig.12 Schematic side view of the time-of-flight installation with the high energy neutral particle analyzer (left) on Alcator C-Mod.

Movable TOF-NPA installed on LHD made measurements along one sightline and could scan the plasma during the discharge. The pitch angle distribution from 40° to 100° can be obtained by horizontal scanning of the TOF-NPA. The disadvantage of this diagnostic is also the impossibility to obtain the whole plasma column scan simultaneously.

Another diagnostic of fast particles widely used at modern fusion devices [18-21] is based on Neutral Diamond Detector (NDD) [22-24]. The NDD has three layer structure, i.e. electrode-semiconductor (very pure natural diamond) electrode. The NDD employed in LHD [19] is a specially developed detector having a very thin graphite front electrode, which makes it possible to detect low energy particles. Incident fast particles produce electric charges inside the diamond. These charges are drawn by an externally applied bias voltage to the electrodes. The NDD is mounted

inside a stainless steel cylinder of 30 cm length to shield the detector against vacuum ultraviolet (VUV) rays and soft x rays because the NDD is sensitive to such photon radiations. In order to view the plasma, they set a circular aperture having a fixed diameter of 1 mm on the opposite end, i.e., plasma side, of the cylinder. An additional aperture whose diameter can be changed is also installed 55 cm ahead of this fixed aperture to control the neutral particle flux coming into the NDD. Two NDDs are installed on LHD. One is installed on the equatorial plane with tangential line of sight to measure ctr.-going beam ions. The distance between the NDD and the magnetic axis position is about 8.3 m in this case. Another is set on a perpendicular diagnostic port to diagnose formation of energetic ion tail produced by ICRF. A line of sight of the NDD set on a perpendicular port is shown in Fig.13. The position of the NDD is about 4.5 m below the magnetic axis position. The NDD is operated at room temperature in LHD. Because of sufficiently wide band gap (5.5 eV), it is not necessary to cool the detector to suppress thermal noise as long as we focus on detecting NB ions or ICRF-produced fast ions.

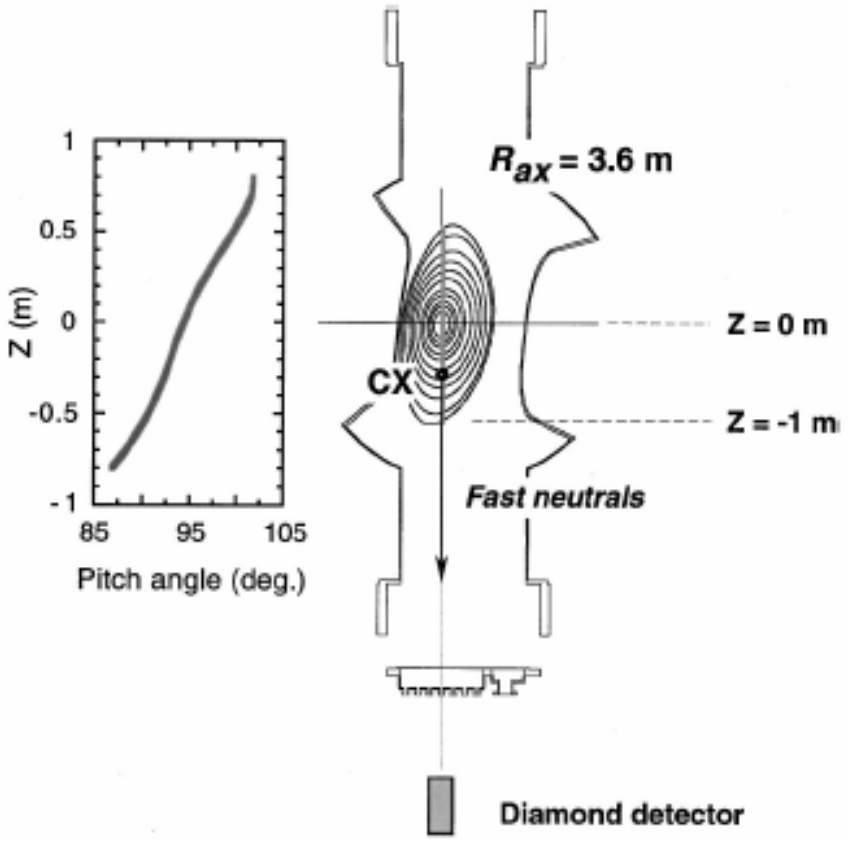

FIG. 13. Line of sight of the NDD on a perpendicular diagnostic port of LHD. The left figure shows the pitch angle distribution of fast particles detected by the NDD along the line of sight at *Rax*=3.6 m.

1.2 MOTIVATION FOR CREATING A NOVEL DIAGNOSTICS

As it was mentioned earlier LHD is equipped with SDNPA [2]. The aim of the SDNPA is to make angle-resolved passive measurements of fast particles. It consists of six separate ion-implanted silicon detectors. The horizontal angular resolution is 4.6 degrees and observable sector is 23 degrees (Fig.14). A vertically movable collimating aperture provides a full two-dimensional scan of the non-axisymmetric plasma. To make a precise scan of the plasma a long discharge or several short discharges with exactly similar conditions are required.

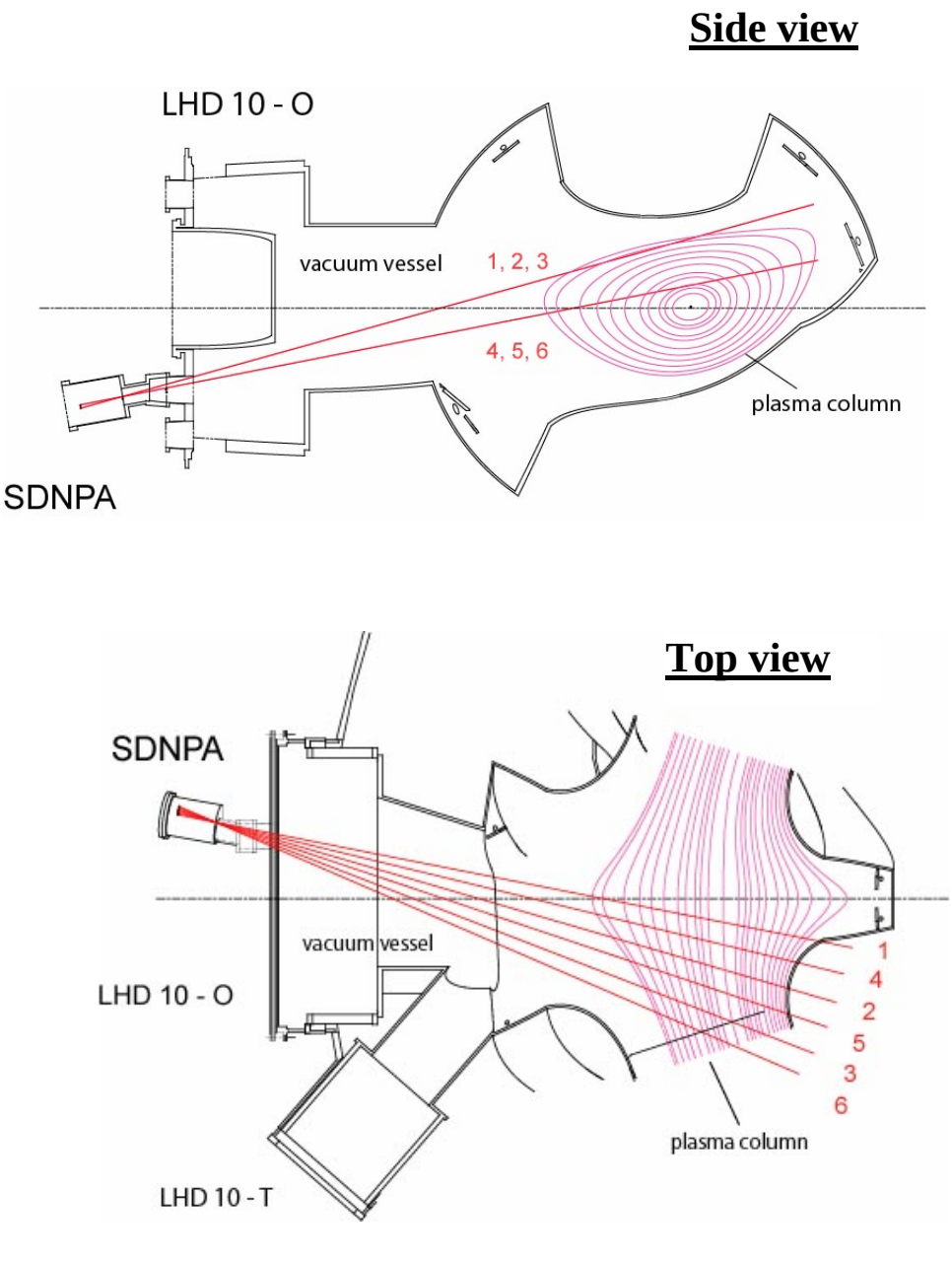

Fig.14 Side and top view of SDNPA sightlines in LHD geometry.

Although SDNPA can scan plasma by 6 sightlines, two pairs of the sightlines observe almost the same plasma regions as it can be seen from Fig.15. Detector 4 observes almost same pitch angles as detector 2. The same situation is for detector 3 and 5. Thus the angular distribution of fast particles appears to be not detailed and not complete (Fig.16).

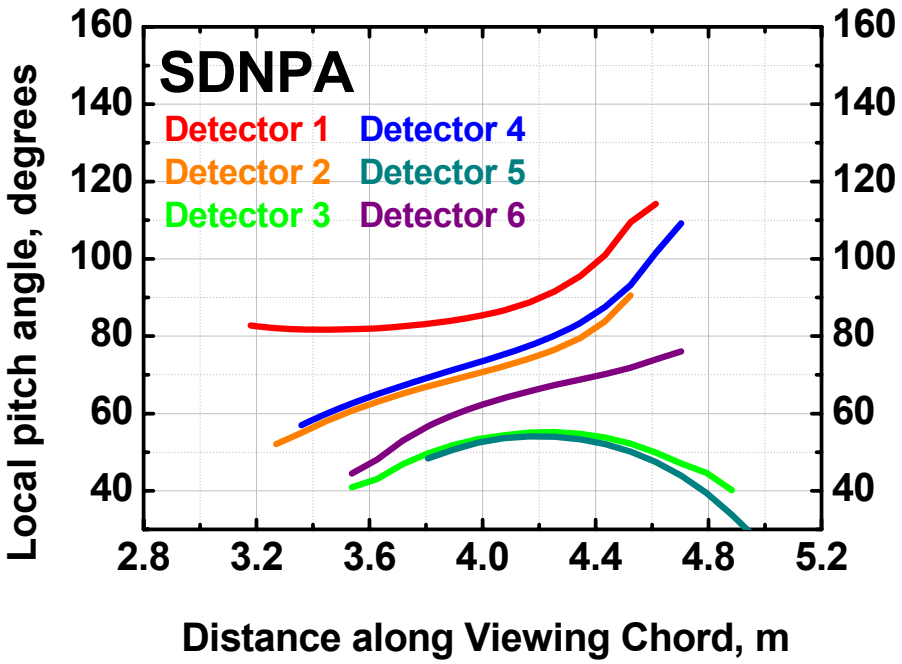

Fig.15 Pitch angle distribution along viewing chords of SDNPA.

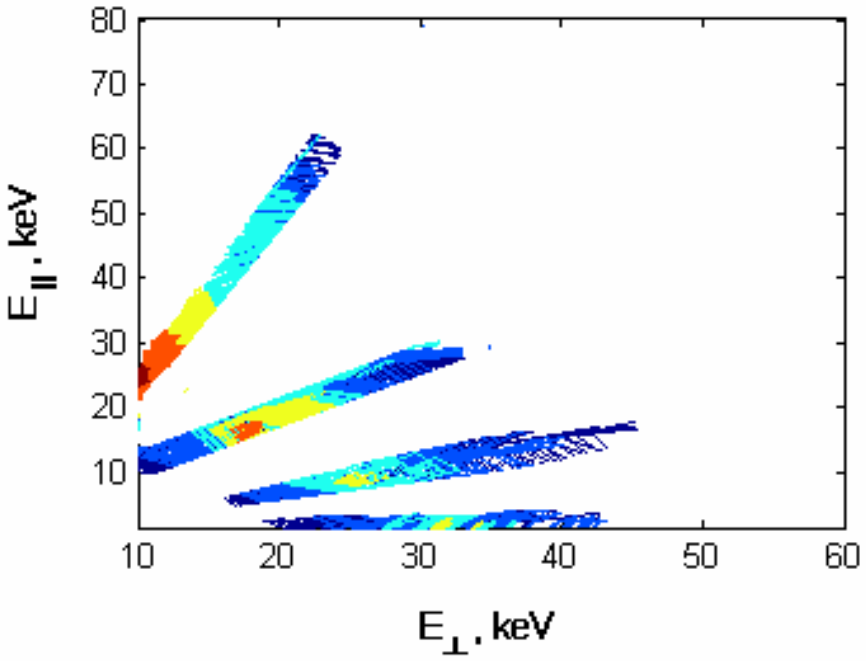

Fig.16 Energy spectrum measured along 6 SDNPA sightlines.

According to some theoretical estimations, in heliotron devices the transition particles may be lost from the confinement region through a loss cone [25] as it can be seen from Fig.17. However, recent theoretical studies predict that the loss-cone in LHD configuration is substantially reduced due to taking into account highly energetic particles outside the last closed magnetic flux surface [26].

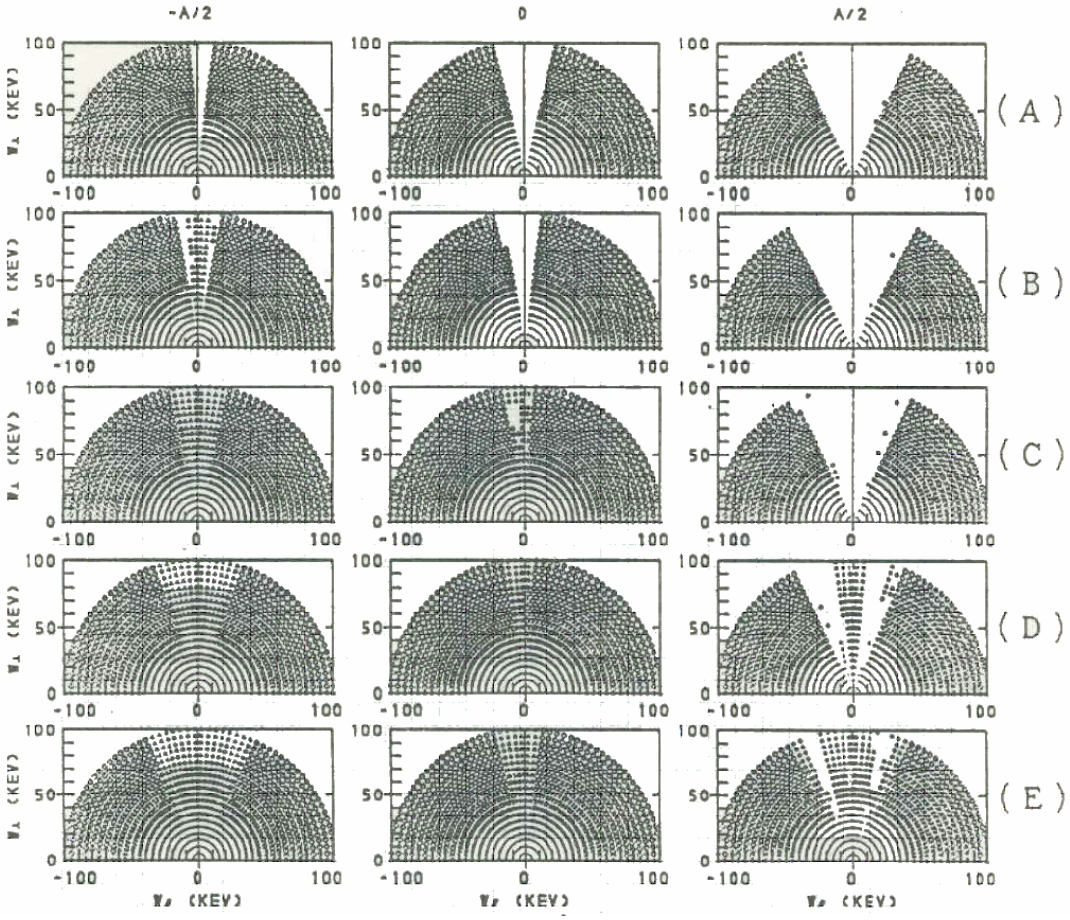

Fig.17 Typical velocity space loss regions of the heliotron configuration for different magnetic shifts, (A):5cm, (B):0cm, (C):-5cm, (D):10cm, and (E):-15cm. The maximum particle energy is 100keV and the magnetic field is 4T.

The loss cones of fast particles in LHD plasma could not be measured so far by the existing diagnostics mainly due to the poor angular resolution. To clarify the situation with loss-cones and to improve the angular resolution versus the existing SDNPA analyzer, a novel Angular Resolved Multi-Sightline NPA (ARMS-NPA) diagnostic scanning plasma by 20 sightlines has been developed. Due to significant increase of observation lines the new diagnostic should fill up the data obtained by SDNPA as it is demonstrated on Fig.18 by red lines. The range of measured pitch angles is from 60 to 160 degrees as it can be seen from Fig. 19. Local pitch angles

along sightlines for two diagnostic positions were calculated from VMEC numerical solution of 3D MHD equilibrium equations assuming nested flux surfaces [27]. Red dots of Fig.19 correspond to last closed magnetic flux surface, black dots correspond to one possible diagnostic position, blue dots correspond to the second possible diagnostic position.

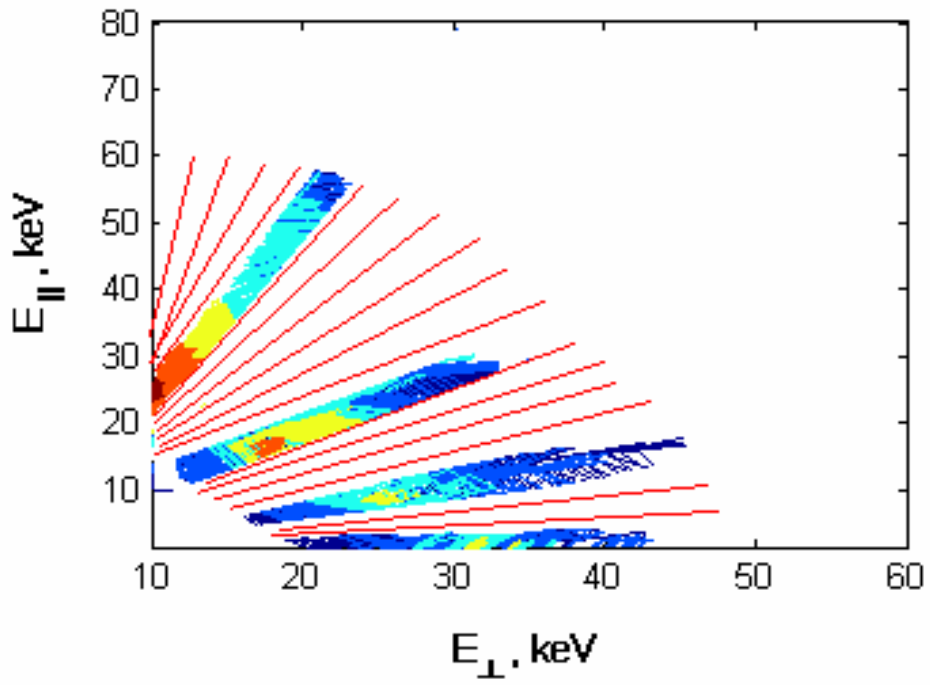

Fig.18 Blank spaces at energy spectrum measured along 6 SDNPA sightlines to be filled in by a new diagnostic.

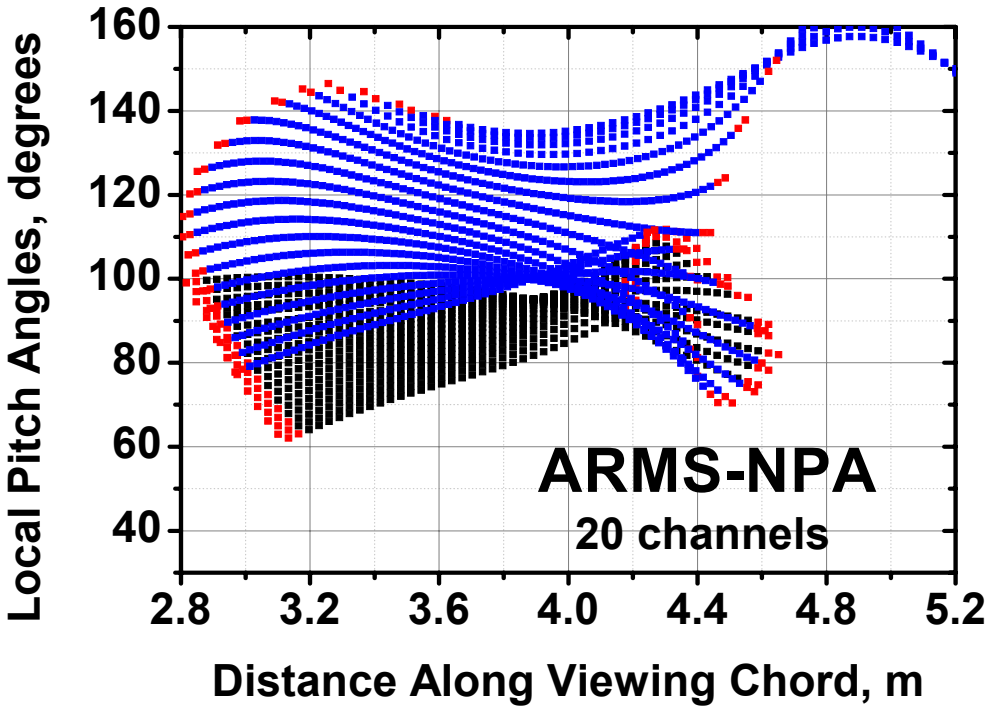

Fig.19 Pitch angle distribution along viewing chords of ARMS-NPA.

1.3 Brief Summary

Among the NPA diagnostics used on tokamaks only a few can make angular resolved measurements of fast particles along several sightlines simultaneously. For example one of NPA system used on TFTR operates six sightlines in equatorial plane which are capable of being scanned in both toroidal and vertical direction [8]. Solid state neutral particle analyzer array on NSTX consists only of four viewing chords [7]. Multi-channel SDNPA on LHD can scan plasma by six sightlines [2]. Thus in the light of multi-sightline NPA systems available to make angular-resolved measurements of fast particles a new ARMS-NPA Diagnostic with its 20 channels of scanning is going to become a powerful tool for fast particles study.

2. Novel Angular Resolved Multi-Sightline NPA Diagnostic (experimental setup)

2.1 BASIC COMPONENTS

The diagnostic is based on a linear position sensitive AXUV-20EL detector [28] consisting of 20 independent sections Fig.20. This is the first time of applying AXUV detectors for fast particle measurements in plasma devices [29]. Dimensions of every detector segment are 4.5×0.75mm (Fig.20).

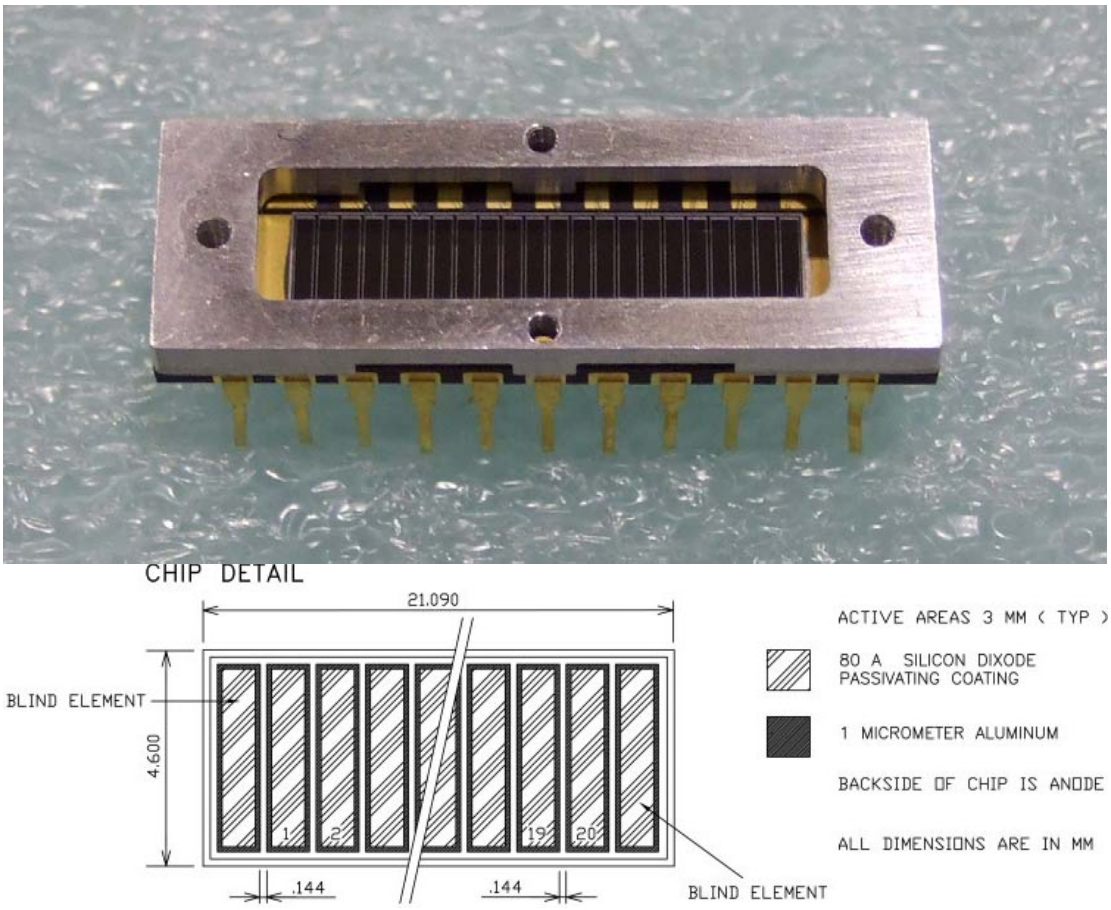

Fig.20 Photograph and drawing of utilized AXUV-20EL detector.

It can work in a high magnetic field, does not use high voltage and does not require such components as a stripping gas cell and a bending magnet. The simultaneous work of all sections enables measurements of energetic particles (>15keV) with 3keV energy resolution to be made along 20 sightlines. This detector positioned behind a 5 μm in diameter aperture serves as an angle resolved neutral particle analyzer (NPA) with an improved angle resolution (as good as 0.6 degrees

between the neighboring channels) compared to the earlier 6-chord SDNPA. Comparison of SDNPA and ARMS-NPA basic parameters are in Table1.

Table 1. Comparison of ARMS-NPA and SDNPA basic parameters.

	SD-NPA (Silicon-Detector Neutral Particle Analyzer system)	ARMS-NPA (Angular Resolved Multi-Sightline Neutral Particle Analyzer)
Amount of sightlines (spatial resolution)	6	**20**
Energy Range, keV	25 ÷ 4000	15 ÷ 1000
Energy Resolution, keV	1.8	3
Pitch Angle on Magnetic Axis, degrees	95-130	**60 ÷ 160**
Detector Size, mm^2	25x6ch	3x20ch
Detector Type	Silicon	Photodiode

The aperture is mounted on a tungsten alloy plate with a small hole to prevent the excessive X-ray influence (Fig.21). In addition to that, the detector is covered by a 100 nm aluminum foil to block the visible and ultraviolet light from the plasma.

The detector, preamplifiers and buffer amplifier are very close to LHD chamber and strong magnetic field respectively. The signal level is quite low (about 2mV after preamplifier and about 20mV after buffer amplifier) it is very sensitive to electromagnetic noise. Therefore the assembly of the detector and the preamplifiers is fixed on a copper plate cooled by liquid nitrogen to reduce the thermal noise and increase the energy resolution. This assembly is mounted on a precision rotary flange (Fig.21). This allows one to set up the direction of the sheaf of 20 sightlines to scan the plasma column readily. Any choice of the diagnostic plane is possible from the vertical to the horizontal one without warming up the detector and depressurizing the diagnostic chamber.

The diagnostic design was improved by installation of the thermocouple to monitor the temperature of the assembly with detector and preamplifiers. It was attached to the

liquid nitrogen cooled copper disk on which the detector and preamplifiers are mounted. In addition to the cooling system the buffer amplifier was positioned as close as it possible to preamplifiers outputs from the chamber and every cable between preamplifier outputs are and buffer amplifier input were covered by metal braid. Such measures could reduce energy resolution of measured signal up to 2-3keV.

The new ARMS-NPA diagnostic is equipped with a special rotary mechanism (Fig.22) which allows one freely to change a diagnostic plane (Fig.23) during experiments without depressurization of the linear detector chamber.

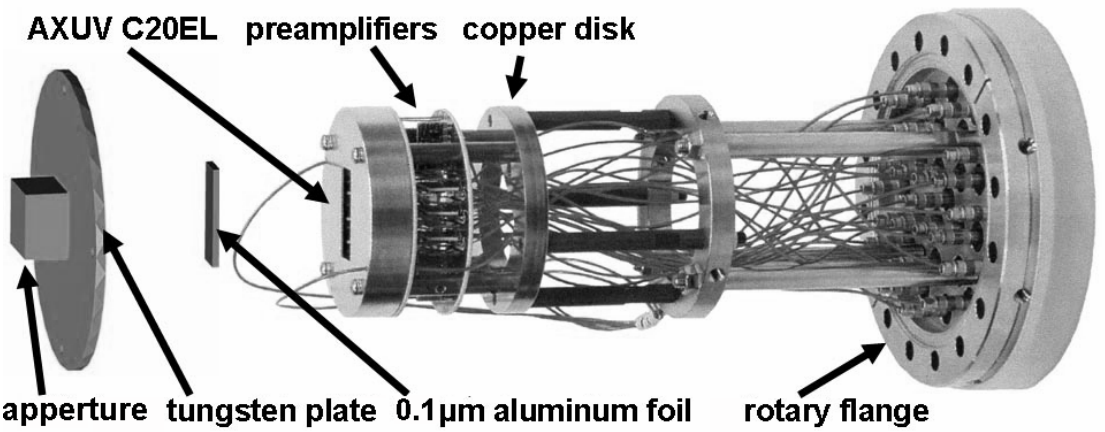

Fig.21 Diagnostic design. Basic components.

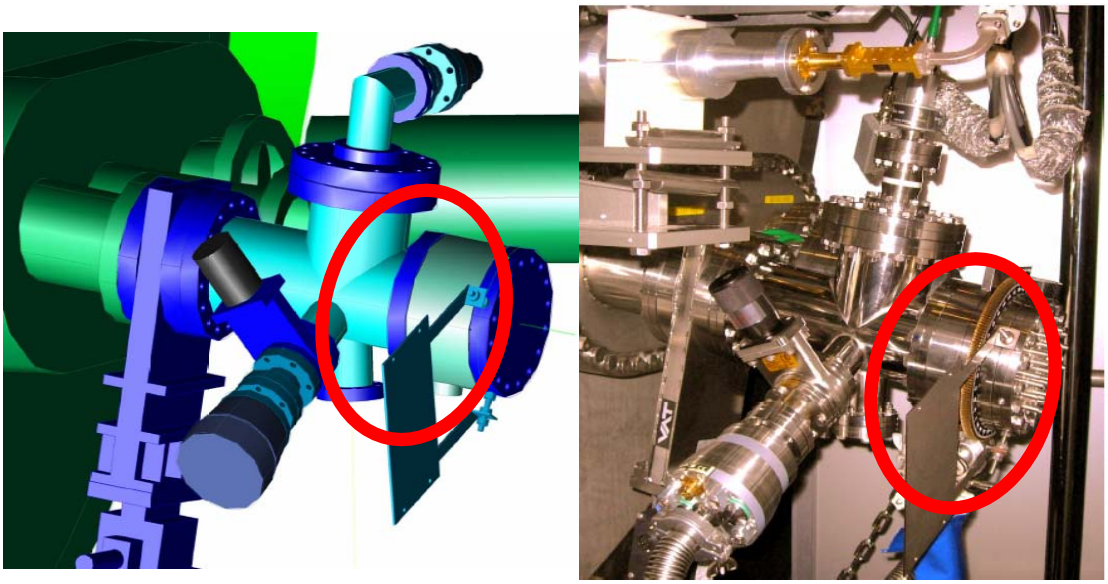

Fig.22 ARMS-NPA chamber and special rotary mechanism.

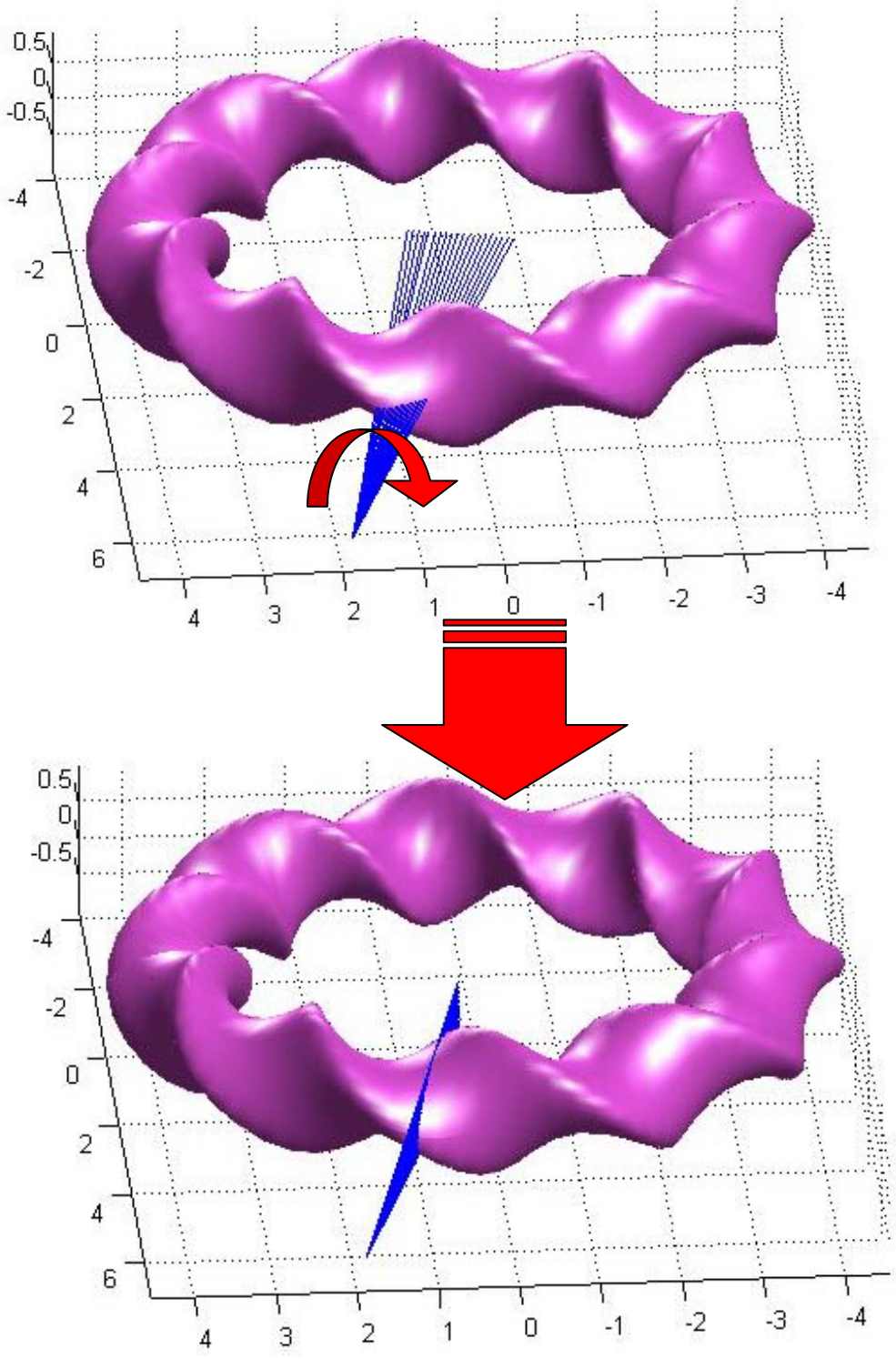

Fig.23 Schematic view of sightlines for horizontal and vertical plasma scan.

2.2 DATA ACQUISITION SYSTEM

ARMS-NPA data acquisition structure is similar to SDNPA one, *i.e.* an incident particle of energy E (eV) incident on any of the detector sections produces a charge pulse of $E/3.63$ electron-hole pairs; this charge is collected and converted to a voltage pulse, amplified by a charge-sensitive resistive feedback preamplifier and a buffer amplifier (located outside of detector chamber), shaped by a fast pulse amplifier, processed by a PHA ADC and stored in a histogramming memory module (Fig.24). All 20 detector segments have their own data acquisition system.

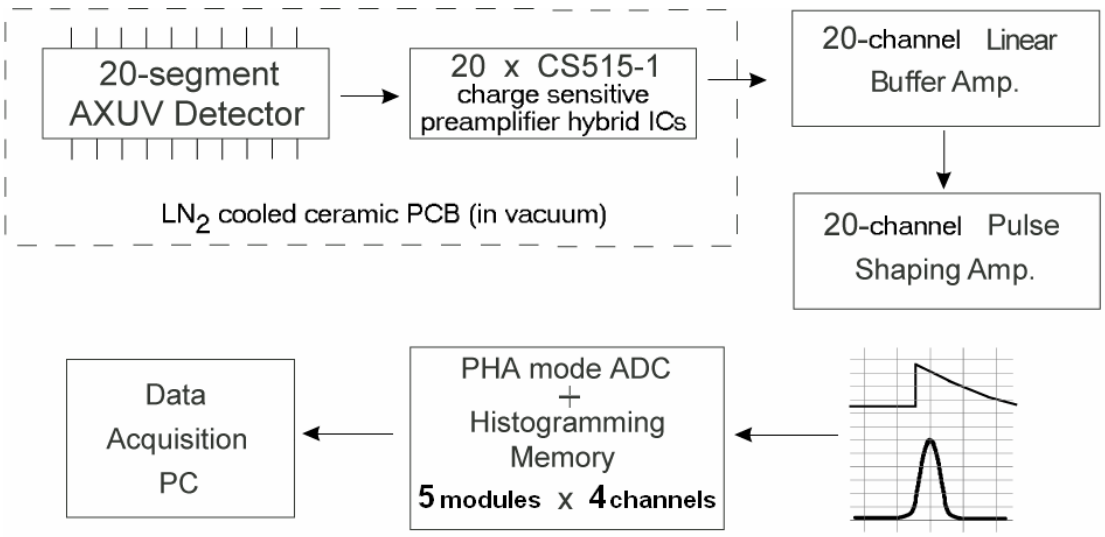

Fig.24 Data acquisition system of every detector segment.

Two types of preamplifiers can be used for diagnostic of fast particles where the pulse from every particle should be processed – Transistor Reset Preamplifier (TRP) and Resistive Feedback Preamplifier (RFP). Their scheme and shape of pulses are presented on Fig. 25. Current diagnostic of fast particles utilizes RFP.

Minimum possible value of the shaping amplifier time constant was 1μs. Such a time constant appeared to be not sufficient for a quite a wide range of plasma conditions with a high flux of fast particles emitted from plasma and entering the detector. Examples of low flux case with satisfactory time constant and of high flux case with not sufficient time constant of the shaping amplifier are shown on Fig.26.

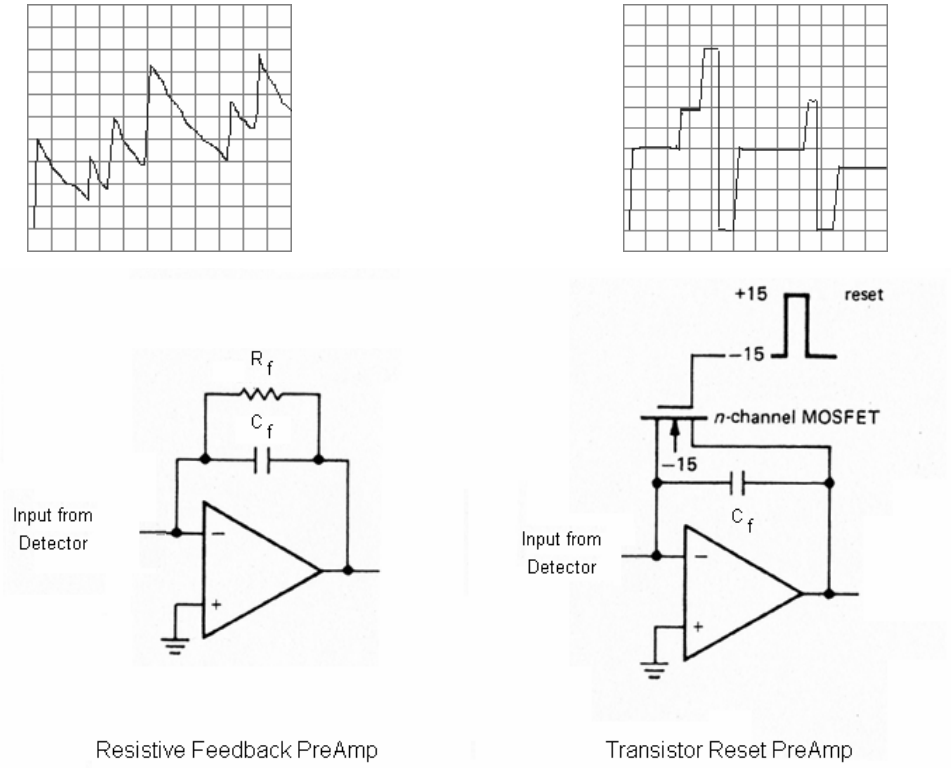

Fig.25 Electrical scheme of Resistive Feedback Preamplifier (RFP) and Transistor Reset Preamplifier (TRP) together with corresponding signals.

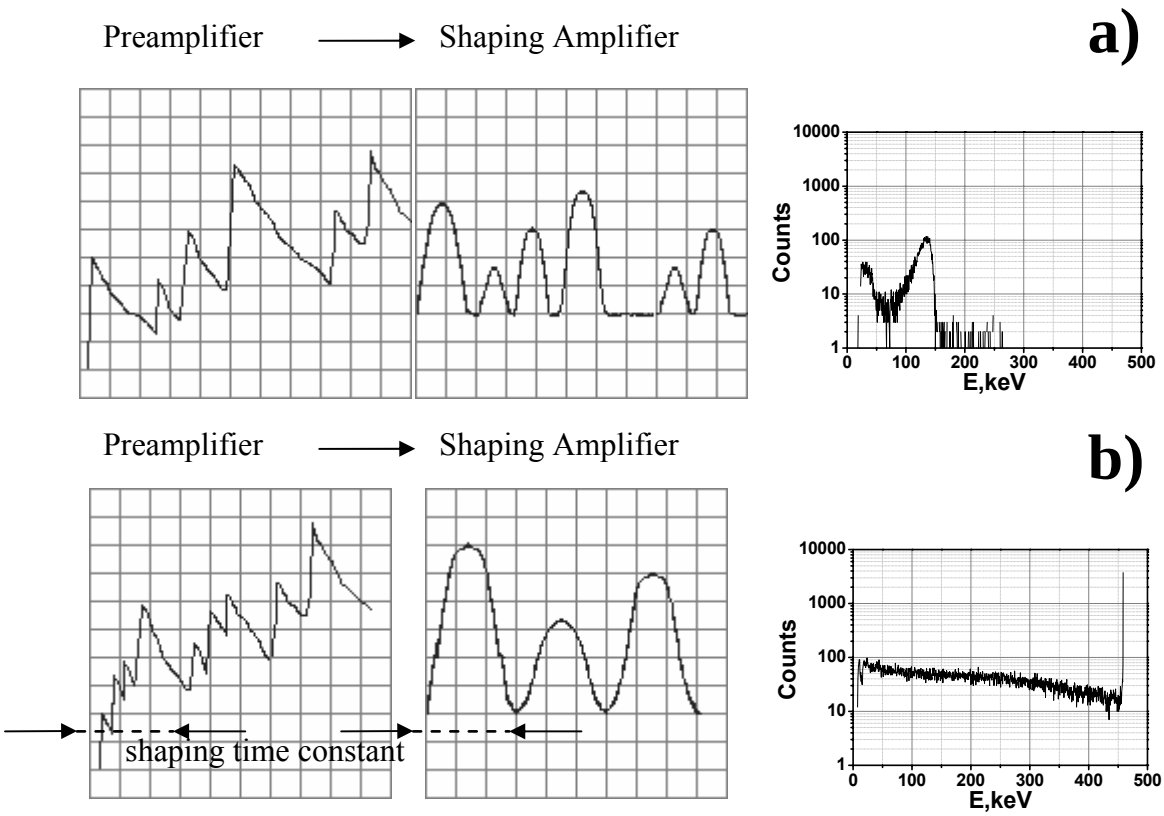

Fig.26 Example of signals for the case of a) low flux from plasma and satisfactory time constant of shaping amplifier b) pile-up effect during high flux from plasma and large time constant of shaping amplifier.

In order to reduce the flux on the detector and improve the diagnostic abilities several ways are proposed:

- To modify shaping amplifier – reducing of the shaping amplifier time constant.
- To install an adjustable piezo-electrically-driven slit (Fig.27) between the aperture and the detector. Gap between slit plates may be reduced up to 5÷10μm.
- To install a thicker (0.2 μm) aluminum foil. This will allow cutting off the low energetic part of spectrum which constitutes the majority of the emitted particles.

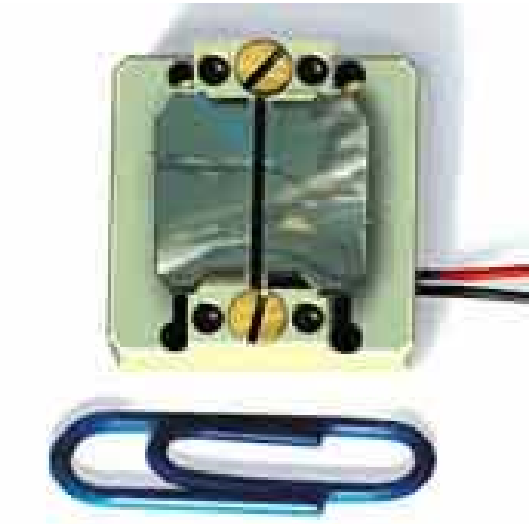

Fig.27 Adjustable piezo-electrically-driven slit.

2.3 GEOMETRY OF MEASUREMENTS

Due to limited space on the stage near LHD the detailed design for diagnostic chamber and cooling system was prepared in 3D CAD system (Fig.28). The photograph of assembled diagnostic with cooling and vacuum system is shown on Fig.29. The ARMS-NPA-based diagnostic is located at the 9 O port of LHD vacuum vessel as it is shown on the top view on Fig.30. Black and blue lines correspond to two available positions of ARMS-NPA diagnostic. Position marked by blue color sightlines is preferable for horizontal angular-resolved scanning of plasma from perpendicular to tangential directions but vertical scan is not available due to interference of sightlines with LHD chamber. Position marked by black color sightlines is preferable for radial scan of plasma by all 20 sightlines, it can be used for horizontal angular resolved scan too but in a quite a narrow range of pitch angles (mostly perpendicular direction). Experimental data presented in current work correspond to blue colored sightlines.

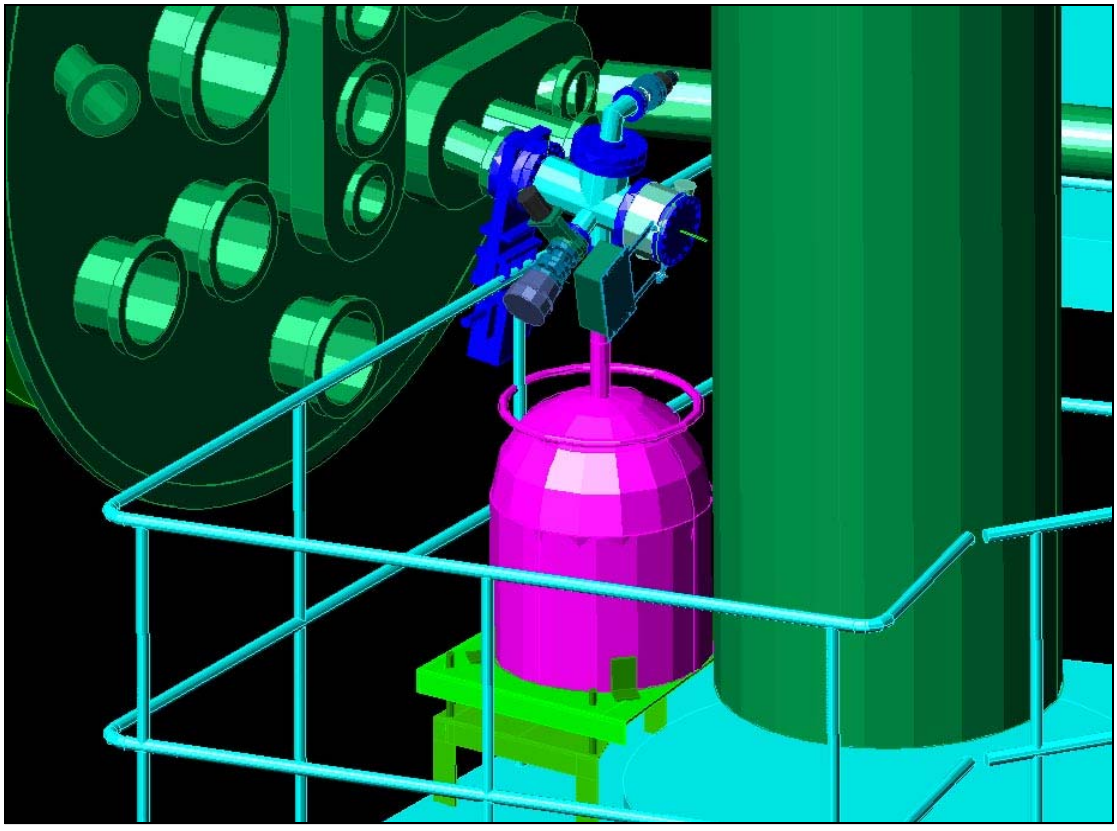

Fig.28 3D view of ARMS-NPA diagnostic with cooling system.

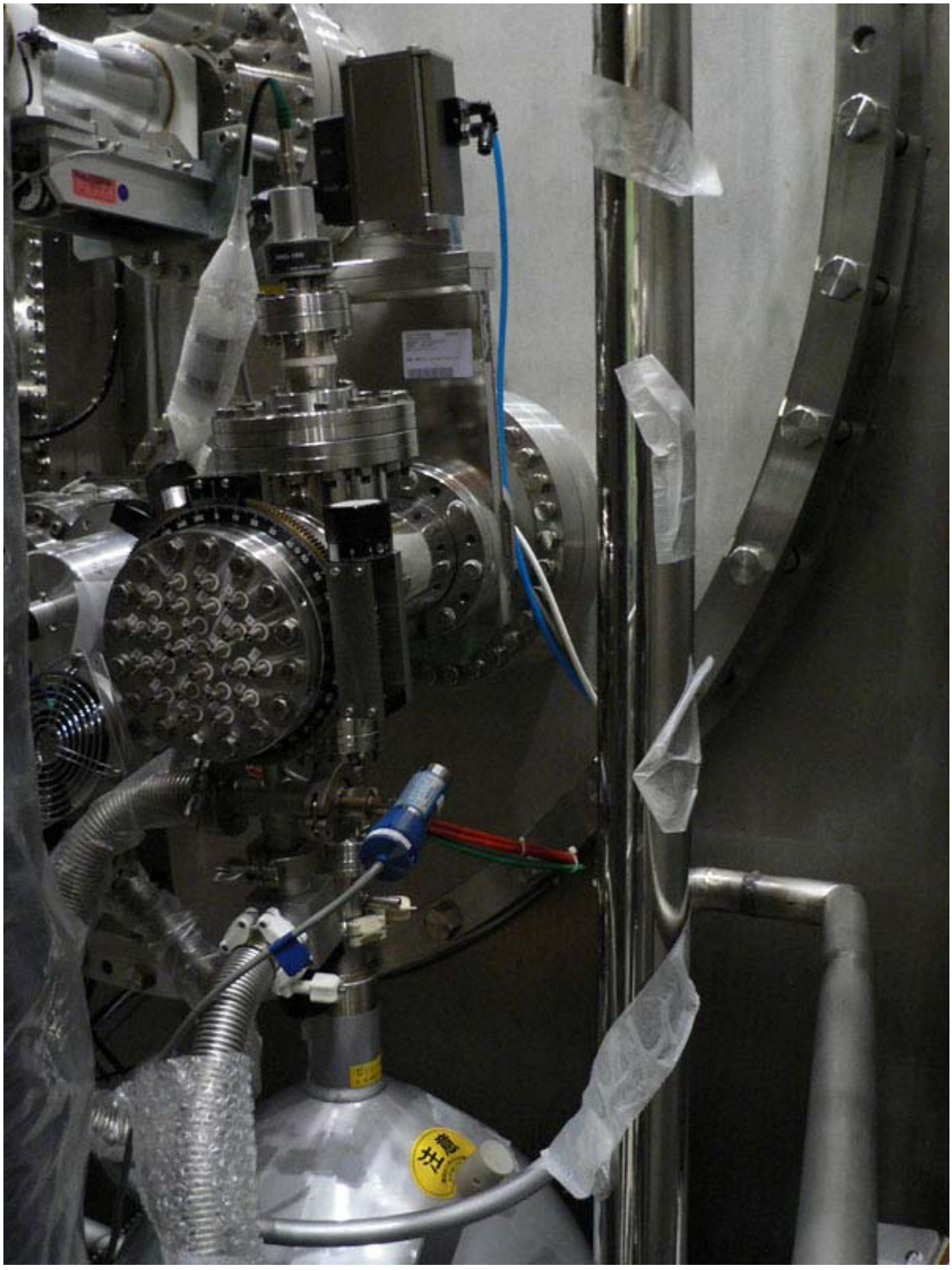

Fig.29 Photograph of assembled for experimental measurements diagnostic with cooling and vacuum systems.

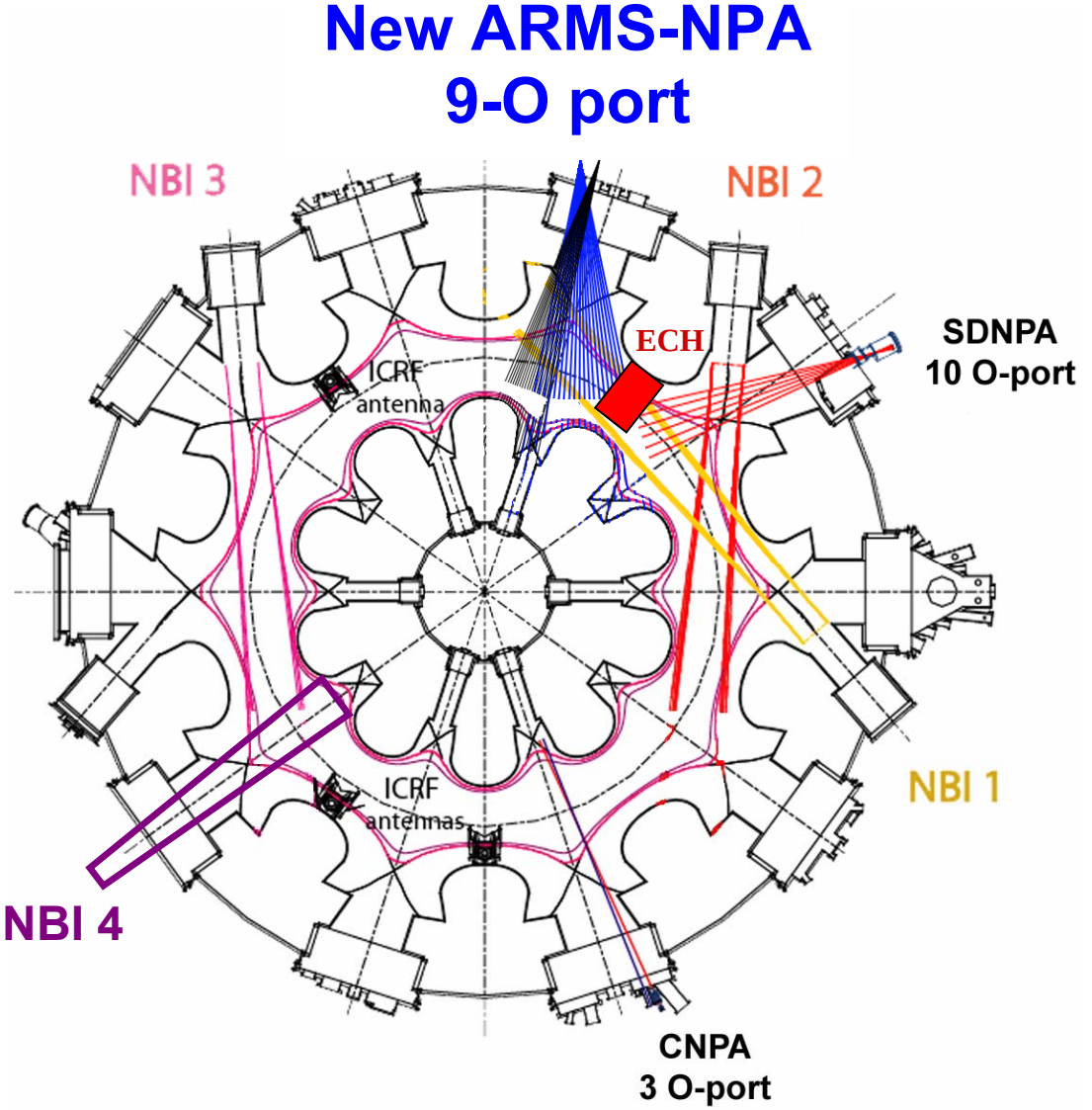

Fig.30 ARMS-NPA Diagnostic sightlines and location at LHD together with CNPA and SDNPA versus NBI, ECH and ICRF.

Magnetic surfaces cross-sections for all 20 sightlines and local pitch angles along sightlines for two diagnostic positions were calculated from VMEC numerical solution of 3D MHD equilibrium equations assuming nested flux surfaces [27]. The structure of magnetic surfaces is shown on Fig.31. Blue colored part of sightline is from detector segment to the central region of plasma and red colored part of sightline is from central part of plasma to the core of LHD. As it can be easily seen the path along every sightline differs from each other that may affect on the measured flux from plasma. Local pitch angles for horizontal and vertical scanning planes are presented at Fig.32. Range of angles between magnetic axis and sightlines to be measured by new diagnostic is 80º ÷ 150º.

As the detector is a linear array, the intersection of circular magnetic axis with a flat plane of sightlines has only 2 points. Thus only 2 detector sightlines can observe the very center of plasma. The sheaf of sightlines was adjusted in such a way that all the channels to observe as closer as possible the central region of plasma.

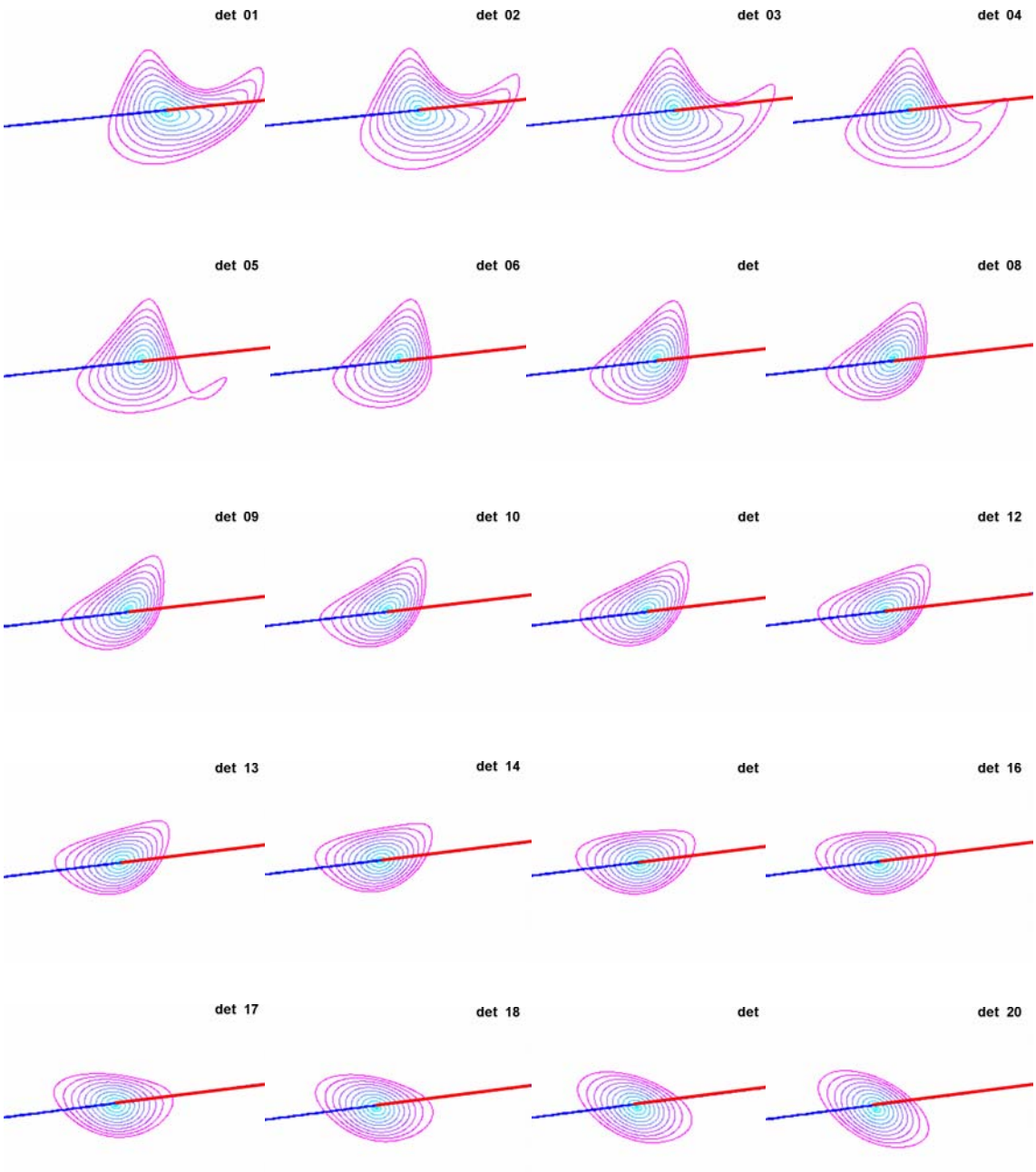

Fig.31 Magnetic surfaces cross-sections for every detector sightline (blue part of the straight line is “detector-plasma center” line, red part is “plasma center-LHD core” line.

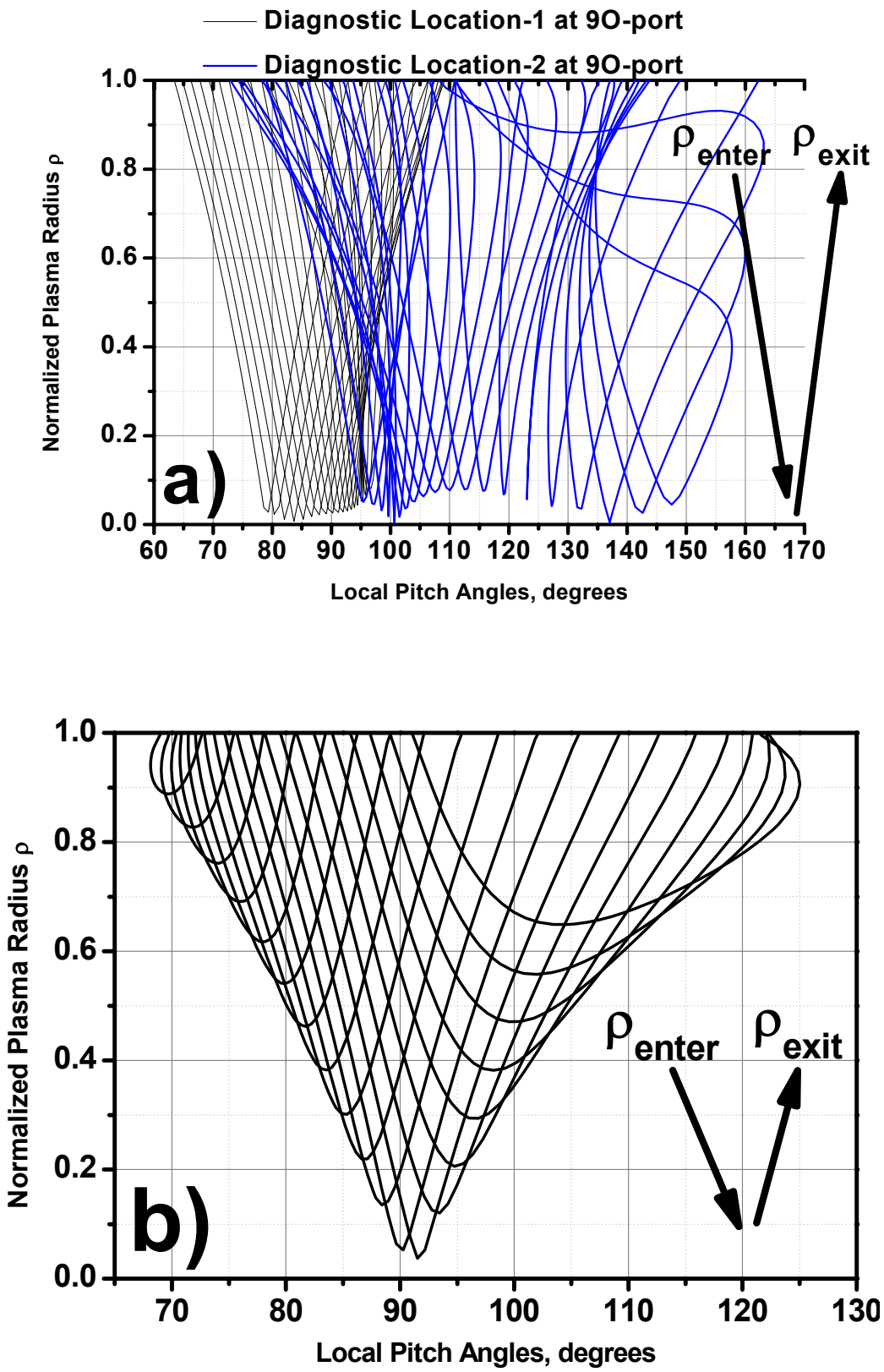

Fig. 32 The sheaf of pitch-angles along the sightlines: (a) horizontal diagnostic plane, blue and black lines correspond to blue and black sightlines of the Fig.30; (b) vertical diagnostic plane.

2.4 CALIBRATION

Preliminary calibration of every detector segment has been made with a radioactive source (Am-241) at room temperature. A typical calibration curve is shown on Fig.33, from which the correspondence between channel numbers and energy values can be estimated by Am-241 characteristic Roentgen peaks.

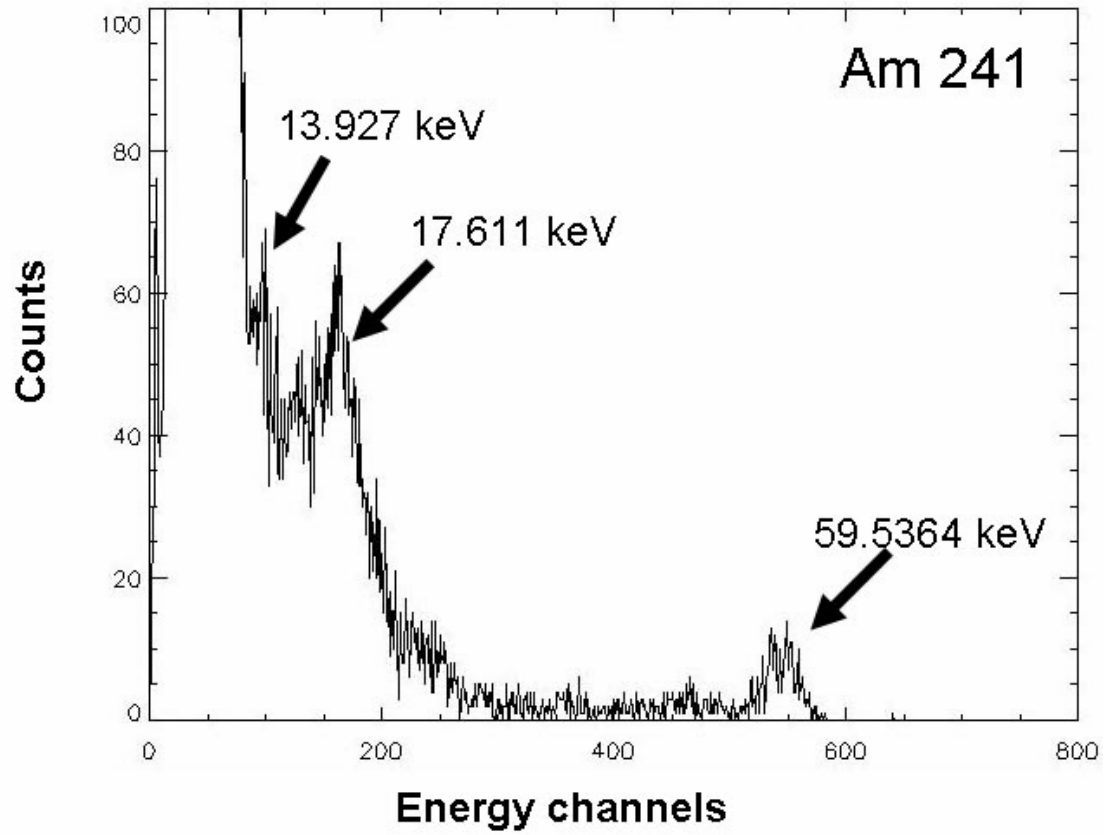

Fig.33 Typical calibration curve of every channel.

The attenuation of X-rays in a thin aluminum foil is negligible but it appears to be significant in fast particles case. These losses are negligibly differ from each other for every detector segment due to the different path lengths of particles passing through the aluminum foil at different angles on the way to the corresponding detector segments. One of the AXUV detector advantages is the absence of a doped dead-region. Thus, only the losses in the aluminum foil should be taken into account.

These energy losses for H and He particles were obtained from SRIM calculations [30, 31] and taken into account during calibration (Fig.34).

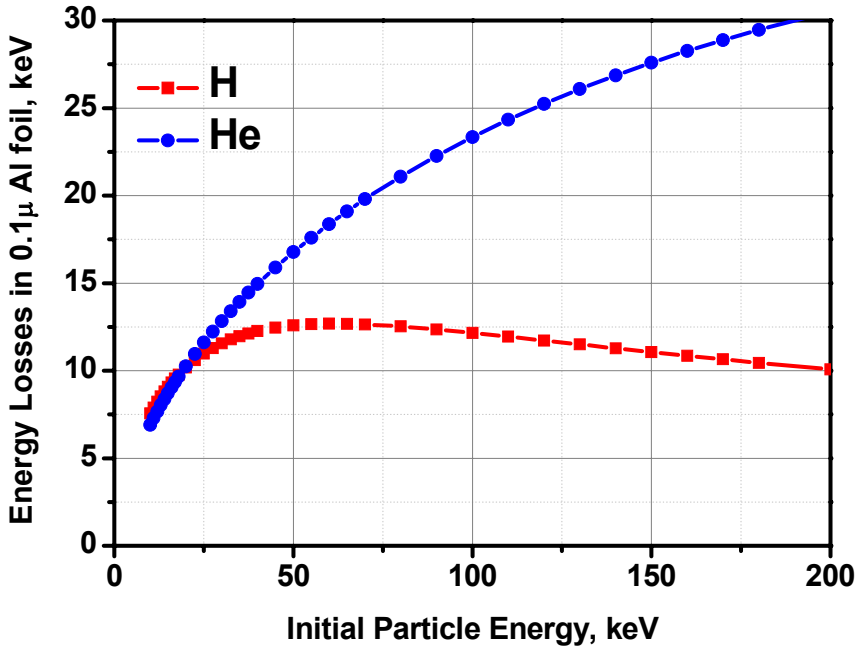

Fig.34 Fast particles energy losses in 0.1μ Al foil.

Coordinates of the detector segment centers and the aperture center were calculated from 3D CAD data. Diagnostic sightline and reference points *in situ* checking on LHD is to be performed.

3. Experimental Results and Data Interpretation

3.1 ANGULAR ANISOTROPY IN NBI REGIMES

3.1.1 Angular dependence NBI direction

First measurements by ARMS-NPA diagnostic with real plasma have been made on LHD for a variety of plasma heating conditions.

The typical energy-resolved spectrum measured along a single sightline is presented at Fig.35.

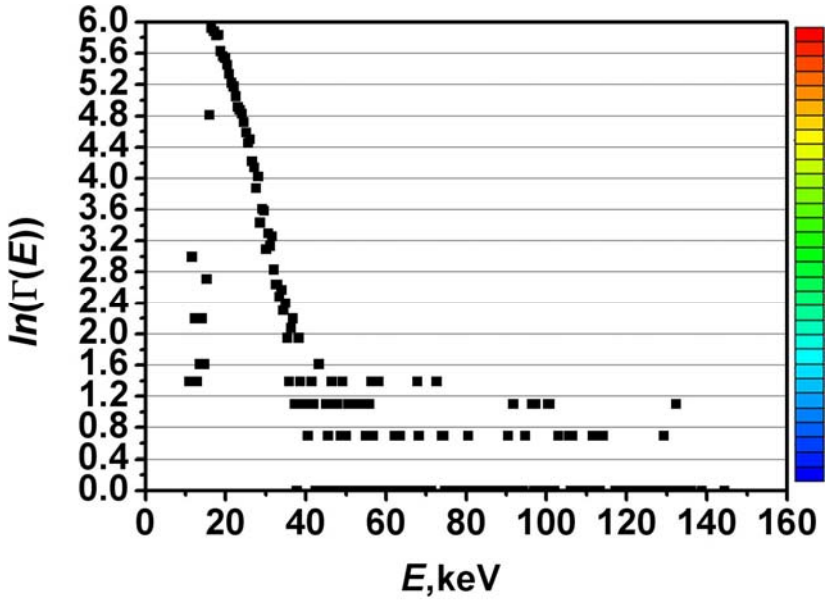

Fig.35 Energy spectrum measured along one of the 20 sightlines.

The set of such spectra along all sightlines forms the angular distribution of fast particles as it is shown in the Fig.36. For visual illustration of the flux dependence on the direction of the sightline the slope θ of every spectra was assumed as the angle between the sightline and magnetic axis. The 1st channel directed in the most tangential direction was broken in the very beginning of experimental campaign. Thus hereafter only data for 19 sightlines will be presented. Detector (preamplifier) repairing and precise positioning *in situ* are to be made (at the moment coordinates of the detector segments and the aperture center are calculated from three-dimensional (3D) computer-aided design (CAD) data).

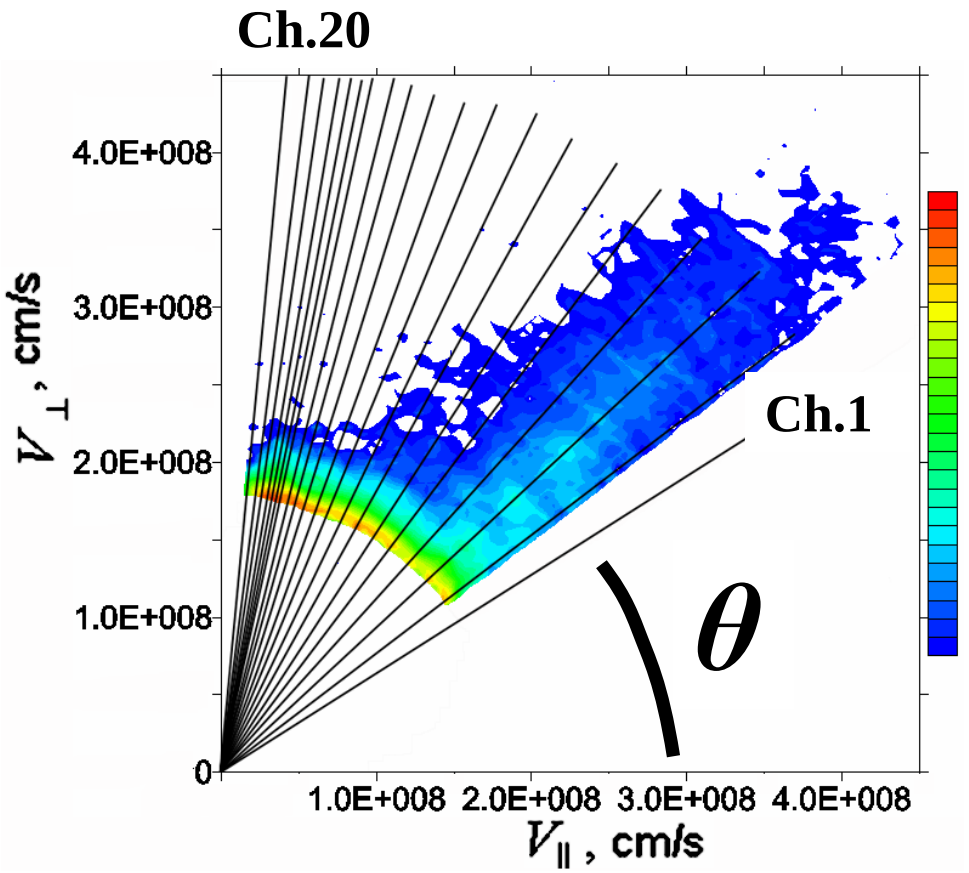

Fig.36 Energy spectrum measured along 19 sightlines. (θ is the angle between the sightline and magnetic axis).

Angular-resolved measurements were made for co- and counter-directed NBI. Time diagram of the discharge with positive-directed magnetic field (B=2.0T, Rax=3.6 m) is shown on Fig.37. Fast particle spectra were plotted for time interval 3.0÷3.2 of co-injecting NBI2 operation and 1.1÷1.3 of counter-injecting NBI1 operation.

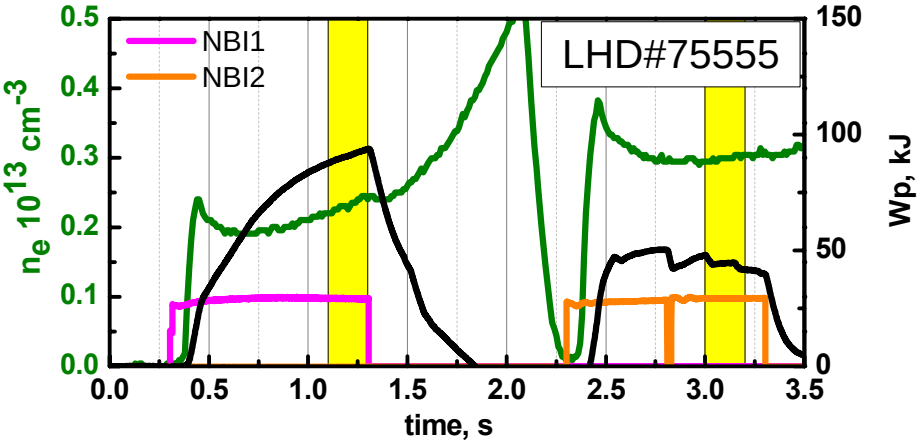

Fig.37 Time diagram of the LHD plasma discharge.

Fig.38 and Fig.39 illustrate angular behavior of fast particles for co- (NBI2) and counter- (NBI1) neutral beam injection respectively.

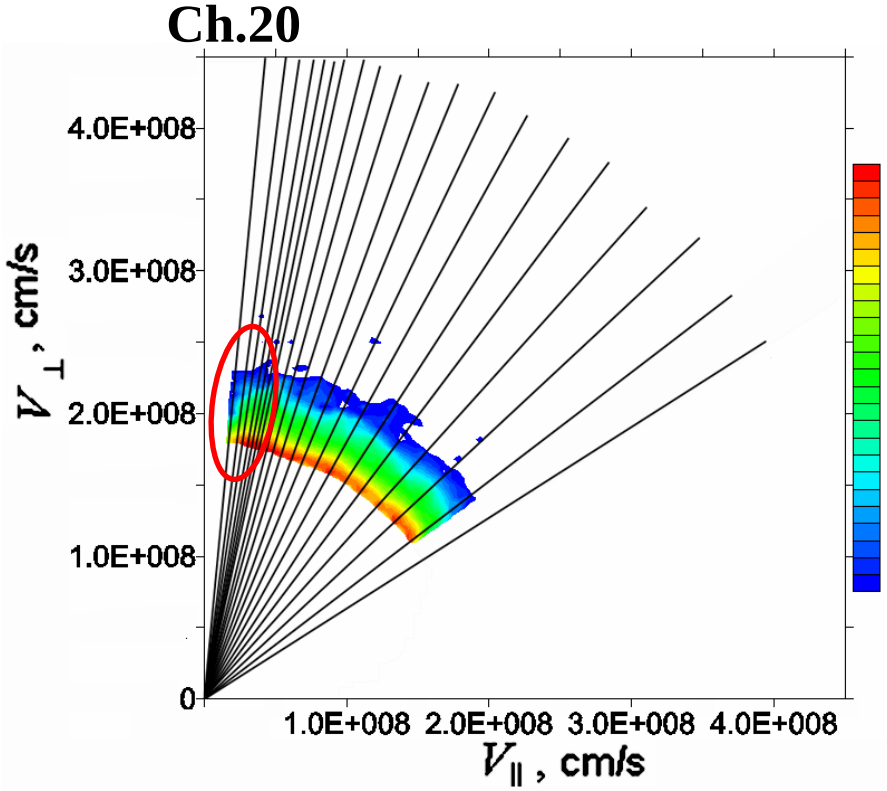

Fig.38 Angular dependence of neutral flux during co-injection (NBI2 case).

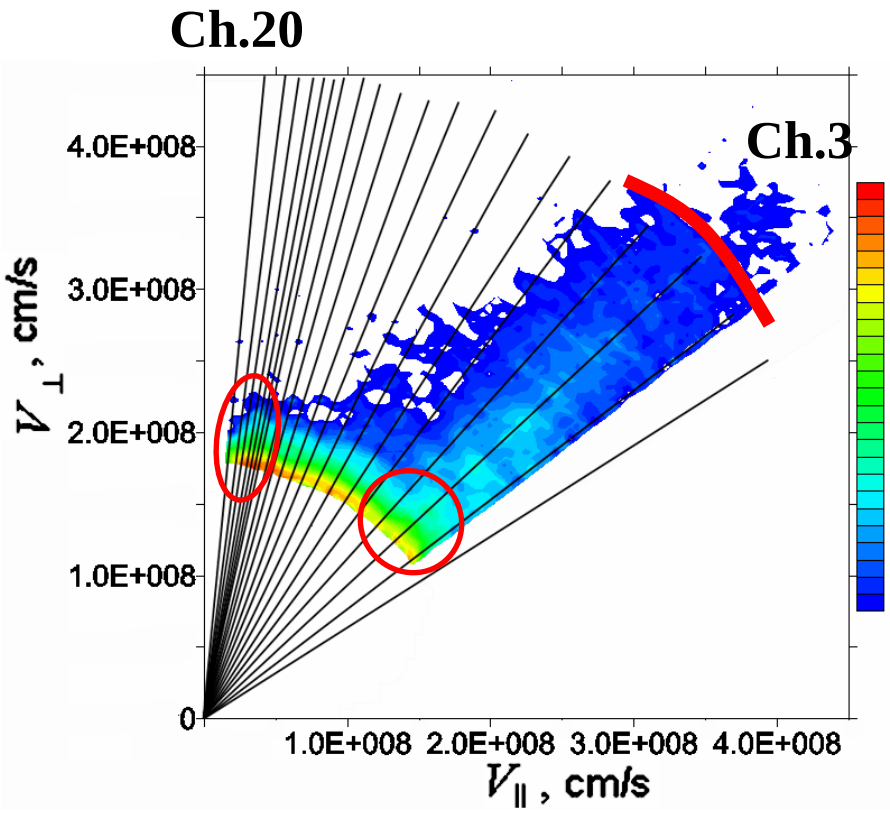

Fig.39 Angular dependence of neutral flux during counter-injection (NBI1 case).

Beam energy and injected power of NBI1is 180keV and 5.2MW correspondingly, and of NBI2 is 157keV and 3.2MW. It is necessary to remind that diagnostic is directed in the same direction as co-injector NBI2 and in opposite direction to counter-injector NBI1 (or NBI3). Thus fast particles from NBI2 must be backscattered to enter the detector. Spectra for counter injecting NBI1 clearly demonstrate angular- and energy- resolved distribution of suprathermal fast particle tail. As it can be seen from the Fig.38 angular distribution during NBI2 work is rather uniform along all sightlines except the sightlines close to perpendicular direction. Spectra for three close to perpendicular direction sightlines are plotted in Fig.40. Spectrum measured along the 20th sightline is significantly different from 19th and 18th (all other sightlines are similar to 18th). Pitch angle between the 20th sightline and magnetic axis is 85 degrees. Such effect may be due to presence of loss cone near this direction.

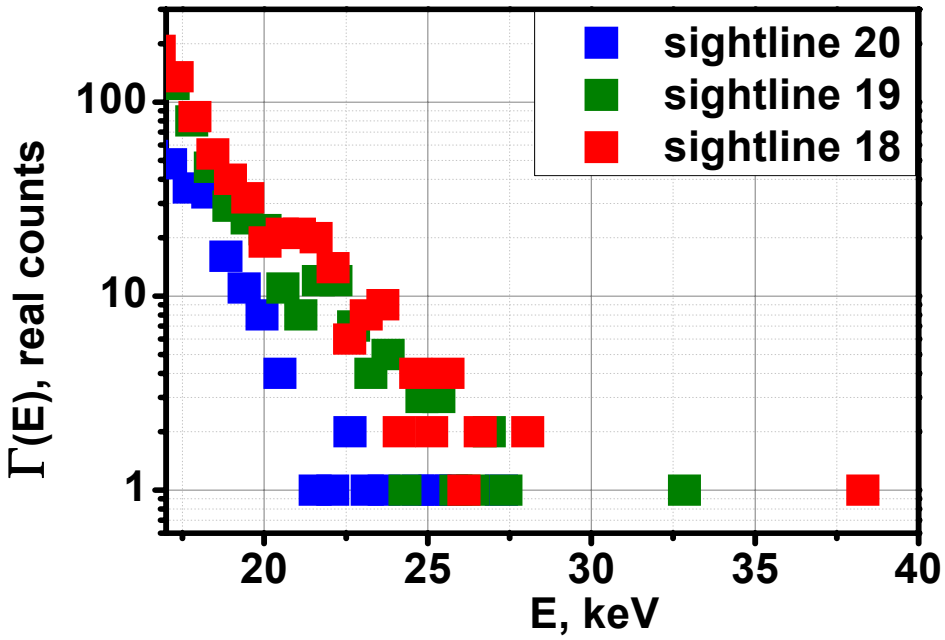

Fig.40 Fast particle spectra for three of the sightlines close to perpendicular direction (sightline 20 is the most perpendicular one) during co-injecting NBI2 operation (positive magnetic field).

Same effect was observed in the case of counter-injecting NBI1 operation. Fig.41. In addition to that the drop at low energetic part of the spectra was observed at sightlines close to parallel direction together with increase of high energy part of the spectra Fig.42.

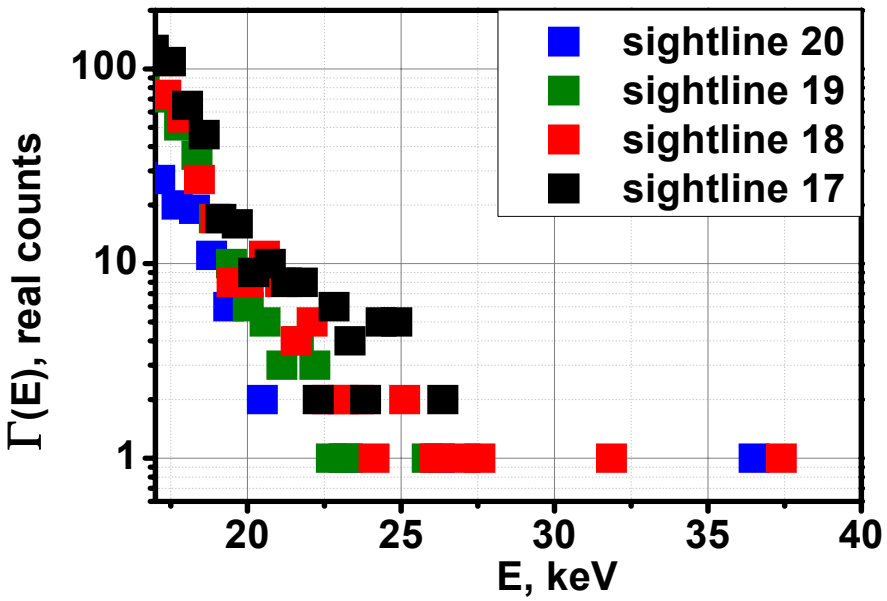

Fig.41 Fast particle spectra for four of the sightlines close to perpendicular direction (sightline 20 is the most perpendicular one) during counter-injecting NBI1 operation (positive magnetic field).

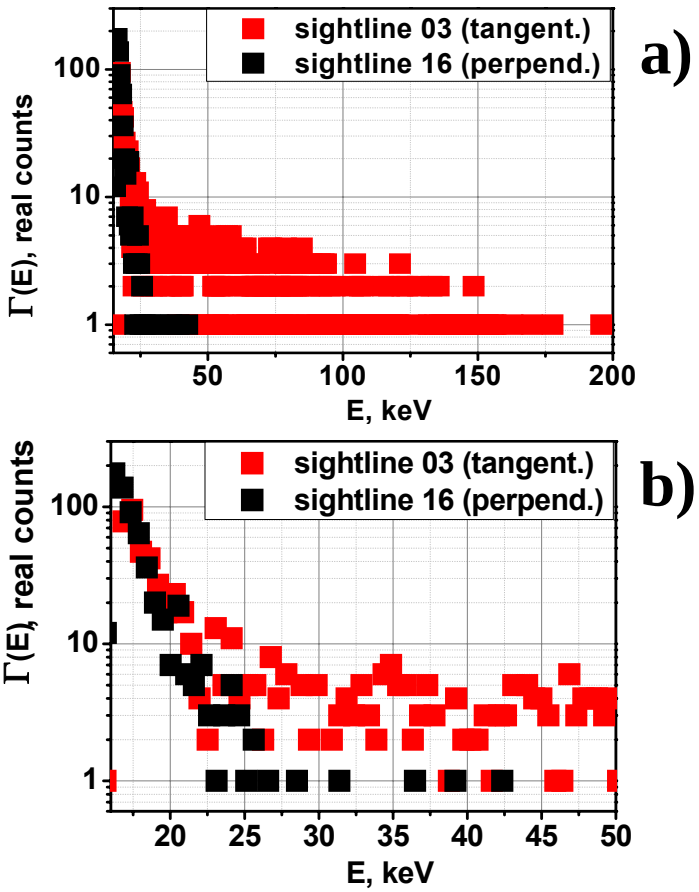

Fig.42 Comparison of fast particle spectra for one of perpendicular sightlines and one of tangential sightlines during counter-injecting NBI1 operation (positive magnetic field) for the same time interval. The difference between (a) and (b) pictures is only in energy scale.

In order to check how the magnetic field direction will influence on the angular distribution, measurements were made for NBI1 and NBI2 in B=-2.811T and R=3.65m magnetic axis configuration. In this case NBI1 is co-injecting and NBI2 is counter-injecting. Time diagrams of the discharges with NBI2 and NBI1 are shown on Fig.43 and Fig.44 correspondingly. Angular- and energy resolved spectra for these two cases are shown on Fig.45 and Fig.46 correspondingly. Fast particle spectra were restored for time intervals marked by the yellow color.

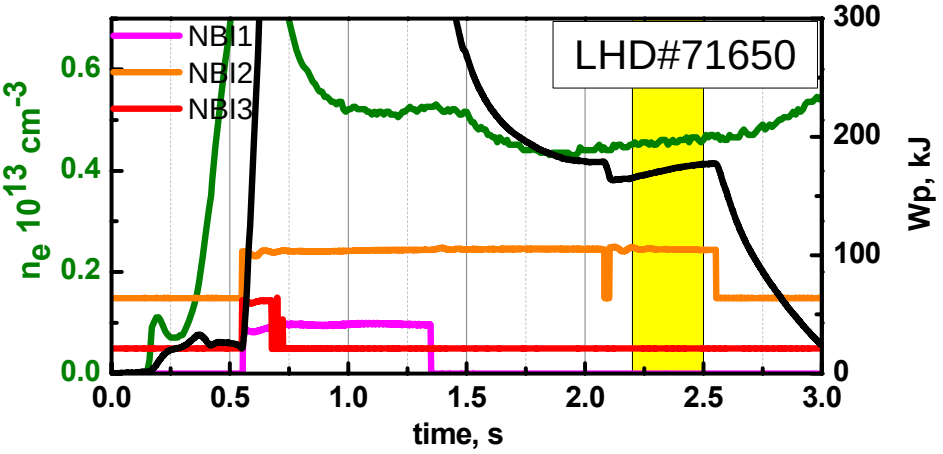

Fig.43 Time diagram of the LHD plasma discharge for the case of counter-injecting NBI2.

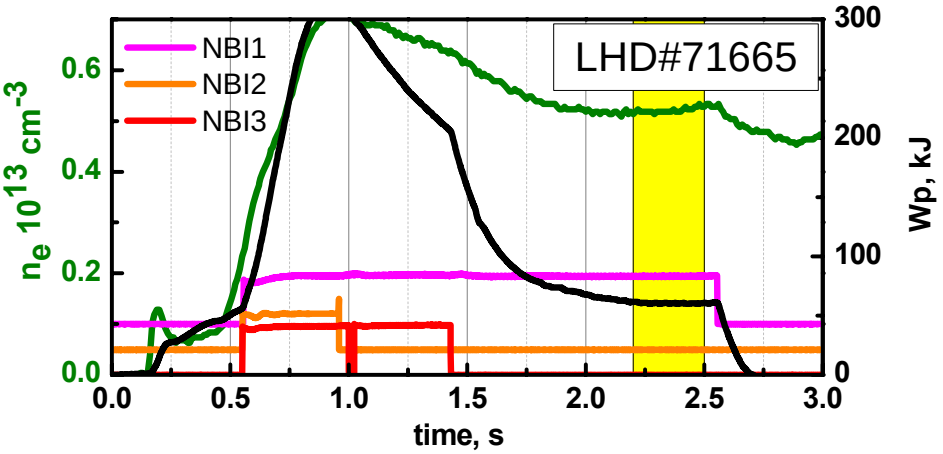

Fig.44 Time diagram of the LHD plasma discharge for the case of co-injecting NBI1.

Beam energy and injected power of NBI2 is 162keV and 3.6MW correspondingly, and of NBI1 is 178keV and 4.6MW. For the case of negative magnetic field direction the angular resolved spectra of fast particles don't demonstrate suprathermal ion tail same as in the case of positive magnetic field. Effect of significant reducing of the fast particle flux still remains at the sightlines close to perpendicular direction at 80º÷85º pitch-angle range Fig.47.

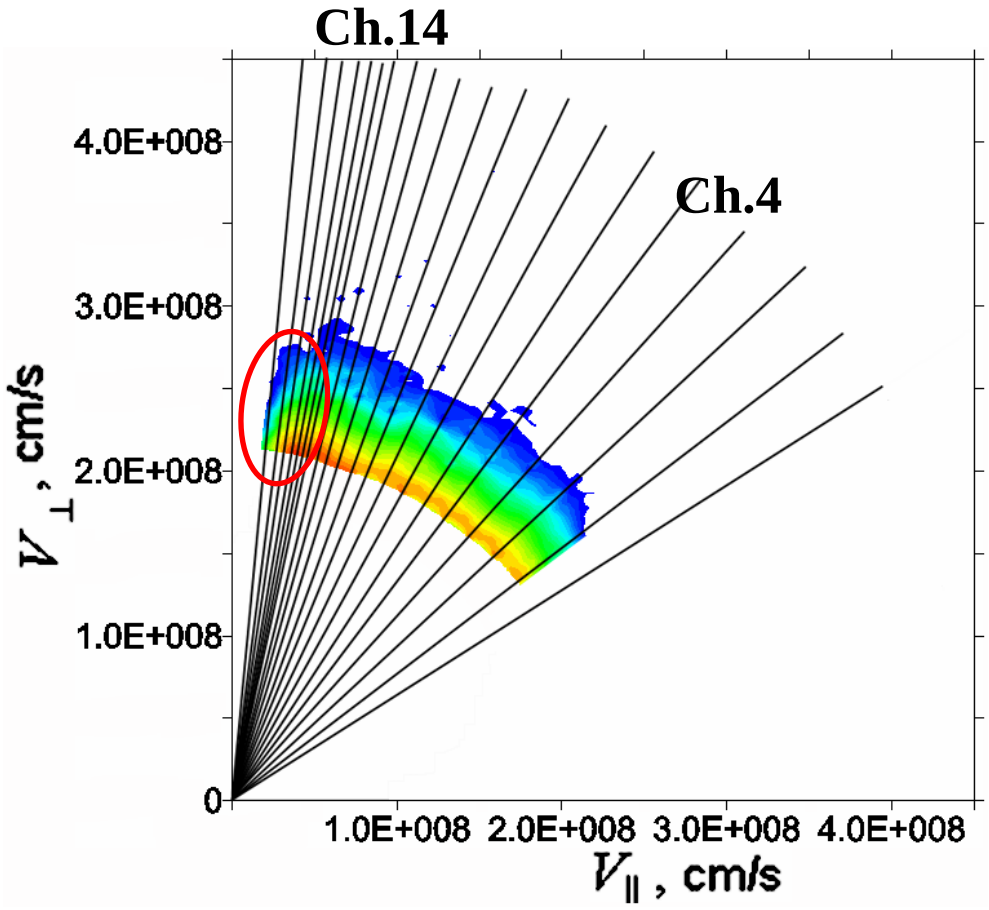

Fig.45 Angular dependence of neutral flux during counter-injection (NBI2 case).

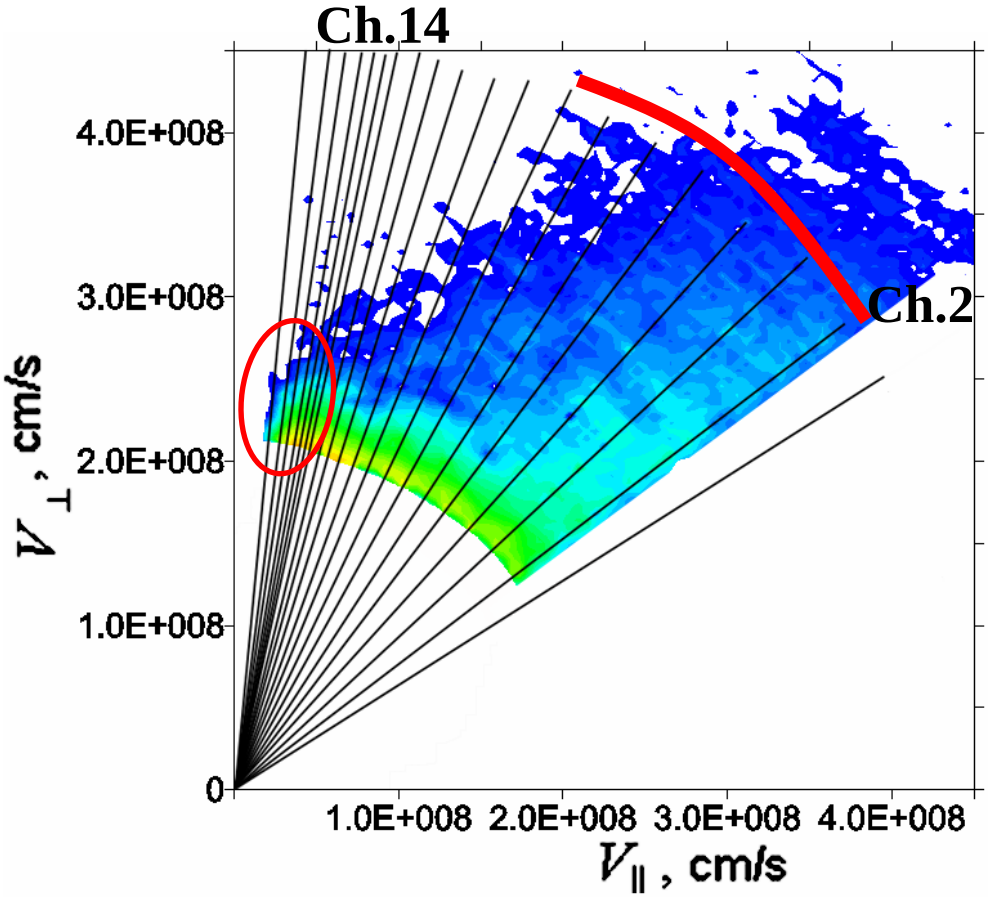

Fig.46 Angular dependence of neutral flux during co-injection (NBI1 case).

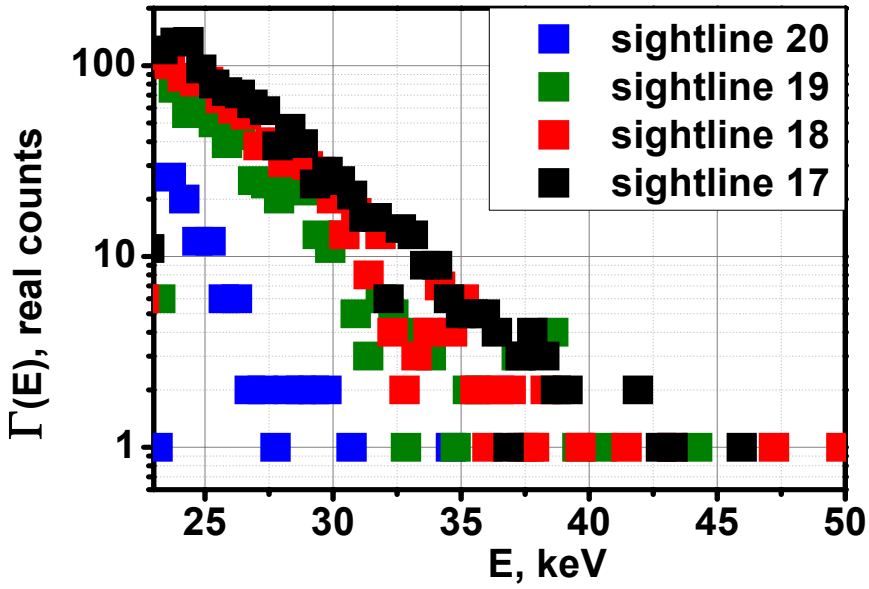

Fig.47 Fast particle spectra for four of the sightlines close to perpendicular direction (sightline 20 is the most perpendicular one) during counter-injecting NBI2 operation (negative magnetic field).

In addition to that the spectra along all other sightlines are not that uniform as for the case of positive magnetic field. The increase of fast particle population observed in the region of 14th sightline is reduced with more parallel direction (Fig.48).

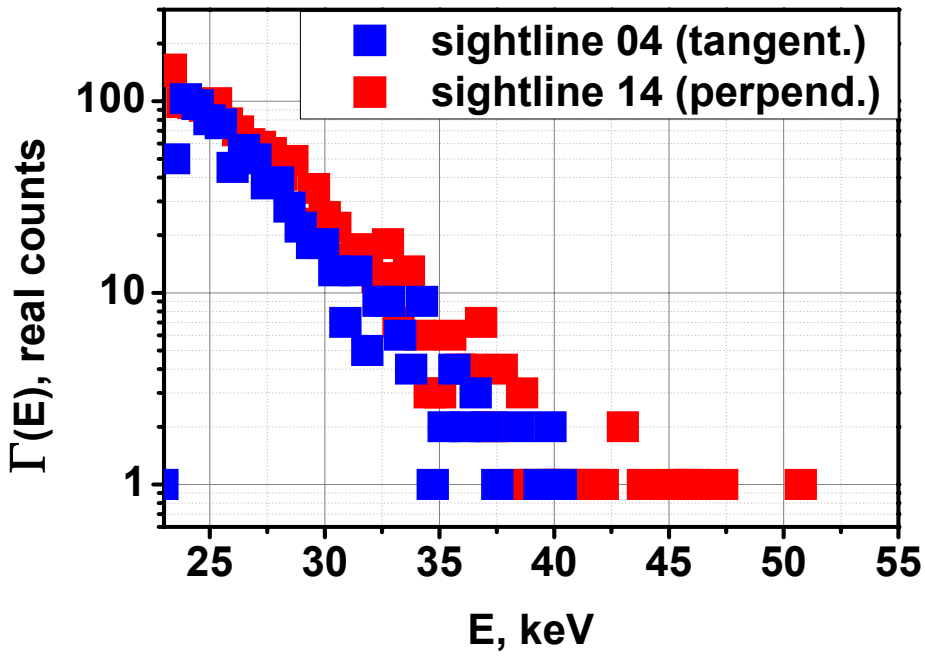

Fig.48 Comparison of fast particle spectra for one of perpendicular sightlines and one of tangential sightlines during counter-injecting NBI2 operation (negative magnetic field).

During operation of co-injecting NBI1 in negative magnetic field, effect of significant reducing of the fast particle flux still remains at the sightlines close to perpendicular direction (Fig.49).

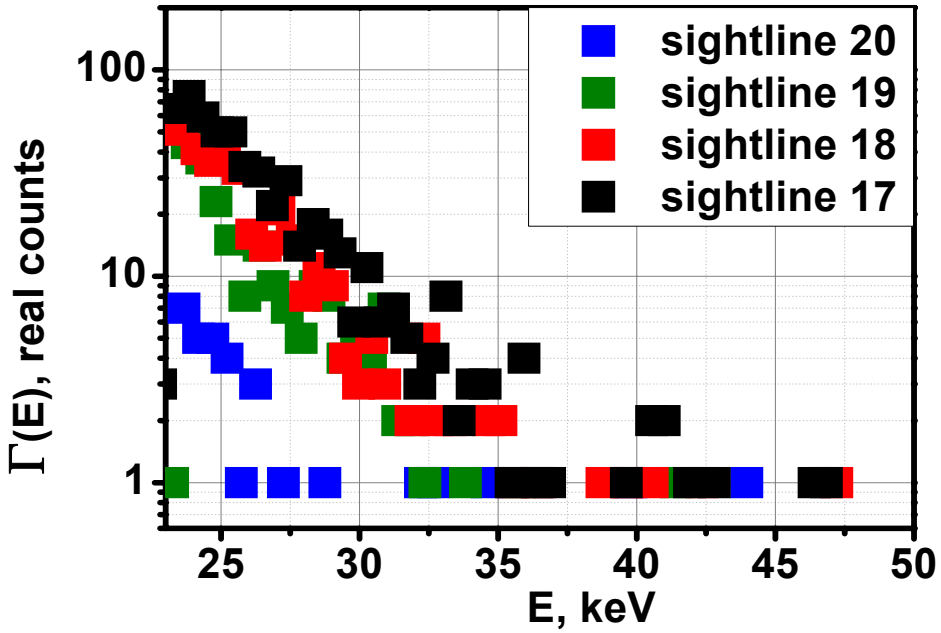

Fig.49 Fast particle spectra for four of the sightlines close to perpendicular direction (sightline 20 is the most perpendicular one) during co-injecting NBI1 operation (negative magnetic field).

During co-injecting NBI1 operation in the case of negative magnetic field spectra along all other sightlines are not uniform (same tendency as in positive magnetic field). Spectra demonstrate angular- and energy- resolved distribution of suprathermal fast particle tail. For the case of negative magnetic field angular range of suprathermal fast particle tail is wider than in the case of positive magnetic field (Fig.39 and Fig.46 marked by red line) This may be due to either stronger magnetic field value (in negative case) or due to larger region of confined particles during co-injecting NBI.

For negative magnetic field the drop at low energetic part of the spectra was observed at sightlines close to parallel direction together with increase of high energy part of the spectra (same as in positive magnetic field case) (Fig.50).

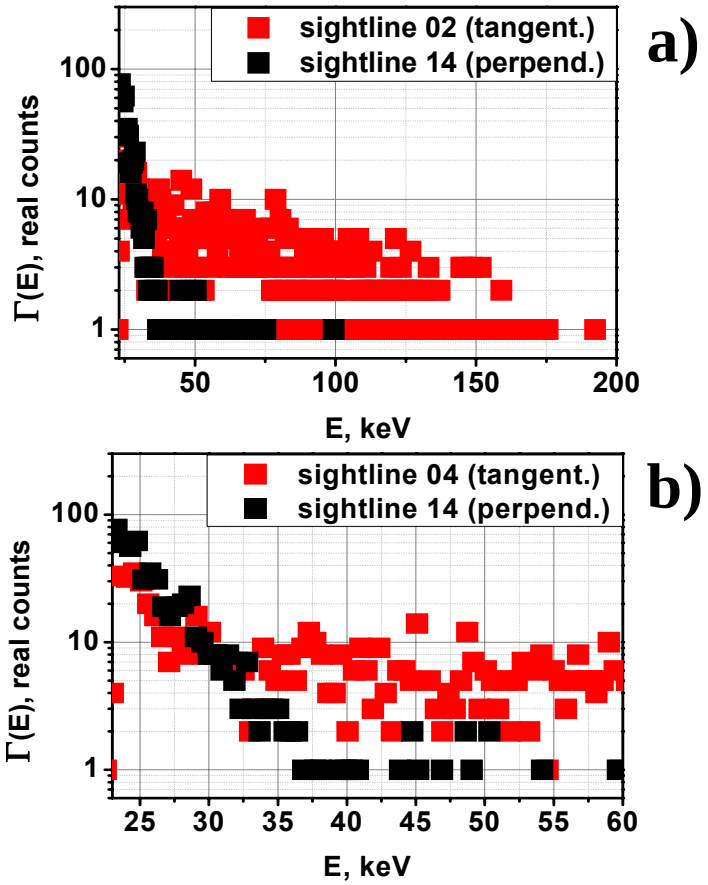

Fig.50 Comparison of fast particle spectra for one of perpendicular sightlines and one of tangential sightlines during counter-injecting NBI1 operation (positive magnetic field) in the same time interval. The difference between (a) and (b) pictures is only in energy scale.

3.1.2 Brief Summary

- In all cases positive or negative magnetic field direction, co- or counter NBI injection the significant reducing of the fast particle flux was observed at the sightlines close to perpendicular direction at 80º÷85º pitch-angle range. This may be due to the presence of loss-cone in this region.
- Angular distribution of fast particles depends on the type of heating, magnetic field direction and magnetic field strength.
- Co-injection is more favorable for heating from the point of view of wider angular range of suprathermal fast particle tail.

3.2 MAGNETIC FIELD STRENGTH EFFECT

3.2.1.1 The case of negative magnetic field and co-injecting NBI1

As it was supposed in the previous chapter magnetic field strength may affect on the fast ion confinement and their angular distribution. It was shown on the example of negative magnetic field and co-injecting NBI1. Thus experiments in negative magnetic field together with co-injecting NBI1 and with varying magnetic field strength were held to check the influence of magnetic field strength on the angular distribution and possible loss-cones in the region close to perpendicular. Magnetic axis position in all the cases was Rax = 3.6m. Three values of the magnetic field strength were chosen for demonstration B_1^- = -0.75T, two times increased magnetic field with B_2^- = -1.49T and one more time almost two times increased magnetic field B_3^- = -2.75T. Time diagrams of the discharges are shown at Fig.51.

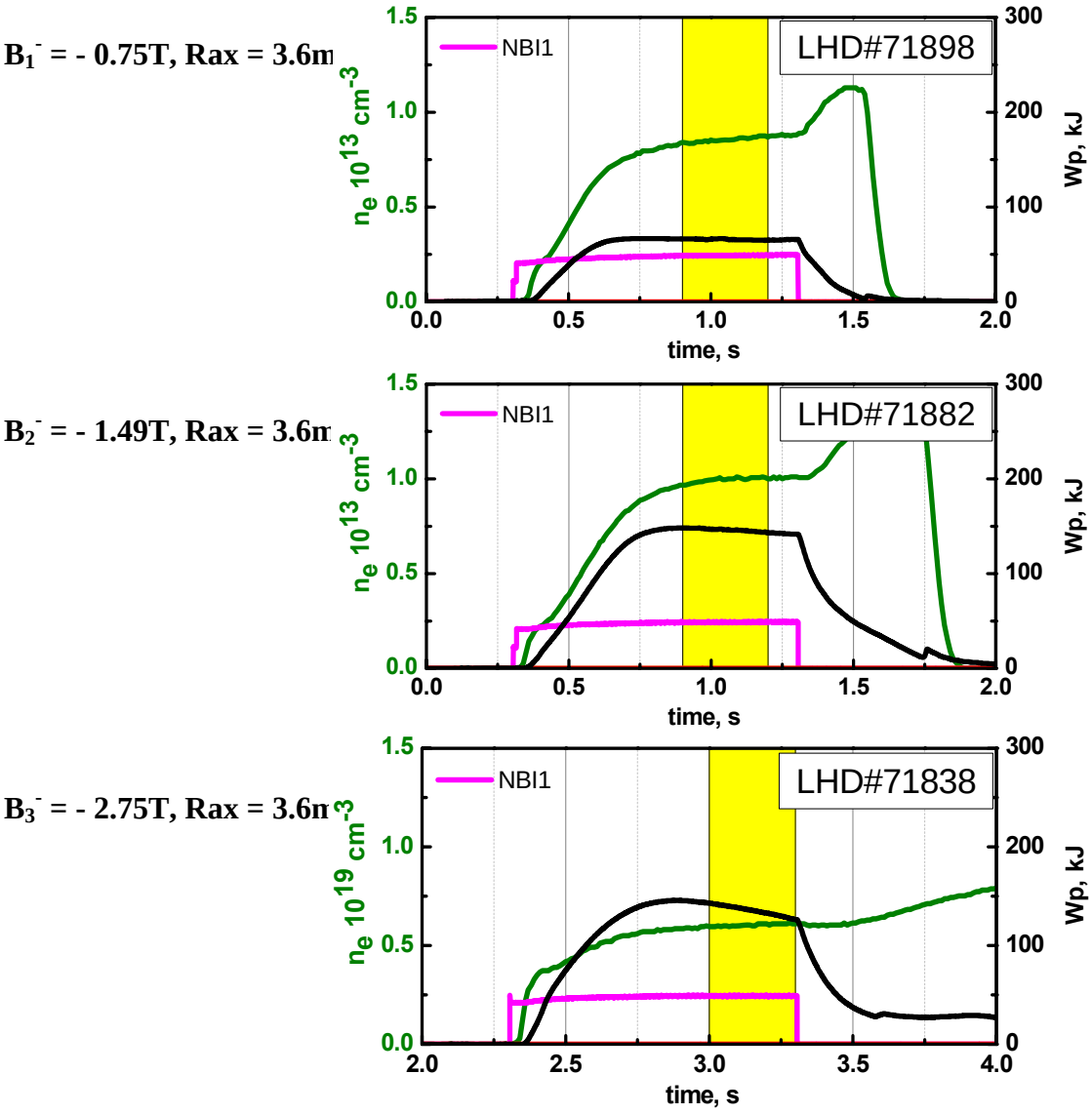

Fig.51 Time diagrams of LHD plasma discharge for three different magnetic field strength values B_1^- = -0.75T, B_2^- = -1.49T and B_3^- = -2.75T.

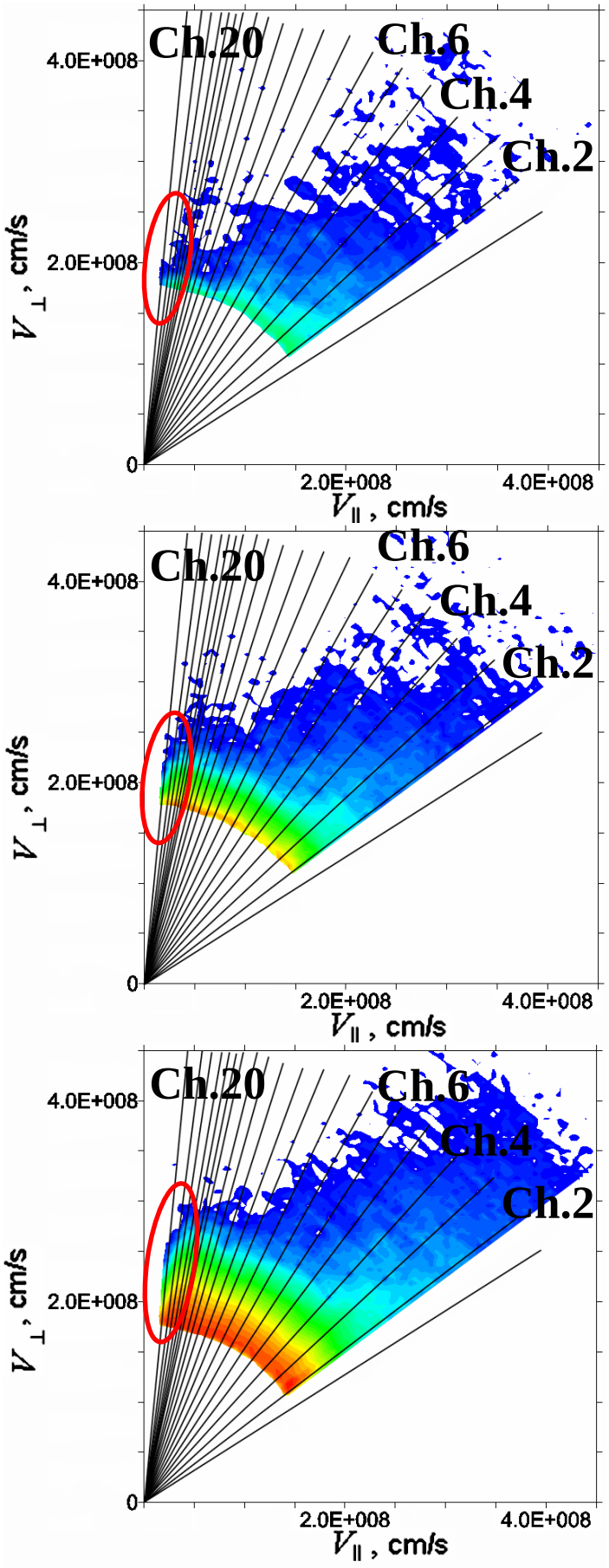

$B_1^- = -0.75T$, Rax = 3.6m

$B_2^- = -1.49T$, Rax = 3.6m

$B_3^- = -2.75T$, Rax = 3.6m

Fig.52. Restored fast particle spectra for marked time intervals in three cases of negative magnetic field.

Beam energy and injected power of NBI1 for the case $B_1^- = -0.75T$ was 175keV and 3.9MW correspondingly, and for the case $B_2^- = -1.49T$ and $B_1^- = -2.75T$ beam energy and injected power 178keV and 4.4MW. Angular- and energy resolved fast particle spectra were plotted for three cases of magnetic field strength ($B_1^- = -0.75T$, $B_2^- = -1.49T$ and $B_3^- = -2.75T$) on Fig.52 in time intervals marked by yellow color at time diagrams of Fig.51. As it can be seen from these pictures increasing of magnetic field strength leads to broadening of the angular range of suprathermal fast ion tail and to increasing of supratermal fast particle population (mostly in parallel sightlines). More clearly it can be seen from the quantitative comparison of the spectra for Sightlines No 2, 4 and 6 presented on Fig.53.

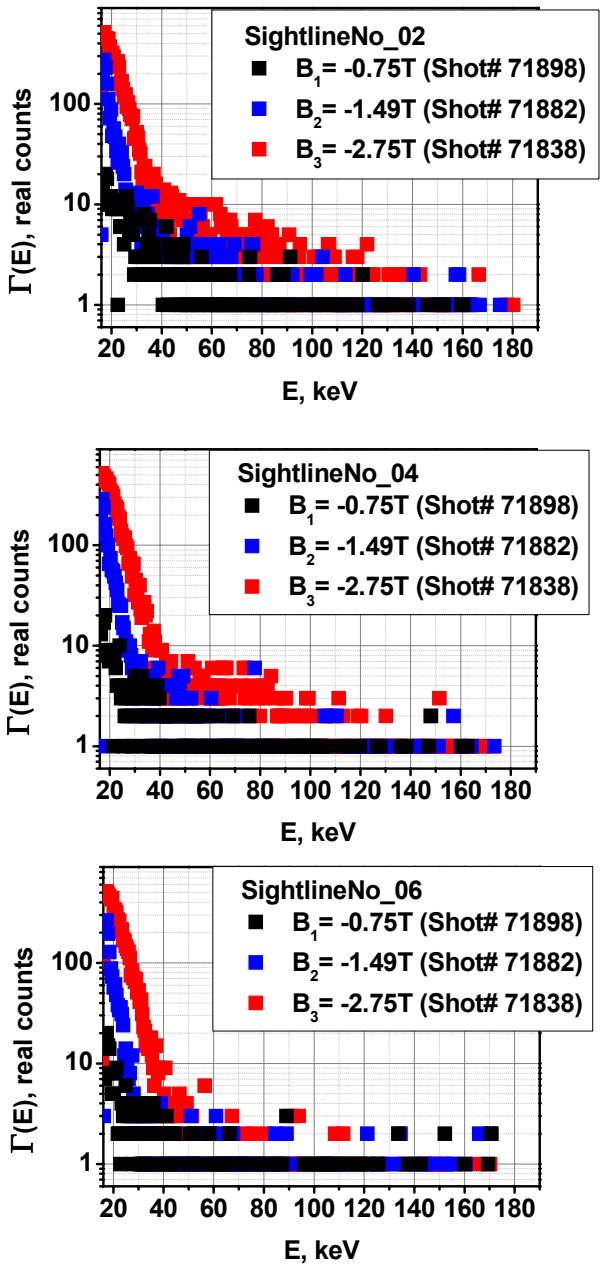

Fig.53 Fast particle spectra measured along SightlineNo 2, 4 and 6 for three different magnetic field strength values $B_1^- = -0.75T$, $B_2^- = -1.49T$ and $B_3^- = -2.75T$.

Fast particle spectra of Fig.53 were corrected by the Spitzer's slowing down time:

$$\tau_s = \frac{3m_p T_e^{3/2}}{4\sqrt{2\pi} n_e e^4 \Lambda m_e^{1/2}},$$

which is equal to 0.15, 0.37 and 0.9 ms for B_1^-= -0.75T, B_2^-= -1.49T and B_3^-= -2.75T correspondingly.

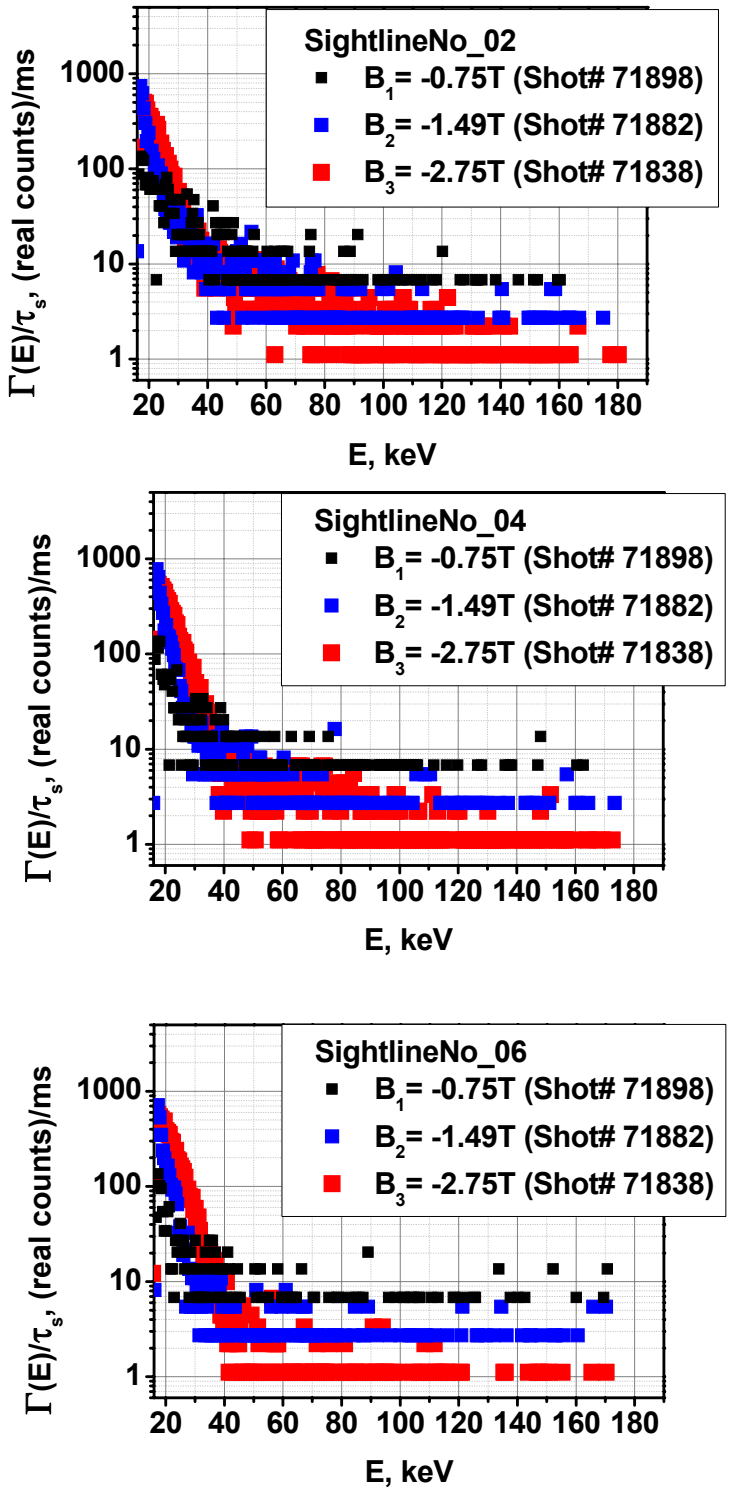

Fig.54 Fast particle spectra measured along SightlineNo 2, 4 and 6 corrected by τ_s for three different magnetic field strength values B_1^- = -0.75T, B_2^- = -1.49T and B_3^- = -2.75T.

As it can be seen from Fig.54 the shape and absolute values of fast particle spectra are different and magnetic field strength increasing leads to improved fast particle confinement. More clearly this effect can be seen from the comparison of the sightlines close to perpendicular region (SightlineNo 20, 19, 18 and 17, where 20th sightline is the closest to perpendicular direction) on Fig.55.

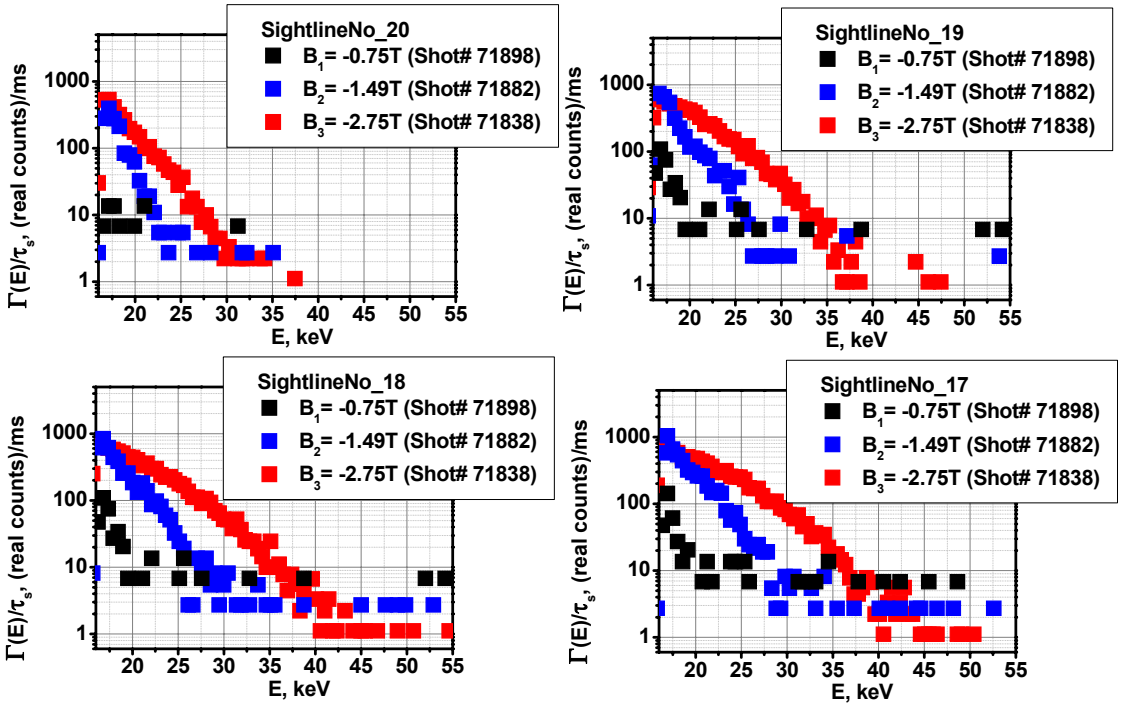

Fig.55 Fast particle spectra measured along SightlineNo 20, 19, 18 and 17 corrected by τ_s for three different magnetic field strength values $B_1^- = -0.75T$, $B_2^- = -1.49T$ and $B_3^- = -2.75T$.

Fig.54 and Fig.55 quantitatively demonstrate that fast particle population was increased in all directions and in the whole range of energies during increase of magnetic field strength. For the cases $B_1^- = -0.75T$ and $B_2^- = -1.49T$ average value of electron density is almost the same, thus increasing of fast particle population in all directions may deal with increasing of magnetic field strength which lead to reducing of the Larmor radius and therefore improved ion confinement. In the case of $B_3^- = -2.75T$ average value of electron density is lower that may lead to increased neutral density. That may also affect on the increasing of the flux from plasma in addition to increased magnetic field strength effect (dependence of the past particle flux from plasma on the electron density, neutral density, etc. is studied in chapter 4).

In addition to that all three cases with different magnetic field strength demonstrated that significant drop of the fast particle flux was observed at the sightlines close to perpendicular direction at 80º÷85º pitch-angle range still remains (Fig.52 and Fig.56).

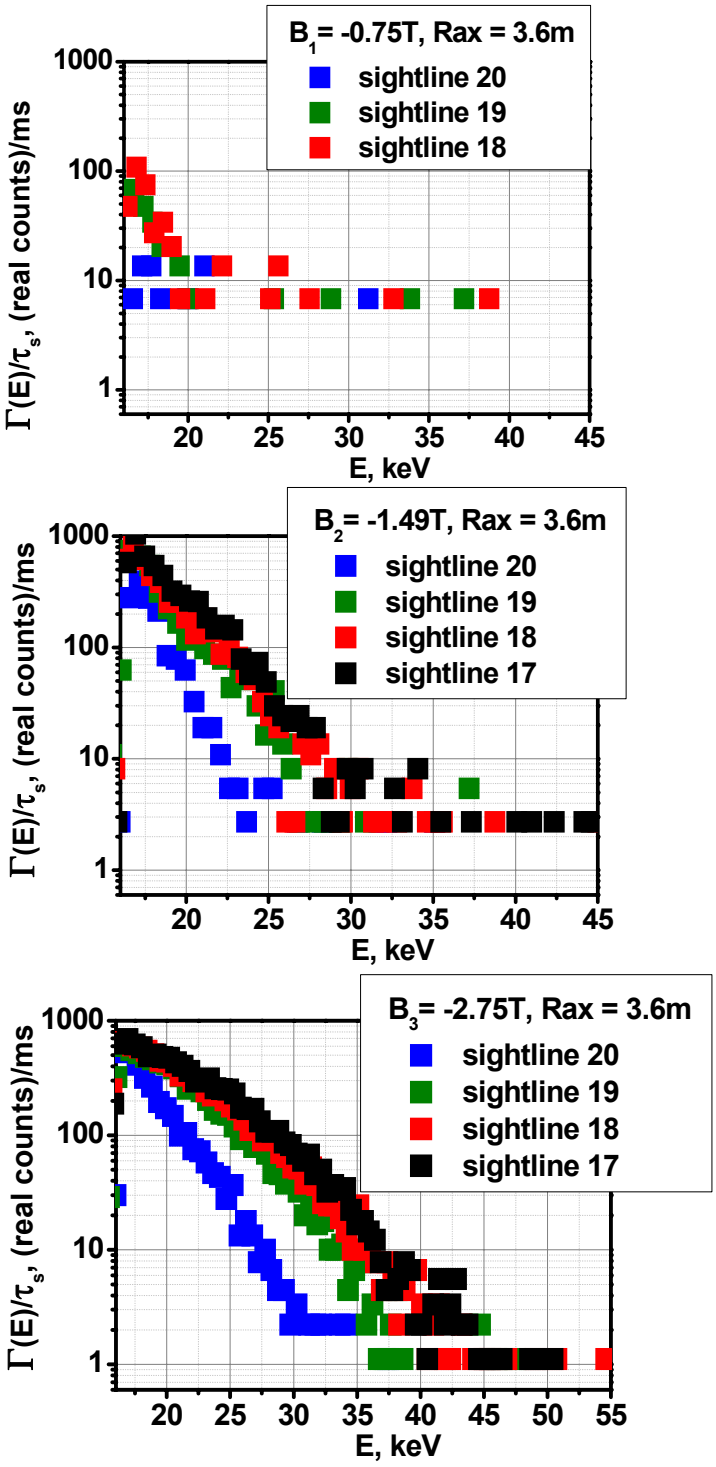

Fig.56 Fast particle spectra for four of the sightlines close to perpendicular direction (sightline 20 is the most perpendicular one) during co-injecting NBI1 operation for three different magnetic field strength values B_1^- = -0.75T, B_2^- = -1.49T and B_3^- = -2.75T.

3.2.1.2 Brief Summary

- Increasing of magnetic field strength leads to broadening of the angular range of suprathermal fast ion tail and to increasing of supratermal fast particle population (mostly in parallel sightlines) in the case of negative magnetic field and co-injecting NBI1.
- Magnetic field strength increasing influences on the increasing of fast particle population in all directions in the whole energy range in the case of negative magnetic field and co-injecting NBI1.
- Although magnetic field strength increasing influences on the increasing of fast particle population in all directions in the whole energy range, it doesn't influence on the disappearance of the possible loss-cone near 80º÷85º pitch-angle range still remains in the case of negative magnetic field and co-injecting NBI1.

3.2.2.1 The case of positive magnetic field and perpendicularly injecting NBI4

As the increasing magnetic field doesn't influence on the disappearance of the drop of the fast particle flux near 80º÷85º pitch-angle range, it was decided to check if the injection of perpendicular directed NBI4 can influence on this region. For this purpose measurements were made in case of positive magnetic field measurements during NBI4. Magnetic axis position in all the cases was Rax = 3.6m. Three values of the magnetic field strength were chosen for demonstration B_1^+ = 1.375T, B_2^+ = 1.5T and B_3^+ = 2.75T. The energy of particles injected bi NBI4 was 40 keV in all cases and the injected power was 2.9MW for the case B_1^+ = 1.375T, 3.1MW for the case B_2^+ = 1.5T and 2.7MW for the case B_3^+ = 2.75T. Time diagrams of the discharges are shown at Fig.57.

B_1^+ = 1.375T, Rax = 3.6m

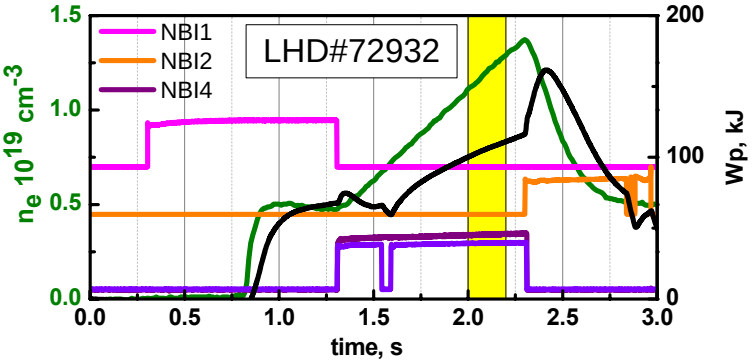

B_2^+ = 1.5 T, Rax = 3.6m

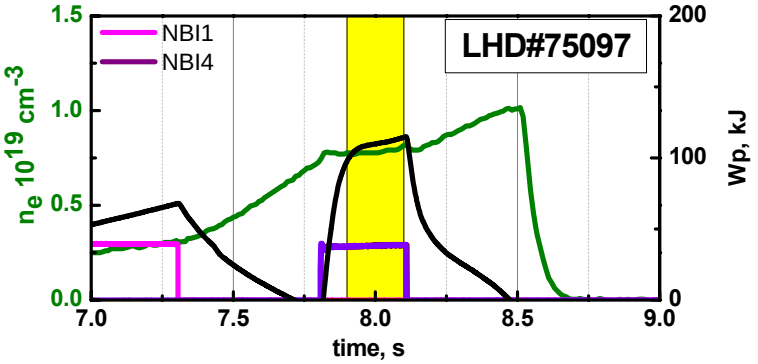

B_3^+ = 2.75 Rax = 3.6m

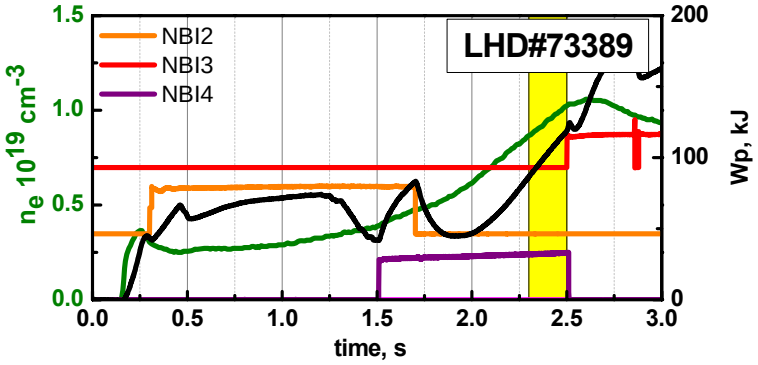

Fig.57 Time diagrams of LHD plasma discharge for three different magnetic field strength values B_1^+ = 1.375T, B_2^+ = 1.5T and B_3^+ = 2.75T.

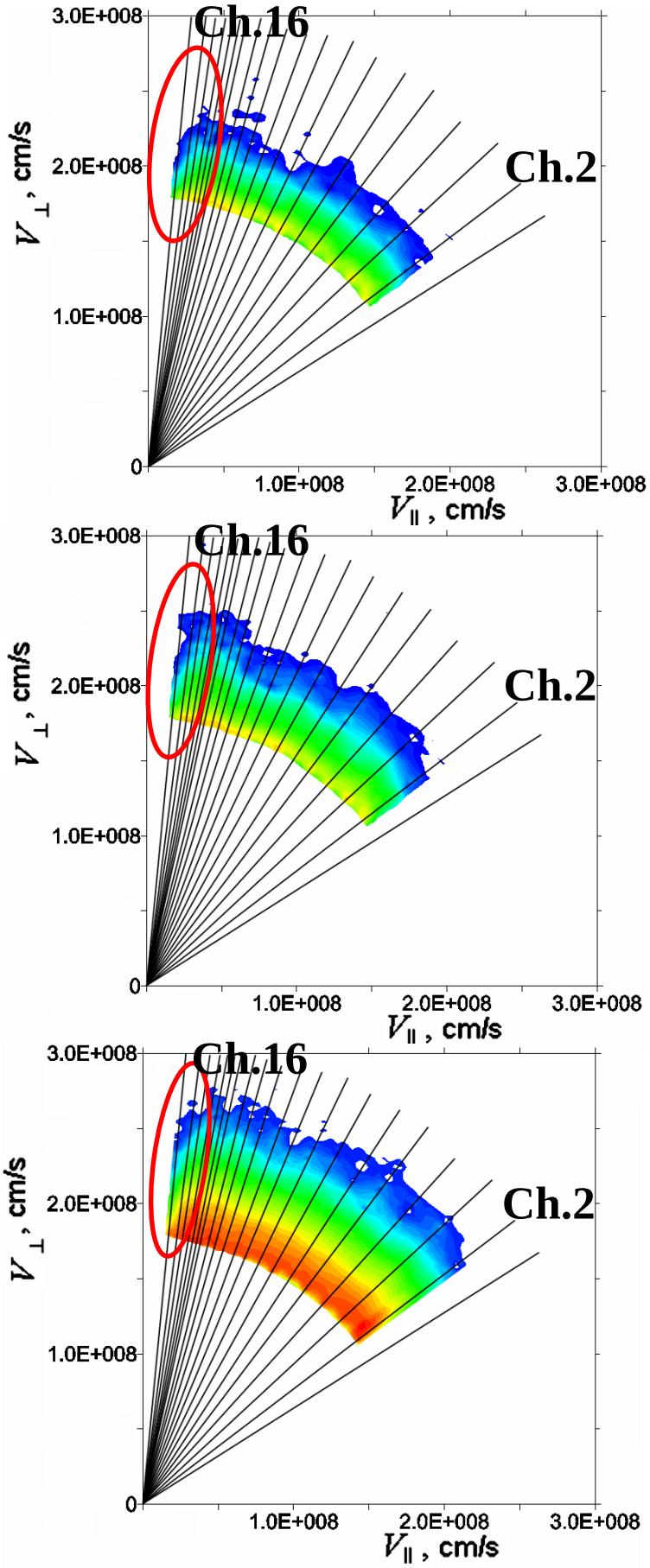

B_1^+= 1.375T, Rax = 3.6m

B_2^+ = 1.5 T, Rax = 3.6m

B_3^+ = 2.75 Rax = 3.6m

Fig.58 Time diagrams of plasma discharges and restored fast particle spectra for marked time intervals for three cases of negative magnetic field B_1^+ = 1.375T, B_2^+ = 1.5T and B_3^+ = 2.75T.

Angular- and energy resolved fast particle spectra were plotted for three cases of magnetic field strength (B_1^+ = 1.375T, B_2^+ = 1.5T and B_3^+ = 2.75T) on Fig.58 in time intervals marked by yellow color at time diagrams of Fig.57. As it can be seen from these pictures increasing of magnetic field strength leads to simultaneous increase of fast particle population in all directions in the whole range of energies. Such increase isn't significant for the case of B_2^+ = 1.5T due to the value of magnetic field strength is close to that on of B_1^+ = 1.375T configuration. Increased magnetic field strength for the case of B_2^+ = 1.5T affects mostly on the region close to perpendicular direction (Fig.59 blue and black dots) because of perpendicular injection of fast particles by NBI4.

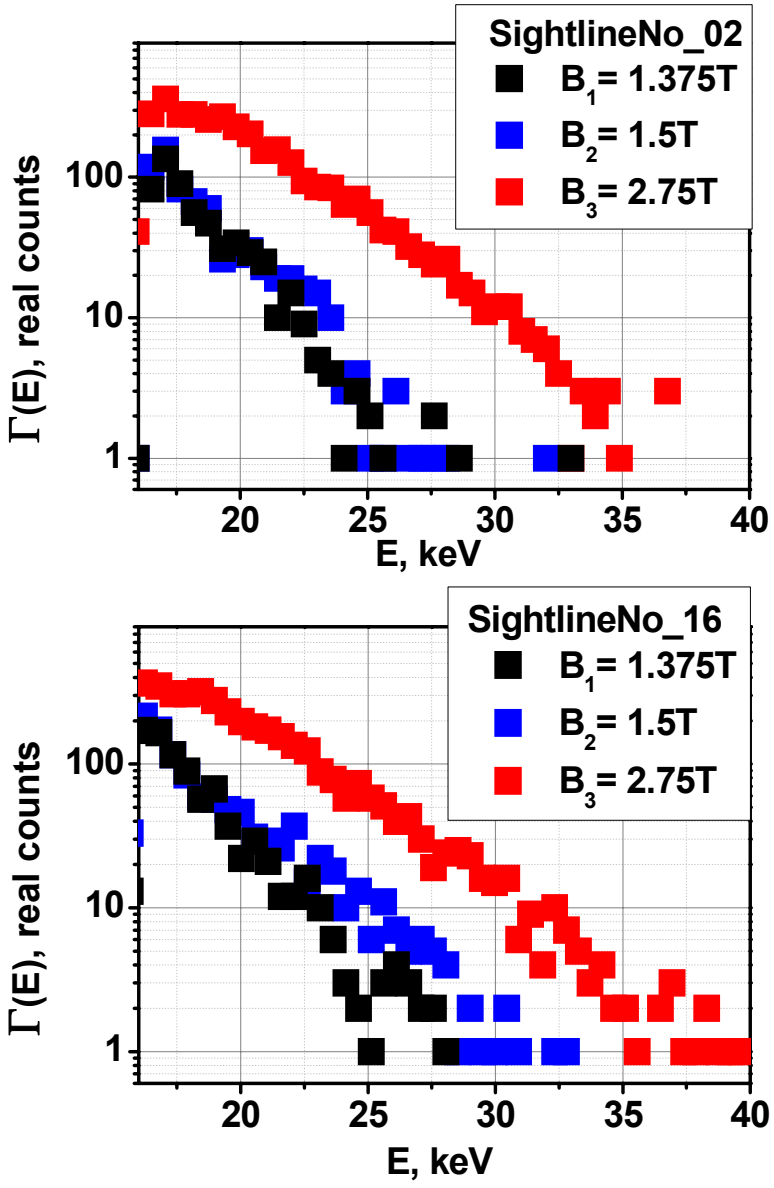

Fig.59 Fast particle spectra measured along SightlineNo 2 and 16 for three different magnetic field strength values B_1^+ = 1.375T, B_2^+ = 1.5T and B_3^+ = 2.75T.

The most significant increase of fast particle population during NBI4 operation was observed for the case of B_3^+ = 2.75T (Fig 59 red dots). At magnetic field strength B_3^+ = 2.75T population of energetic particles in perpendicular direction is slightly higher than in parallel (Fig.60).

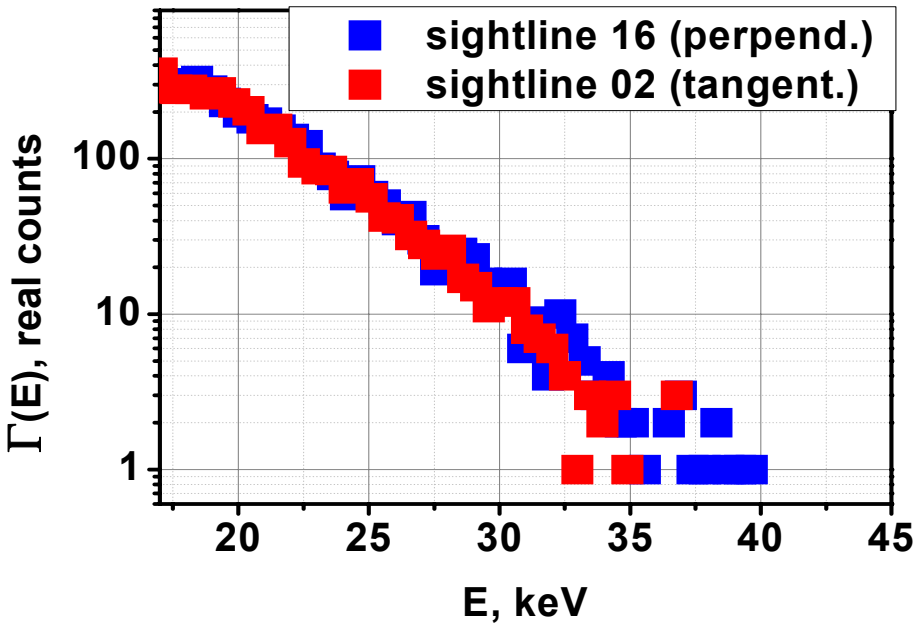

Fig.60 Comparison of perpendicular and tangential sightlines for the case of B_3^+ = 2.75T and perpendicular-injecting NBI4.

In the case of positive directed magnetic field and perpendicularly injecting NBI4 operation the drop of the fast particle flux at 80º÷85º pitch-angle range still remains Fig.58 and Fig.61.

3.2.2.2 Brief Summary

- Increasing of negative or positive magnetic field strength leads to increasing of fast particle population in all directions in the whole energy range in the case of negative magnetic field and co-injecting NBI1.
- Although magnetic field strength increasing influences on the increasing of fast particle population in all directions in the whole energy range, it doesn't influence on the disappearance of the possible loss-cone near 80º÷85º pitch-angle range still remains in the case of negative magnetic field and co-injecting NBI1.
- Neither varying of the injected particles direction, nor direction of magnetic field, nor magnetic field strength doesn't influence significantly on the loss-cone in the direction close to perpendicular.

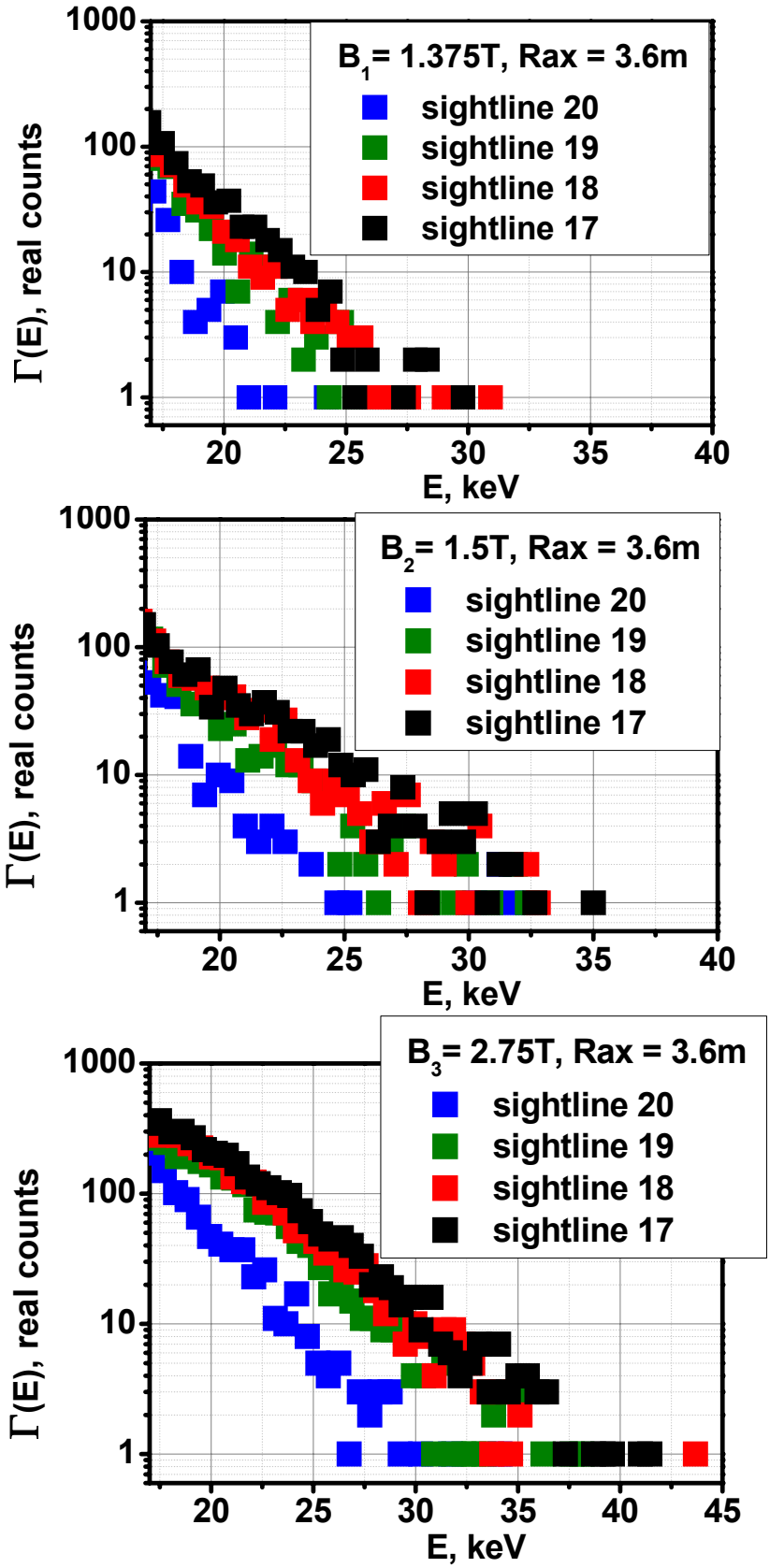

Fig.61 Fast particle spectra for four of the sightlines close to perpendicular direction (sightline 20 is the most perpendicular one) during perpendicularly-injecting NBI4 operation for three different magnetic field strength values B_1^+ = 1.375T, B_2^+ = 1.5T and B_3^+ = 2.75T.

3.3 ICRF EFFECT

3.3.1.1 EXPERIMENTAL RESULTS IN ICRF HEATING REGIMES

As it was concluded in the previous chapter neither varying of the injected particles direction, nor direction of magnetic field, nor magnetic field strength doesn't influence significantly on the loss-cone in the direction close to perpendicular. Thus it was decided to check the influence of the heating by ion-cyclotron radiofrequency (ICRF) on angular distribution of fast particles. The heating time diagrams, density and stored energy behavior during discharge are shown on Fig.62 for plasma with R_{ax} = 3.6m, B = 2.75T.

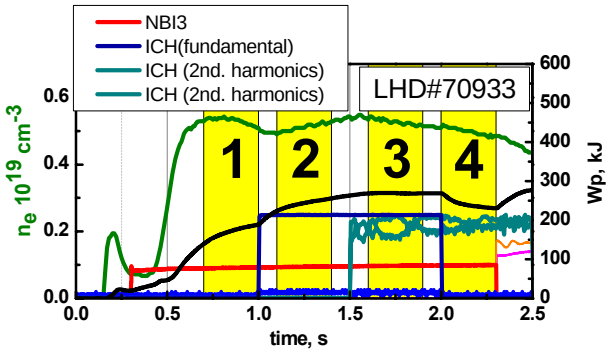

Fig.62 Time diagram of the LHD plasma discharge.

Ch.20

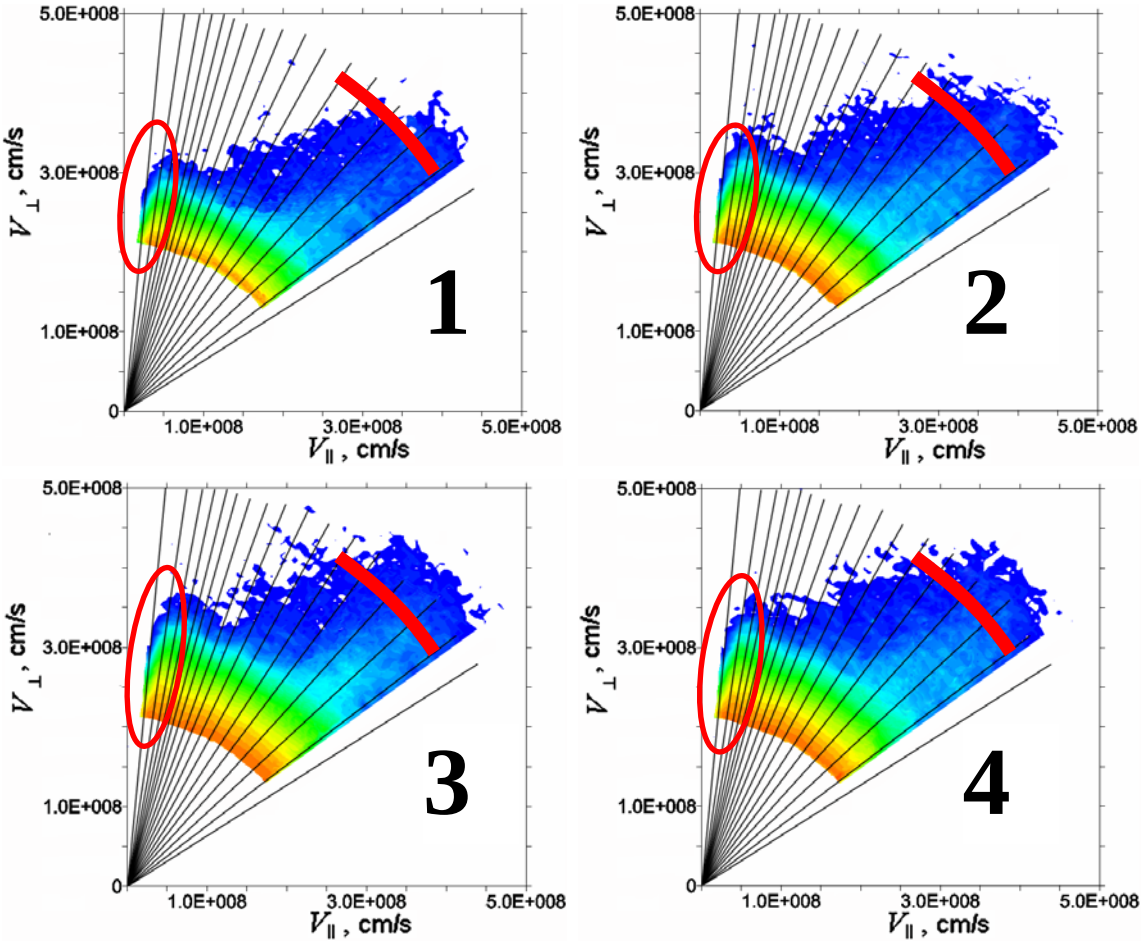

Fig.63 Restored spectra for four time intervals during ICRF heating regime.

The energy of particles injected bi NBI3 was 160 keV and the injected power was 4MW, the ICH power was 1.5MW. For analysis the discharge was divided in four equal time intervals: (1) only NBI3 operation; (2) in addition to NBI3 basic ICRF was added; (3) in addition to NBI3 and basic ICRF the ICRF on the 2nd harmonics was added; (4) basic ICRF switching off. The spectra at Fig.63 demonstrate that ICRF affects in simultaneous increase of fast particle population in all directions (not only perpendicular). Same time, the closest to perpendicular direction two channels demonstrate significant drop of fast particle flux as it can be seen from Fig.64. Blue (cold) gradated colors correspond to the first time interval before switching on of the ICRF for the most perpendicular sightlines 20, 19 and 18; red (warm) gradated colors correspond to the second time interval with basic ICRF for the same sightlines 20, 19 and 18. As it can be seen from this figure switching on of the ICRF influence on increase of the flux in all sightlines but doesn't influence on relative distributions between sightlines 20, 19 and 18.

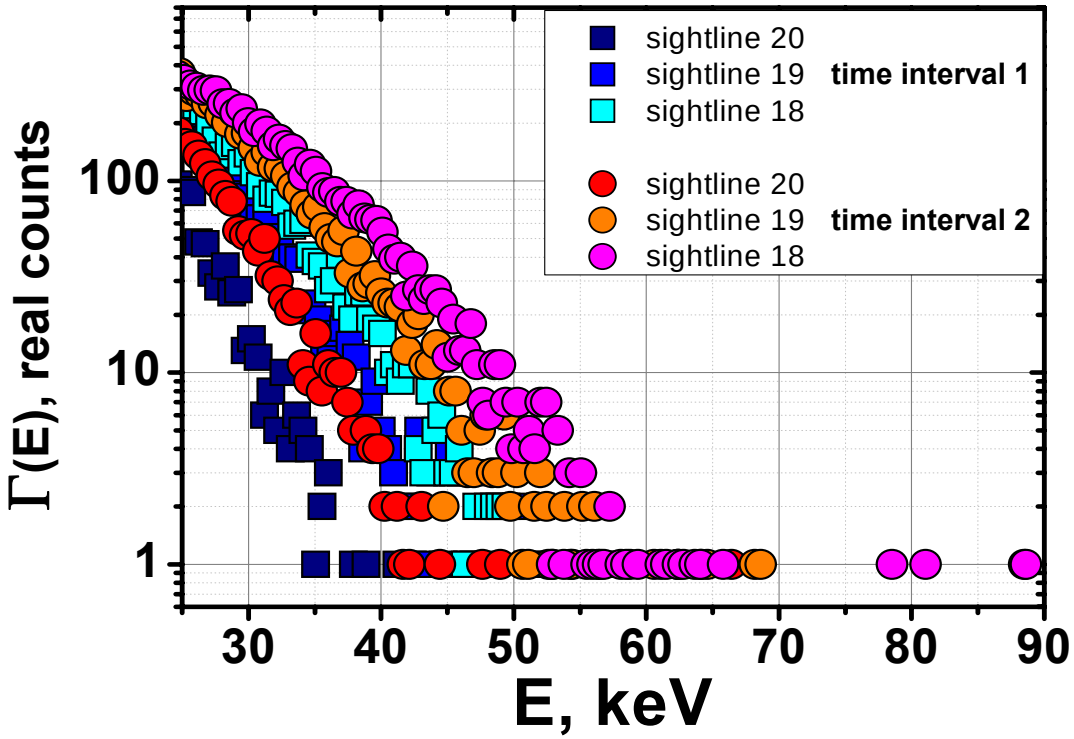

Fig.64 Flux spectra from channels 20, 19 and 18 for the case with only NBI3 operation without ICRF in time interval 1 – blue (cold) gradation of color, and the case of NBI3 with basic ICRF in time interval 2 – red (warm) gradation of color.

Same behavior was observed after switching on the ICRF on the 2nd harmonics in addition to the basic at the 3rd time interval (Fig.65) and in the case of only 2nd ICRF harmonics operation after switching off the basic at the 4th time interval (Fig.66).

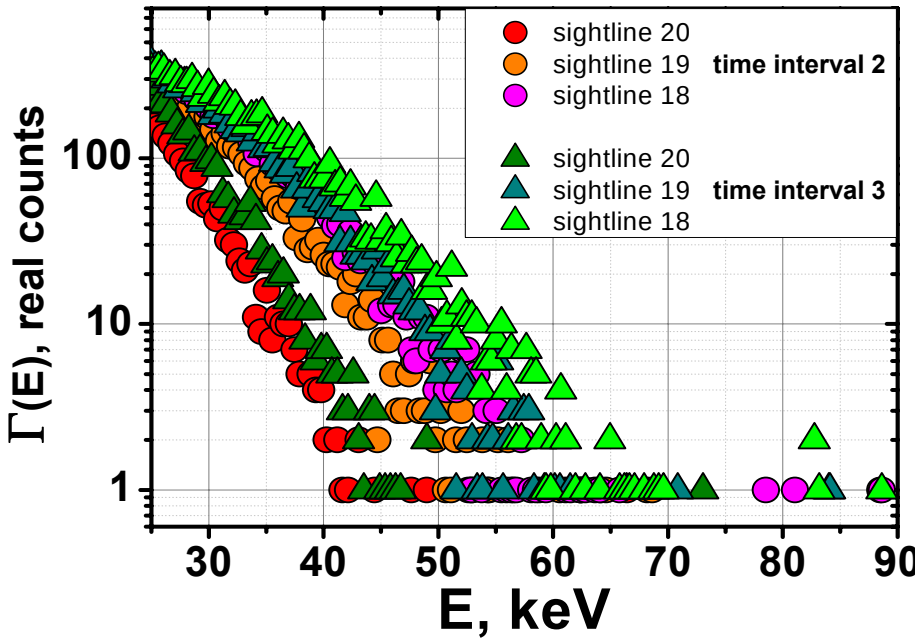

Fig.65 Flux spectra from channels 20, 19 and 18 for the case of NBI3 operation with basic ICRF in time interval 2 – red (warm) gradation of color, and the case of NBI3 with basic and 2nd harmonics ICRF in time interval 3 – green gradation of color.

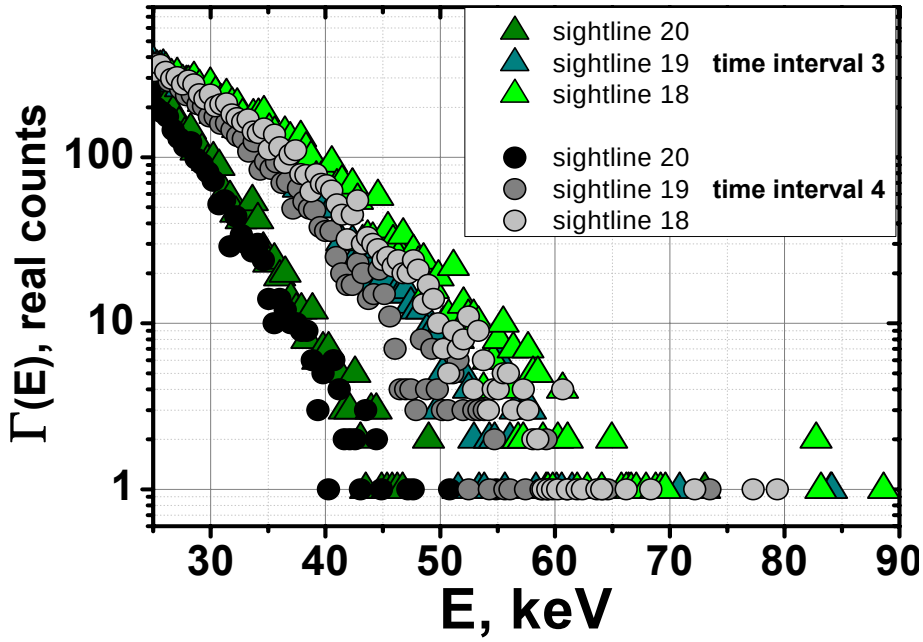

Fig.66 Flux spectra from channels 20, 19 and 18 for the case of NBI3 operation with basic and 2nd harmonics ICRF in time interval 3 – green gradation of color, and the case of NBI3 with only 2nd harmonics ICRF in time interval 2 – red (warm) gradation of color.

Thus the spectra from the most perpendicular 20th sightline always remain much smaller flux than channels 19 or 18, and the spectra form 19th sightline are always of less flux then that ones from the 18th sightline. Spectra from all other sightlines in the energy range 25-55 keV are similar to the spectrum from 18th one. Such significant difference of the spectra at the 20th and 19th sightlines from the other sightlines may be due to presence of the loss-cone in perpendicular direction.

Switching on of the ICRF leads to increasing of fast particle population in all sightlines. Same time ICRF heating leads to broadening of the angular range of suprathermal fast ion tail and to increasing of supratermal fast particle population in parallel and perpendicular sightlines Fig.63.

3.3.1.2 Brief Summary

- Switching on of the ICRF heating in R_{ax} = 3.6m, B = 2.75T magnetic field configuration with counter-injecting NBI3 doesn't lead the disappearance of the possible loss-cone near 80º÷85º pitch-angle range.
- Fast particle population is increasing in all sightlines during ICRF heating.
- ICRF heating influences on the broadening of the angular range of suprathermal fast ion tail
- Supratermal fast particle population is mostly increased in parallel and perpendicular sightlines.

3.3.2.1 EXPERIMENTAL RESULTS IN NBI4+ICRF HEATING REGIMES

As it was demonstrated in previous chapters loss-cones in 80º÷85º pitch-angle range can not be suppressed by only NBI4 heating or by switching on of the ICRF heating only. Thus comparison of experimental data measured for the case of perpendicular directed NBI4 and a combination of NBI4 with ICRF was made to check how the joint work of these two types of heatings may affect on the possible loss-cone region. For this purpose two shots with close parameters in same plasma conditions were chosen. The heating time diagrams, density and stored energy behavior during discharge are shown on Fig.67 for plasma with R_{ax} = 3.6m, B = 1.375T. NBI4 port through power in Shot# 72867 (without ICRF) was $P_{port\text{-}through}$ = 2.2MW, in Shot# 72878 (with ICRF) was $P_{port\text{-}through}$ = 2.75MW, the ICH power was P_{ICH} = 1.8MW. Fast particles spectra are plotted on Fig.68 for time intervals marked by yellow color on time diagrams of the Fig.67.

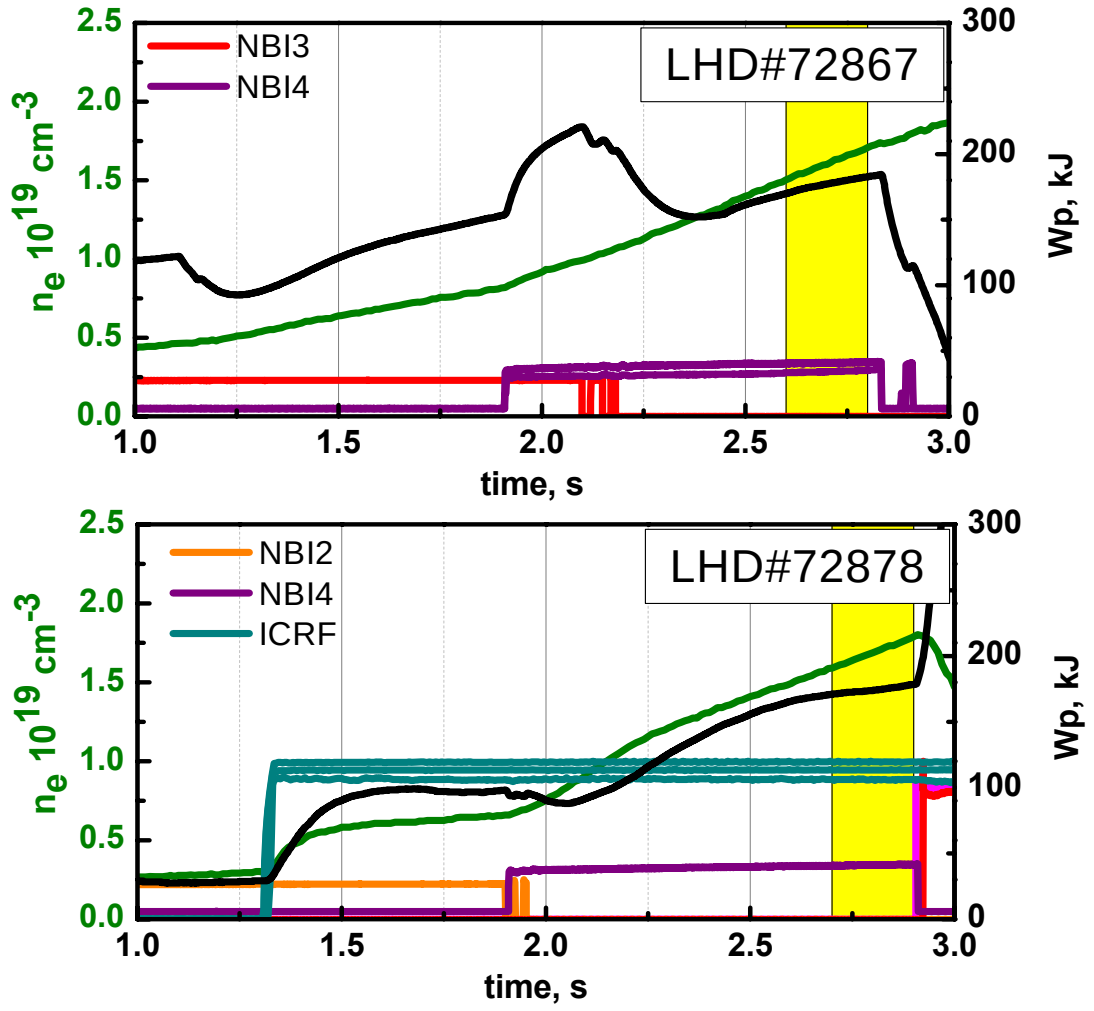

Fig.67 Time diagram of the LHD plasma discharge without ICRF (Shot# 72867) and with ICRF (Shot# 72878).

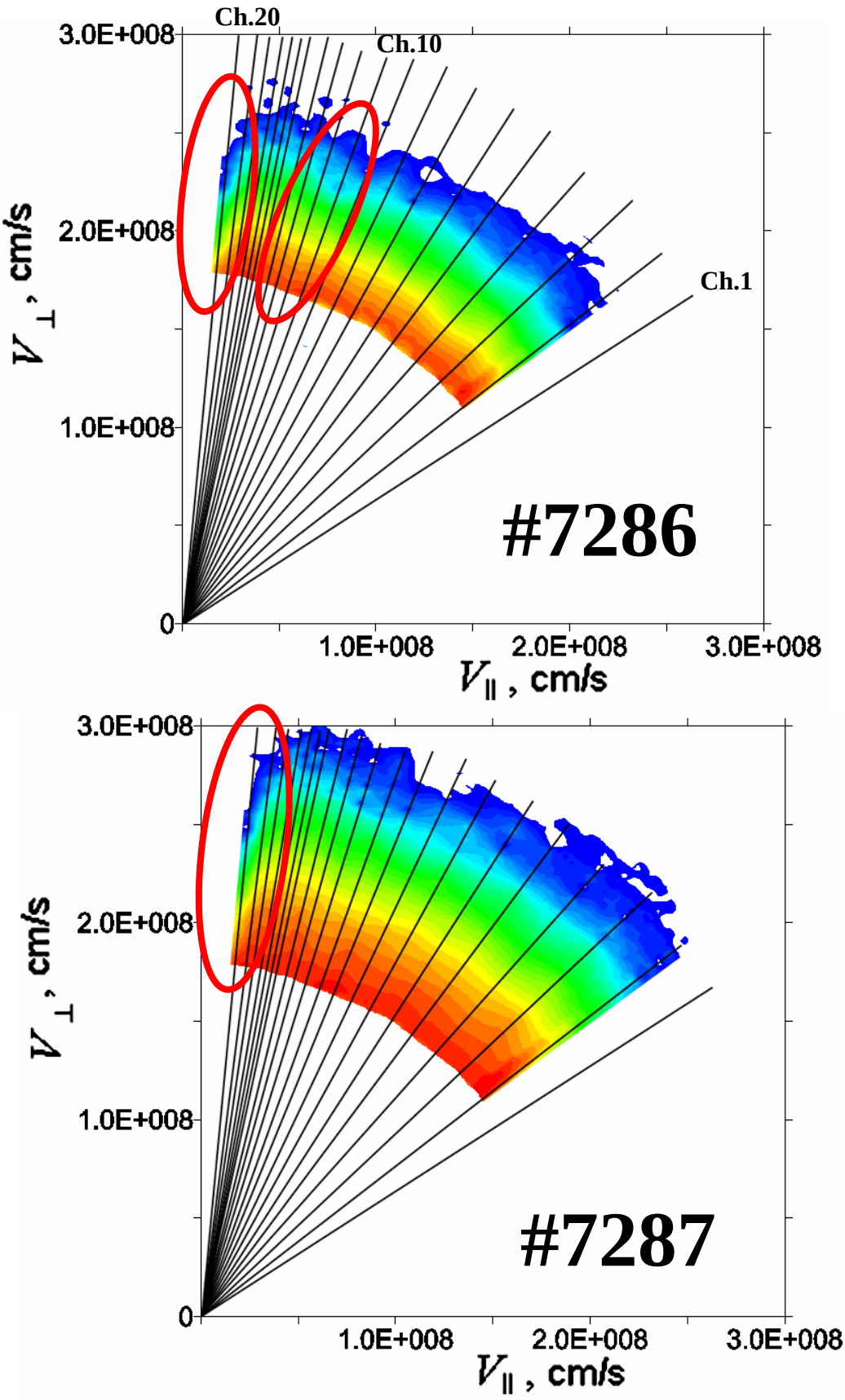

Fig.68 Restored spectra for the case of only NBI4 heating (Shot# 72867) and for the case of NBI4 with ICRF (Shot# 72878).

In the case of the only NBI4 heating (Shot# 72867) perpendicular sightlines (No20, 19 and 18) still demonstrate lower flux in comparison with other sightlines. In addition to that in the current magnetic field configuration additional peculiarity in the region of the 10th sightline has appeared – drop of the fast particle flux Fig.69.

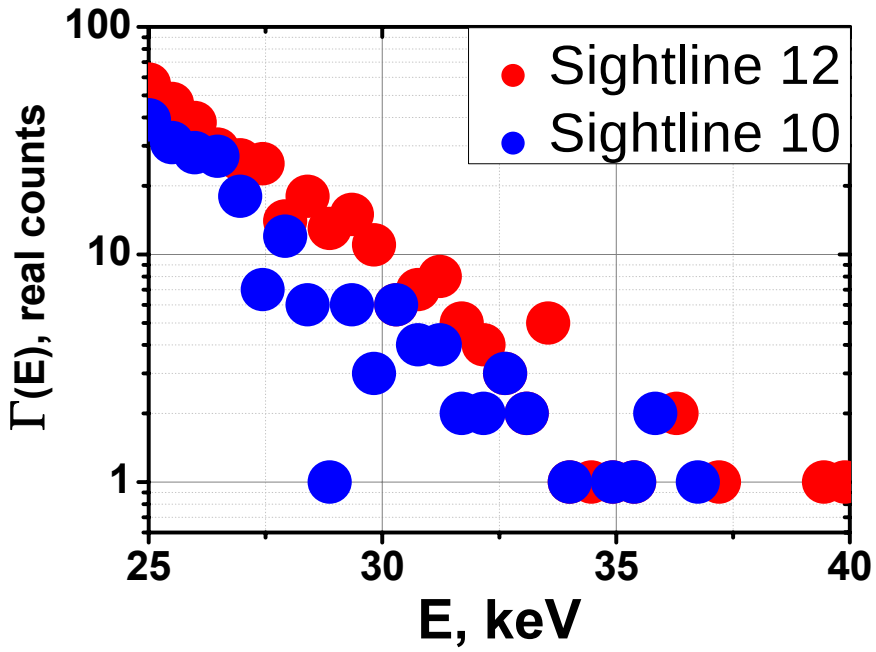

Fig.69 Spectra obtained from the 10th and 12th sightline in the Shot# 72867 with only NBI4 heating.

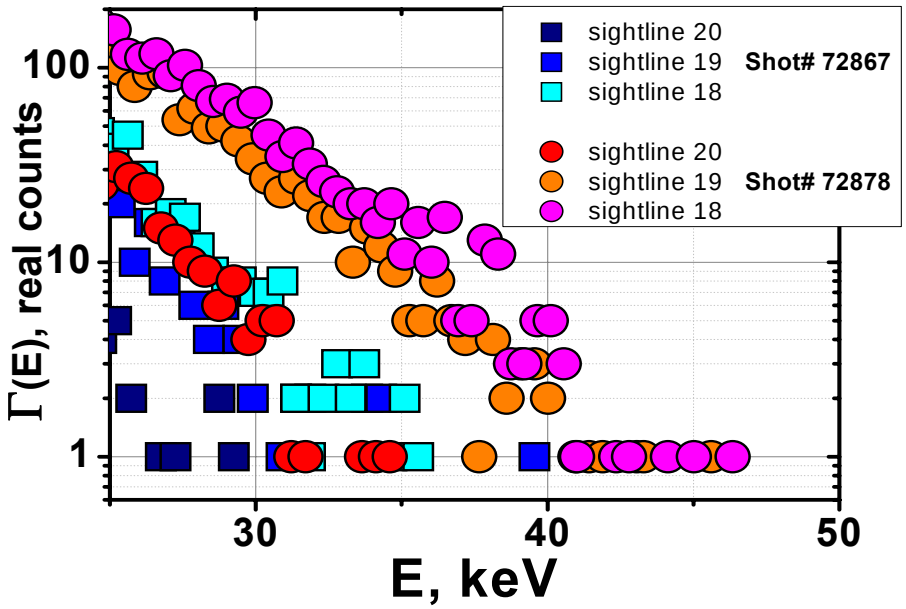

Fig.70 Flux spectra from channels 20, 19 and 18 for the case of the only NBI4 – blue (cold) gradation of color, and the case of NBI4 with ICRF – red (warm) gradation of color.

Increasing of NBI4 port-through power and switching on of the ICRF led to increasing of the flux in all directions in ShotNo 72878; spectra in the 10th sightline region were aligned with spectra from other sightlines (2 ÷18) up to the uniform shape, but fast particle population in the region of the 19th and 20th sightlines still remained smaller in comparison with other sightlines Fig.70. Probable reason to such a behavior is the presence of loss-cone region in perpendicular direction. Although spectrum from the 19th sightline still remained below the 18th one, after increasing NBI4 port-through power and switching on of the ICRF the relative value of them has slightly increased to get closer to the spectrum from the 18th sightline (orange and pink dots on Fig.70). This may be due to reducing of the shape of loss-cone region due to slightly improved confinement (still to be checked in further experiments).

3.3.2.2 Brief Summary

- Joint operation of perpendicularly-injecting NBI4 and of ICRF heating in R_{ax} = 3.6m, B = 1.375T magnetic field configuration doesn't lead to the disappearance of the possible loss-cone near 80º÷85º pitch-angle range.
- ICRF influences on increasing of fast particle population in all sightlines.
- ICRF heating may be effective in suppressing of small possible loss-cone regions and in aligning of angular an-uniformity.
- Increasing of NBI4 port-through power and switching on of the ICRF may reduce the shape of loss-cone region due to slightly improved confinement

3.4 Angular anisotropy of perpendicular region.

In the current chapter experimental data from the 9th experimental campaign will be presented [25]. At that time diagnostic was installed at another position available to make horizontal scan of perpendicular region of distribution function with very good angular resolution (0.6º between the sightlines). Pitch angle values along scanning sightlines for that position are shown on Fig.32(a) by black colored lines. The very initial spectra were made only by two detector segments scanning plasma in perpendicular direction and tangential direction Fig.71.

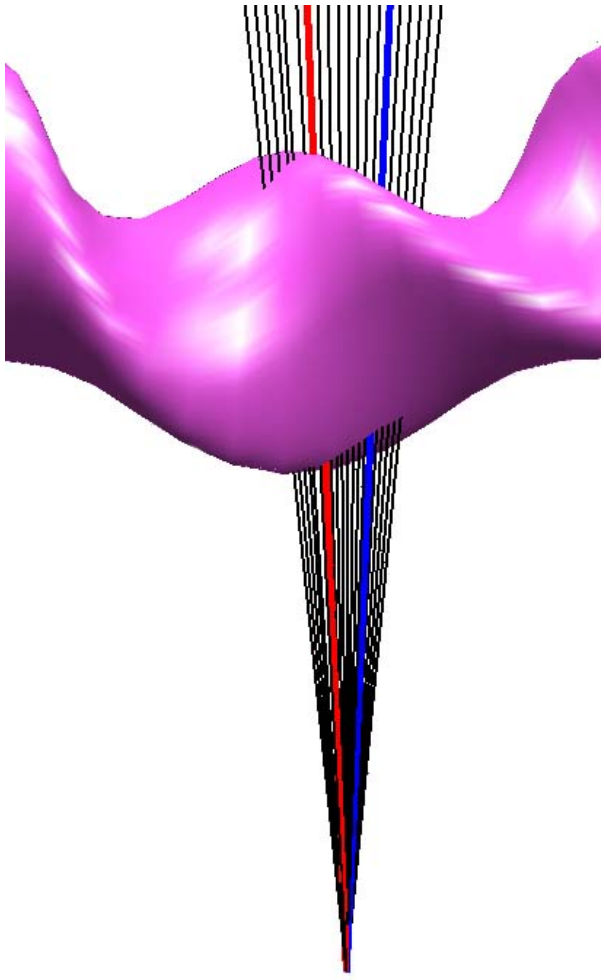

Fig.71 Illustration of plasma column and two scanning sightlines in perpendicular direction (red line) and slightly tangential direction (blue line).

Pitch angles along the viewing directions of the sightline scanning in perpendicular direction (red line) and in slightly tangential direction (blue line) are show in Fig.72. Average pitch angle of the sightline scanning plasma column in perpendicular direction is 92 degrees and the one of the sightline scanning plasma in tangential sightline is 85 degrees.

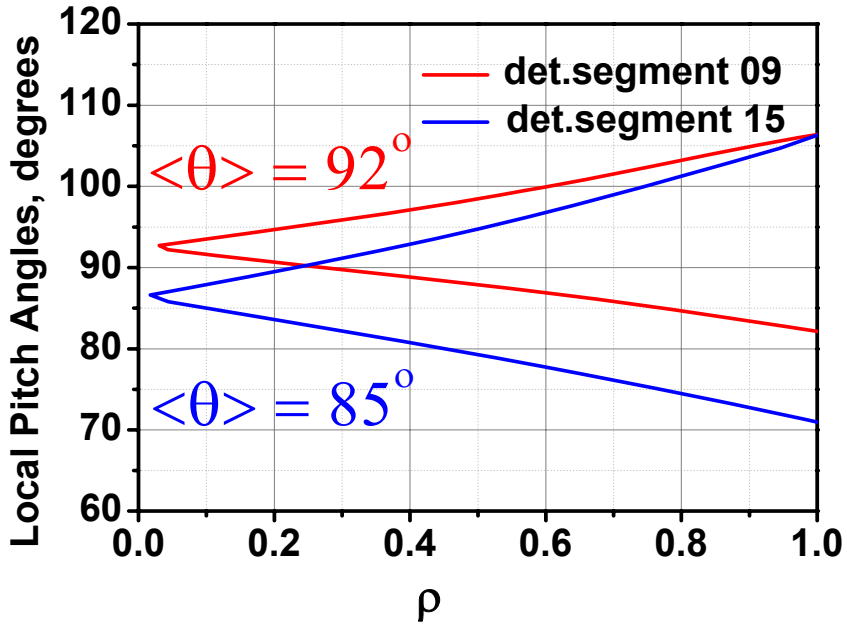

Fig.72 Pitch angles along the viewing direction of the sightline scanning in perpendicular direction (red line) and in slightly tangential direction (blue line).

3.4.1 Experimental results with in perpendicularly-injecting NBI4 regimes

First measurements by new diagnostic were made in the regime with perpendicularly injecting NBI4 operation in plasma with Rax = 3.6 and B = 2.75T. The neutral particle flux measured by these channels and its response to the perpendicular NBI4 heating can be clearly seen on the time diagram in Fig.73(a). Figure 73(b) shows the tangential and perpendicular NBI operation times and general discharge wave forms.

The discharge was divided in three equal time intervals and fast particle spectra were restored for the case of only co-injecting NBI2 (time interval 1), the case of co-injecting NBI2 and perpendicularly injecting NBI4 (time interval 2) and the case of counter-injecting NBI1 and NBI3. Restored spectra are shown at Fig.74.

Fig.74 Demonstrates that in all three cases fast particle population at the tangential sightline with average pitch angle θ = 85º is smaller than at perpendicular sightline. In addition to that the restored energy distributions demonstrate that the more perpendicular sightline of the detector (red dots) is more sensitive to the perpendicular NBI4 heating than the detector section closer towards the tangential observation.

Counter-injecting NBI1 and NBI3 demonstrated a stronger angular dependence compared to co-injected NBI2.

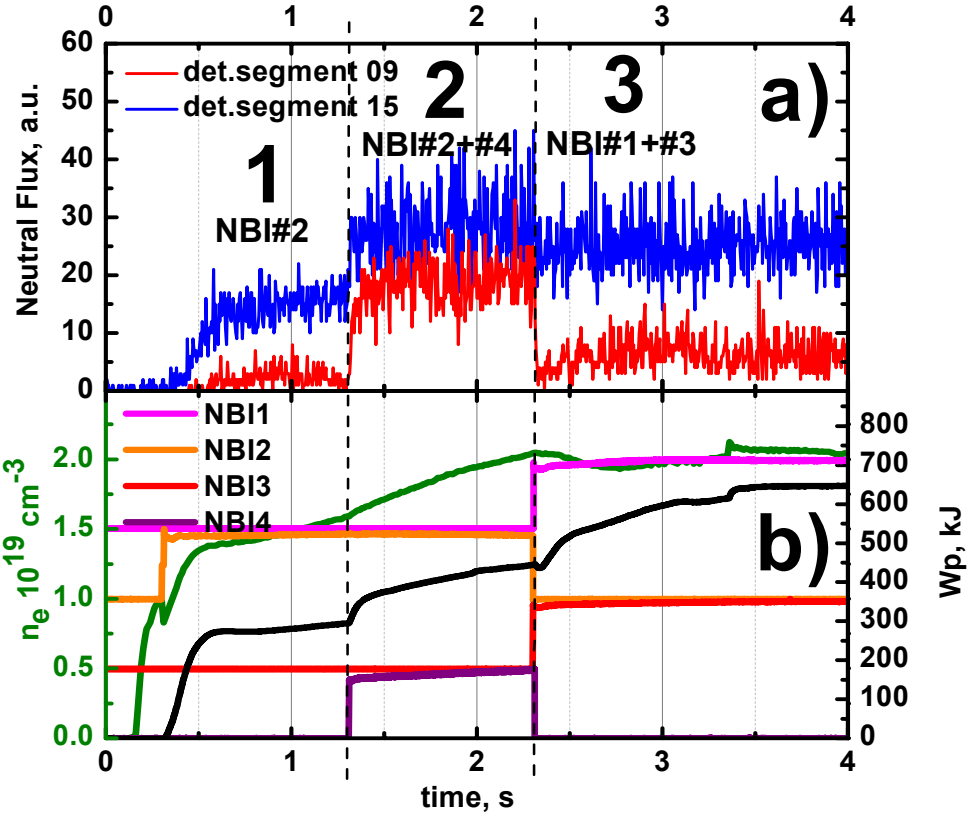

Fig.73 Time diagram of the LHD plasma discharge. (a) Charge exchange neutral particle flux during the discharge measured by two different detector segments (red curve - perpendicular sightline and blue curve - tangential sightline). (b) Yellow - tangential NBI2 operation time; purple - perpendicular NBI4 operation time; green curve - electron density *ne*; and black curve - stored energy *Wp*.

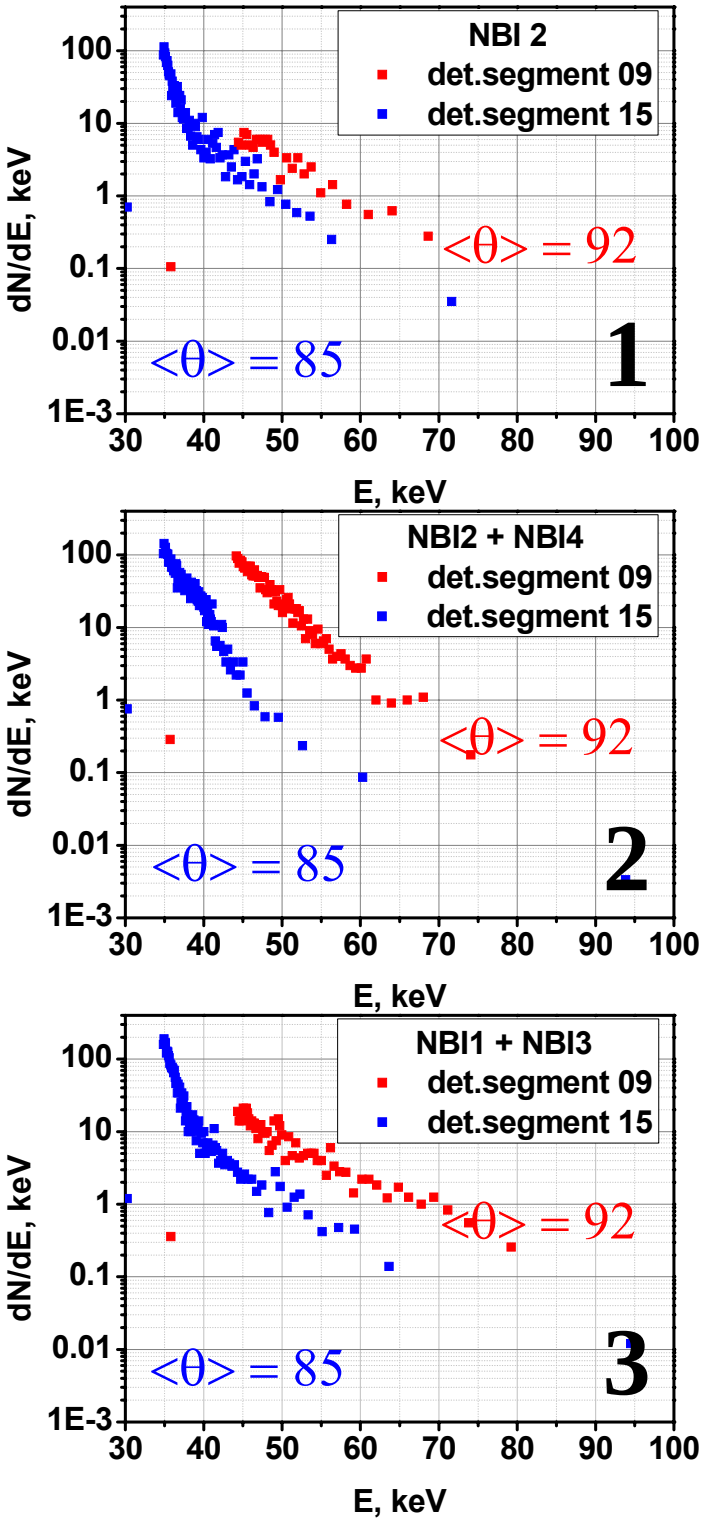

Fig.74 Restored spectra for three different NBI heating schemes: (1) tangential NBI2 only. (2) Tangential co-injecting NBI2 combined with perpendicular NBI4. (3) Combination of tangential counter-injecting NBI1 and NBI3. In all three cases red dots correspond to perpendicular sightline and blue dots to tangential sightline.

3.4.2 Experimental results in ICRF heating regimes

Initial measurements were made in regimes with ICRF heating too. The time diagram for the discharge with ICRF is shown at Fig.75.

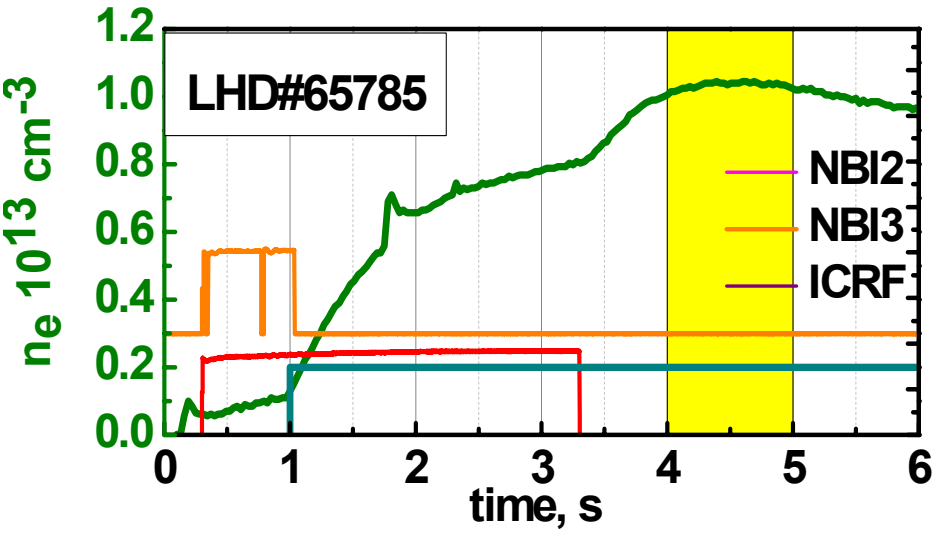

Fig.75 Time diagram of the LHD plasma discharge without ICRF heating.

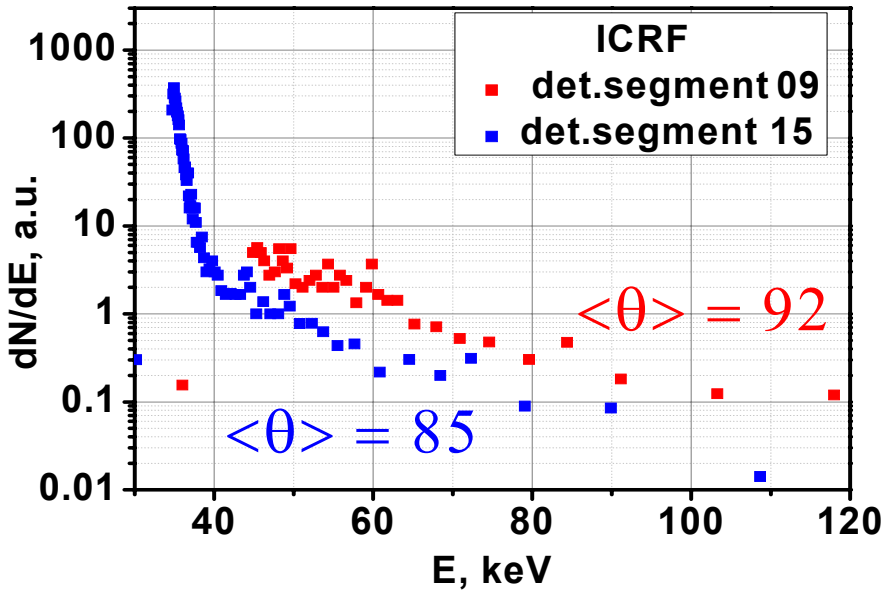

Fig.76 Restored spectra for the case of ICRF heating. Red dots correspond to perpendicular sightline and blue dots to tangential sightline.

The restored spectra for the case of ICRF heating is shown on the Fig.76. It can be seen that during ICRF heating the fast particle population at slightly tangential sightline with average pitch angle θ=85° still remains smaller in comparison with almost perpendicular sightline.

Thus, the initial data obtained by new ARMS-NPA diagnostic in the very beginning of it's operation in 9th cycle experimental campaign demonstrate that fast particle spectra from the sightline with average pitch angle θ=85º demonstrate reduced fast particle population. Hence in the case of combined measurements from two possible diagnostic positions the angular distribution function with loss-region should look qualitatively like on the Fig.77. Measured loss-region correlates with numerical results for helical systems [32] (Fig.78).Calculations are made for l = 2 heliotron with helical field period number M = 14.

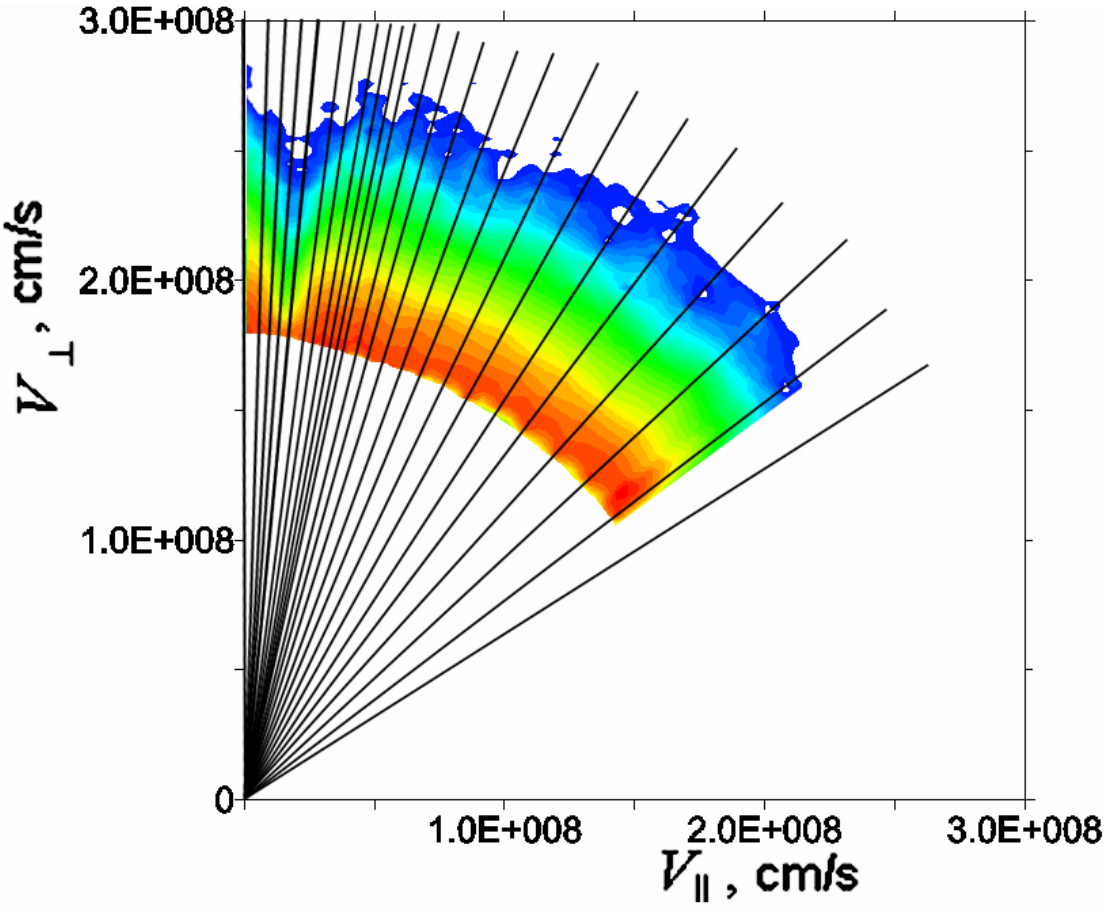

Fig.77 Qualitative image of obtained angular distribution function which can be achieved in the joint measurements from two possible diagnostic positions.

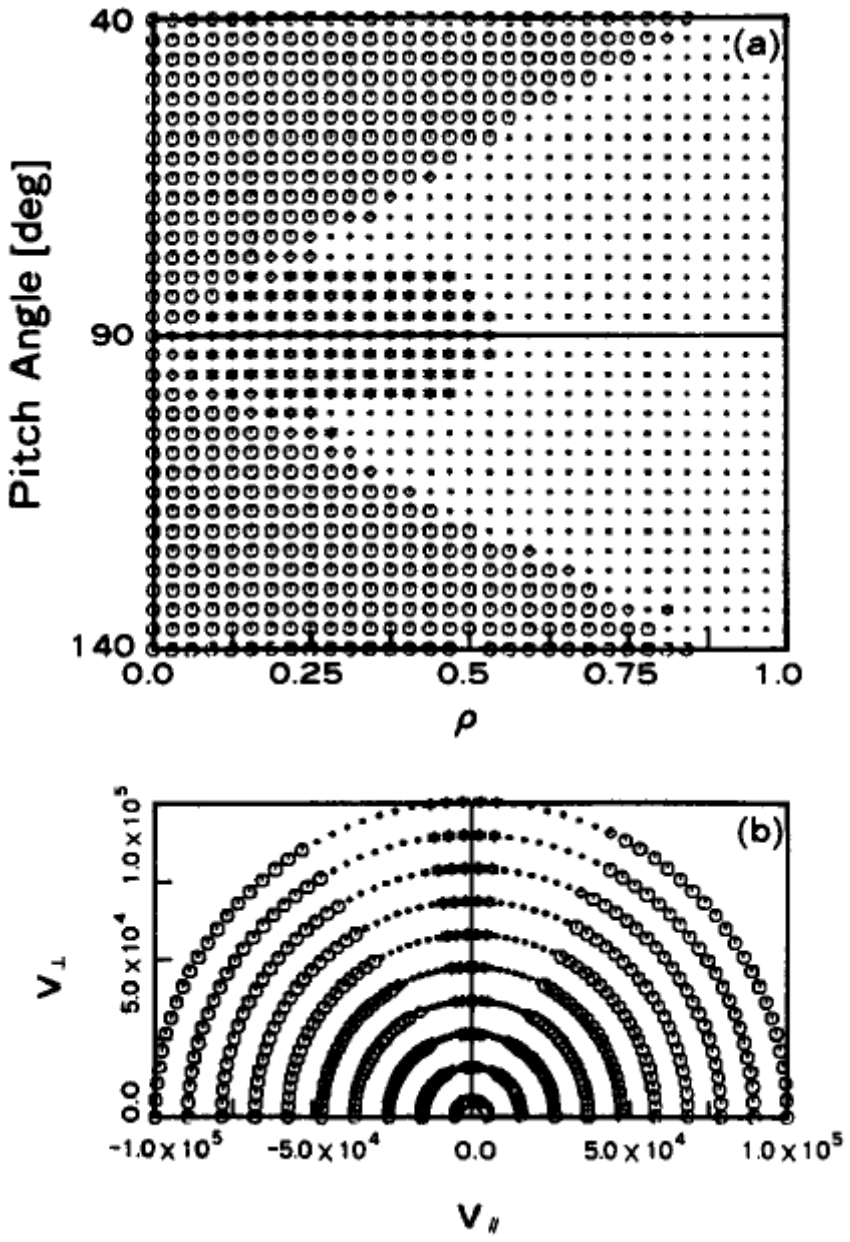

Fig.78. Numerical results of the loss-region in both (a) configuration and (b) velocity space at $\rho = 0.5$ outside the torus in the case of $\varphi = 0$. Results are obtained by solving the drift equations.

3.4.3 Brief Summary

- Preliminary experiments with horizontal scan of perpendicular region of distribution function show that population at the tangential sightline with average pitch angle $\theta = 85^{\circ}$ is smaller than at perpendicular sightline with average pitch angle $\theta = 92^{\circ}$. Such effect was observed for any type of heating i.e. co-injecting NBI, counter-injecting NBI, perpendicularly-injecting NBI and ICRF.
- Restored energy distributions demonstrate that the more perpendicular sightline of the detector (red dots) is more sensitive to the perpendicular NBI4 heating than the detector section closer towards the tangential observation.
- Precise scan with all 20 channels is required to check more detailed the perpendicular region of distribution function.
- Experimentally measured loss-cone region coincide with numerical calculations.
- Some sightlines may intersect with the region of energetic particles. This may increase the signal on intersecting sightlines and reduce at the sightlines which don't intersect with it.

3.5 ECH EFFECT

3.5.1 EXPERIMENTAL RESULTS IN ECH REGIMES

In order to understand the influence of different types of heating on the angular distribution on fast particles the measurements were made in ECH regimes. All data presented in this part of the 3.5 Chapter were measured in the inward shifted magnetic field configuration with strong negative magnetic field R_{ax} = 3.575m, B = -2.870T. Time diagram for one of the discharges with ECH is shown on Fig.79. ECH was switched on during counter-injecting NBI2 operation.

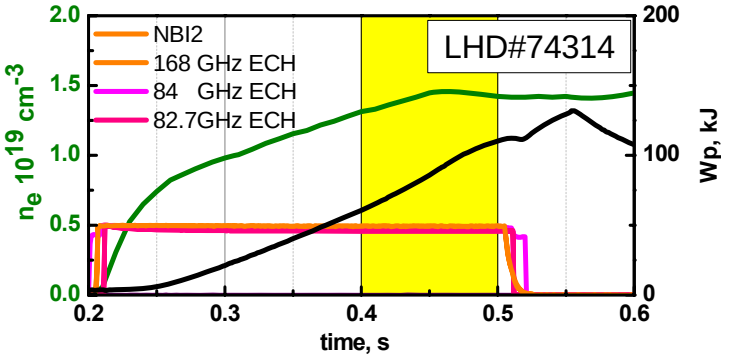

Fig.79 Time diagram of the LHD plasma discharge with ECH.

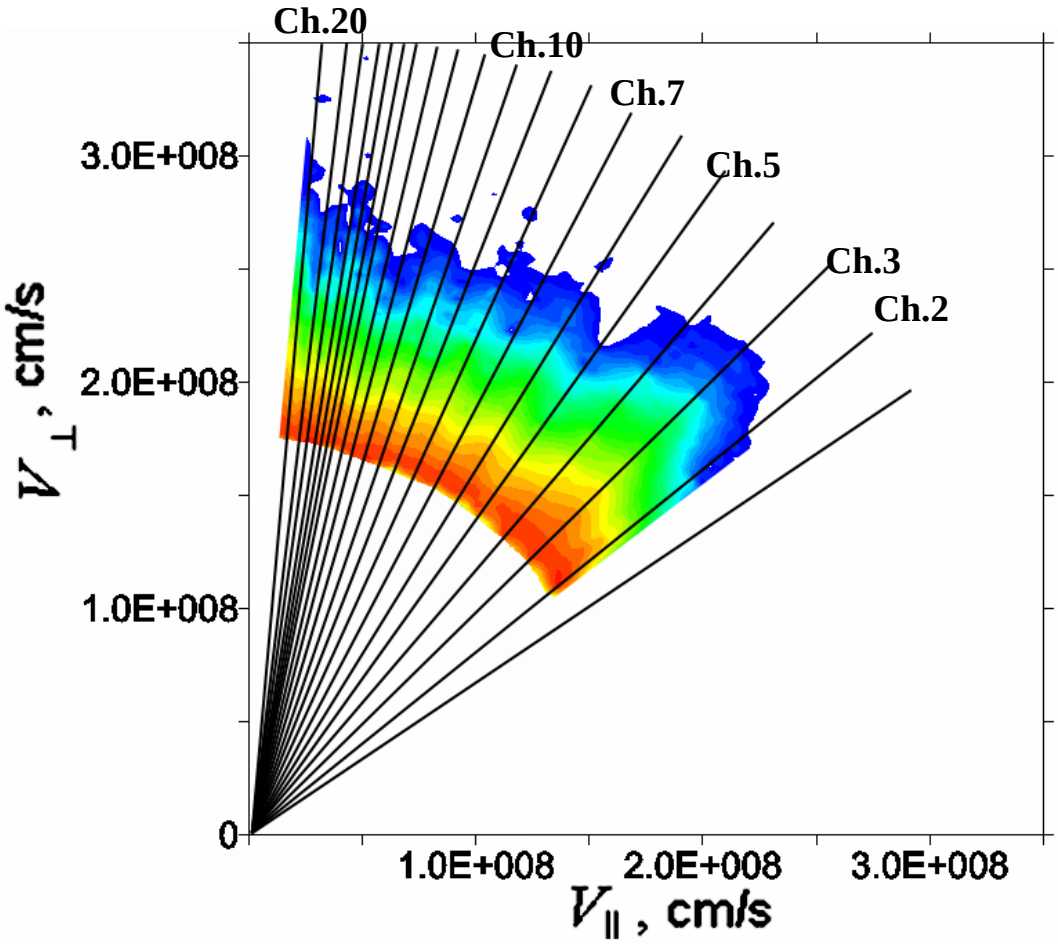

Fig.80 Restored spectra of fast particles during counter-injecting NBI2 and ECH.

Fast particle spectra were restored for the time interval marked by yellow color on Fig.79 and plotted on Fig.80. As it can be seen (qualitatively from the Fig.80 and quantitatively from Fig.81) switching on of the ECH may significantly influence on the angular distribution of fast particles. This may be due to possible loss-cones which couldn't be observed in other conditions. As it can be seen from the Fig.80 and Fig.82, switching on of the ECH has significantly influenced on the flux from along the 20th and 19th sightlines. This could happen due the influence of electric field or the electron temperature profile produced by ECH.

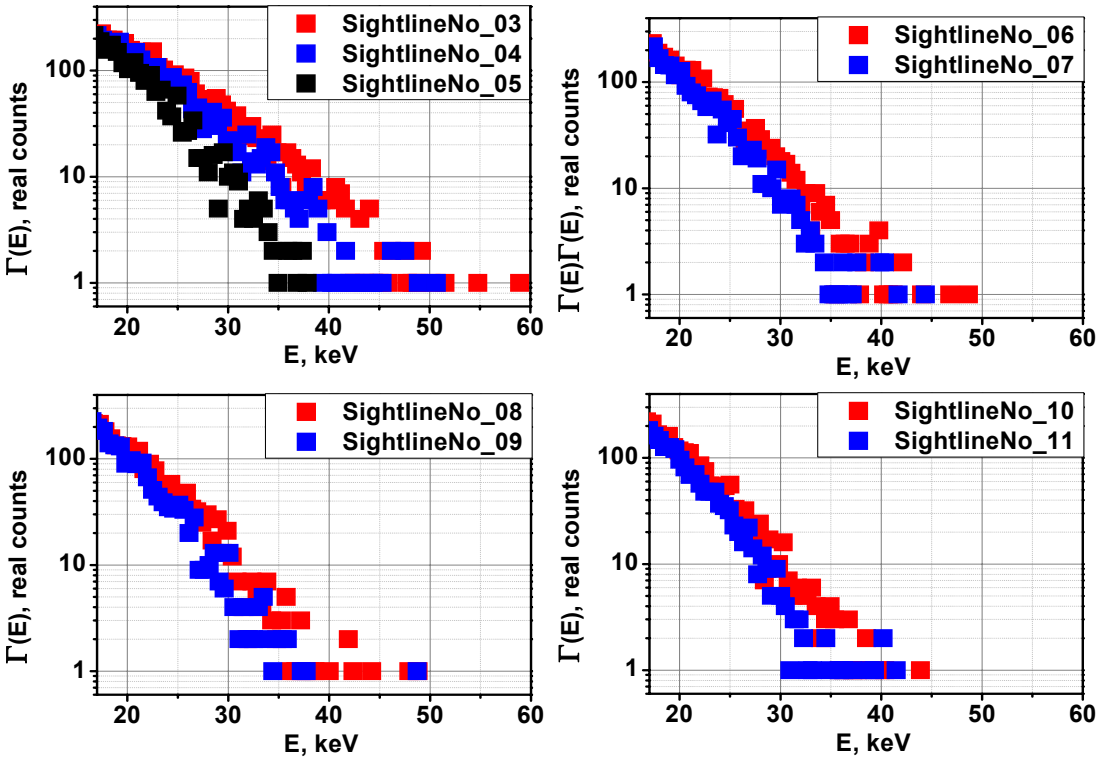

Fig.81 Angular anisotropy of fast particle spectra measured along 03÷11 sightlines.

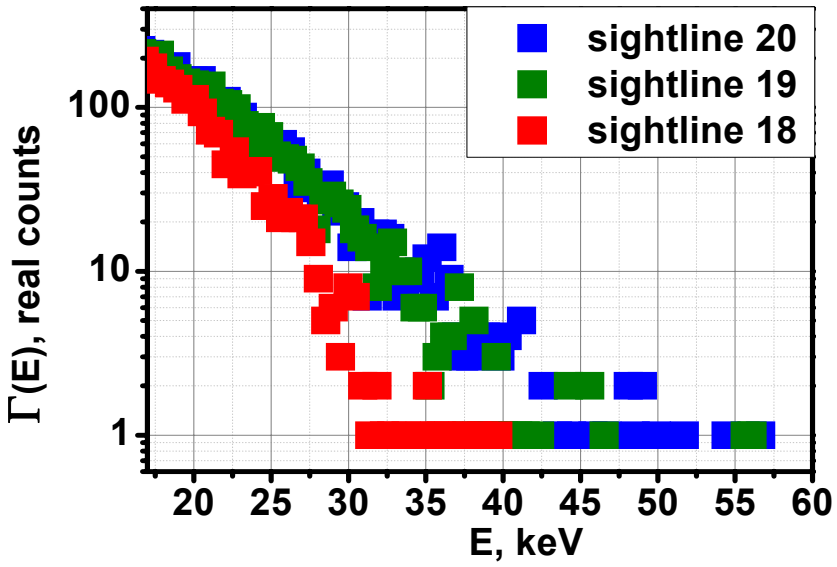

Fig.82 Flux spectra from channels 20, 19 and 18 for the case with only NBI3.

3.5.2 Comparison of ECH heating effect with NBI4

Comparison of the fast particle spectra during ECH and perpendicularly-injecting NBI4 was made to check the angular distribution in the same discharge with same plasma conditions and same plasma parameters. Time diagram of the plasma discharge is shown on Fig.83. The energy of particles injected bi NBI4 was 40 keV and the injected power was 5.7MW.

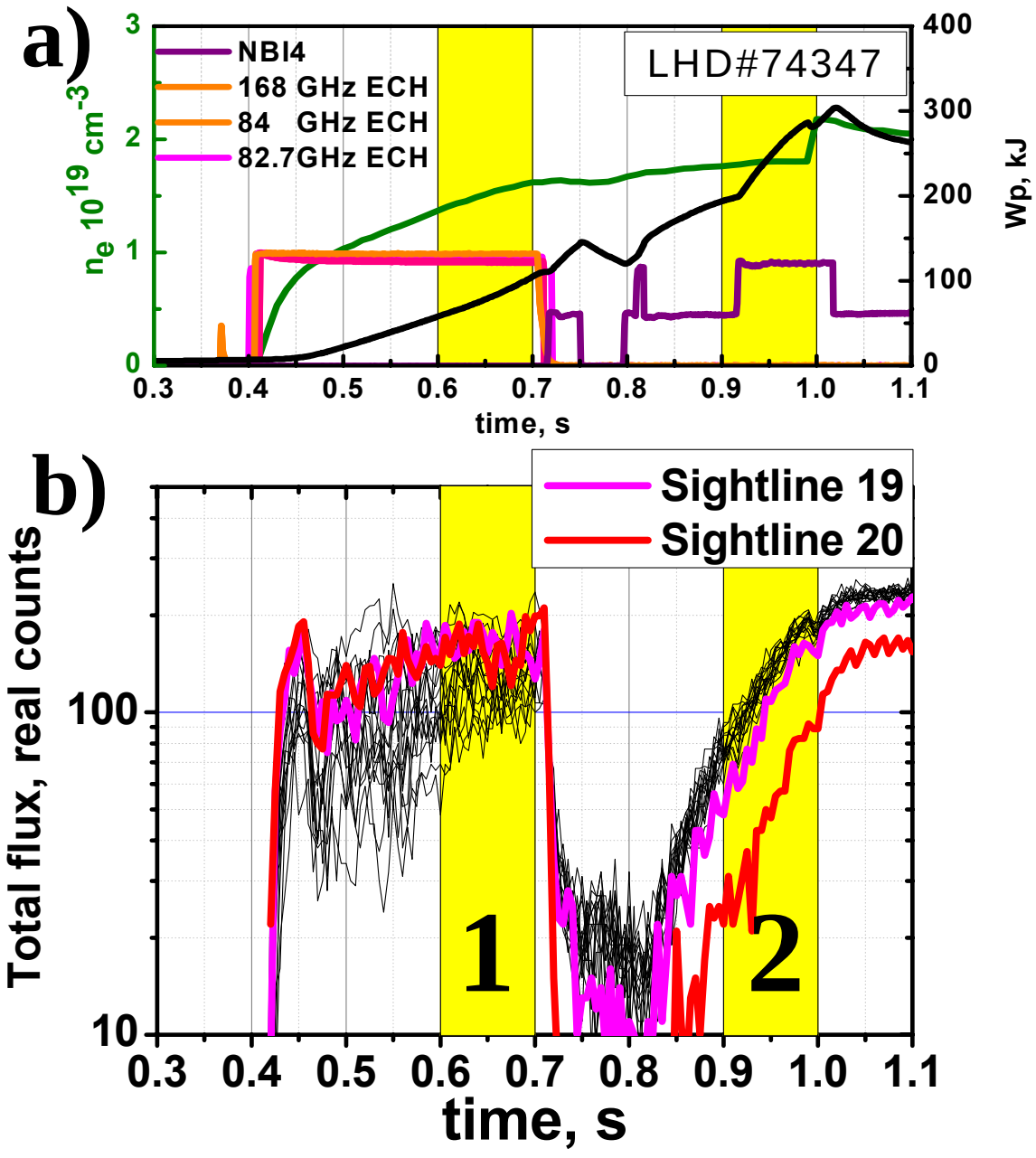

Fig.83 Time diagram of the LHD plasma discharge. (a) Violet - perpendicular NBI4 operation time; orange and magenta – ECH operation time; green curve - electron density *ne*; and black curve - stored energy *Wp*. (b) Charge exchange neutral particle flux during the discharge measured by 19 different detector segments (red curve – 20th sightline and magenta curve – 19th sightline).

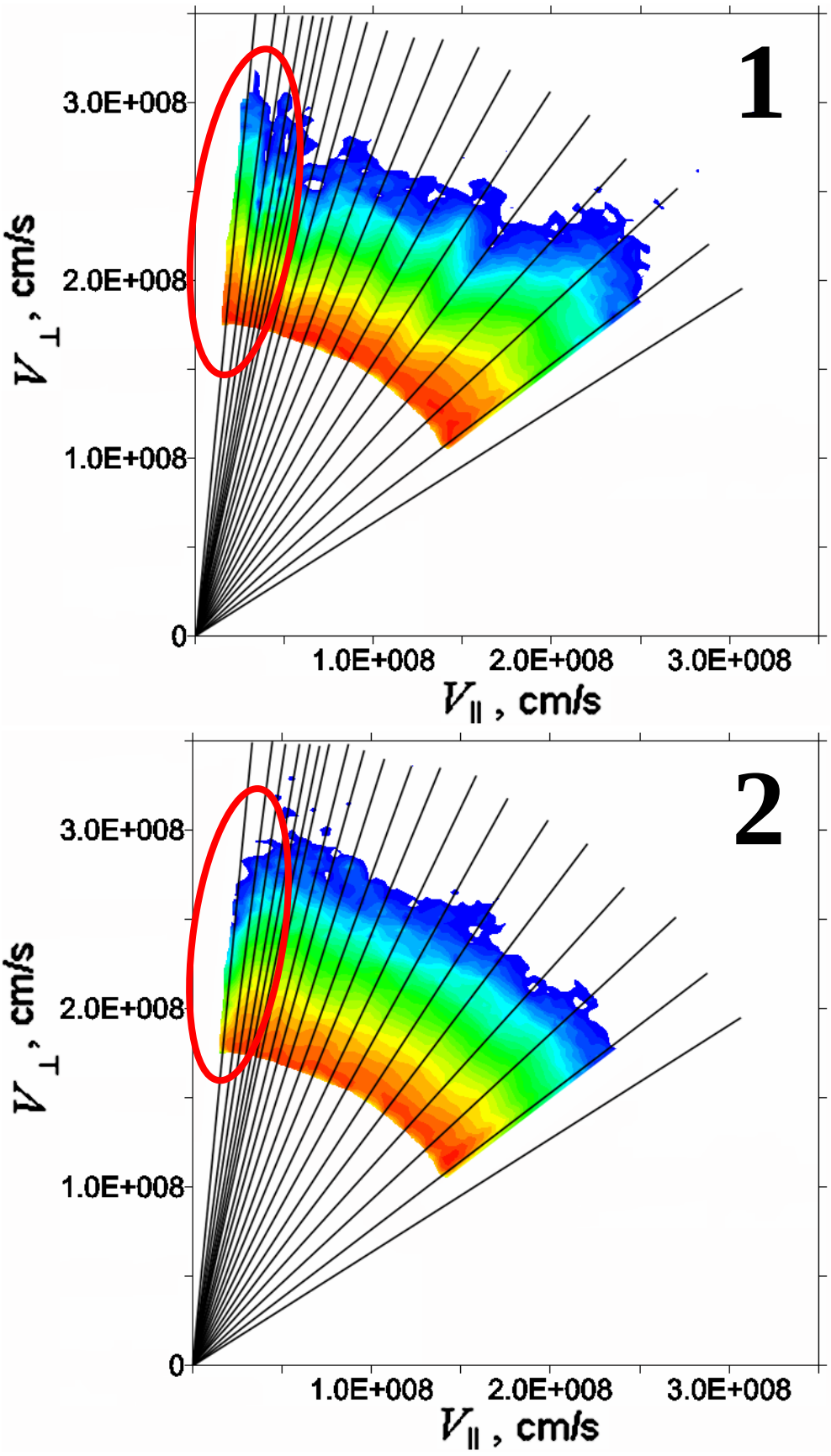

Fig.84 Restored angular-resolved spectra of fast particles for time interval 1 and 2 of the Fig.83 correspondingly.

As it can be seen from Fig.84 ECH can significantly influence on the angular distribution and can significantly increase the fast particle population in the sightlines close to perpendicular direction, as it is shown on Fig.85 where the fast particle flux from 18^{th}, 19^{th} and 20^{th} sightlines is compared. NBI4 operation leads to uniform angular distribution along all sightlines except sightlines close to perpendicular direction - 18^{th}, 19^{th} and 20^{th} which demonstrate reducing of the fast particle population along these sightlines (Fig.85).

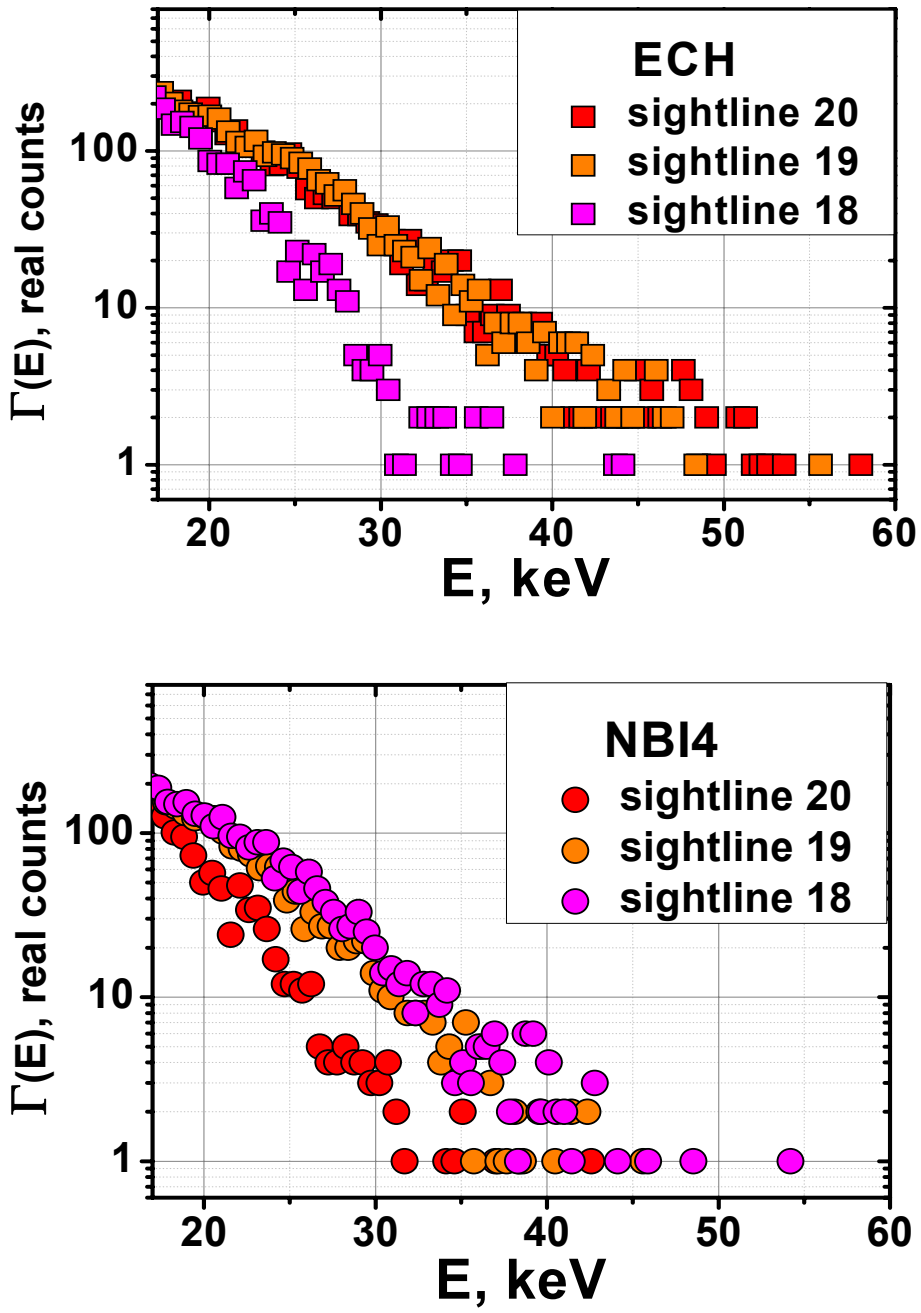

Fig.85 Flux spectra from channels 20, 19 and 18 for the case of NBI2 with ECH.

The reason to such behavior may be changes in electric field produced by ECH switching on as it is shown on Fig.86 [47].

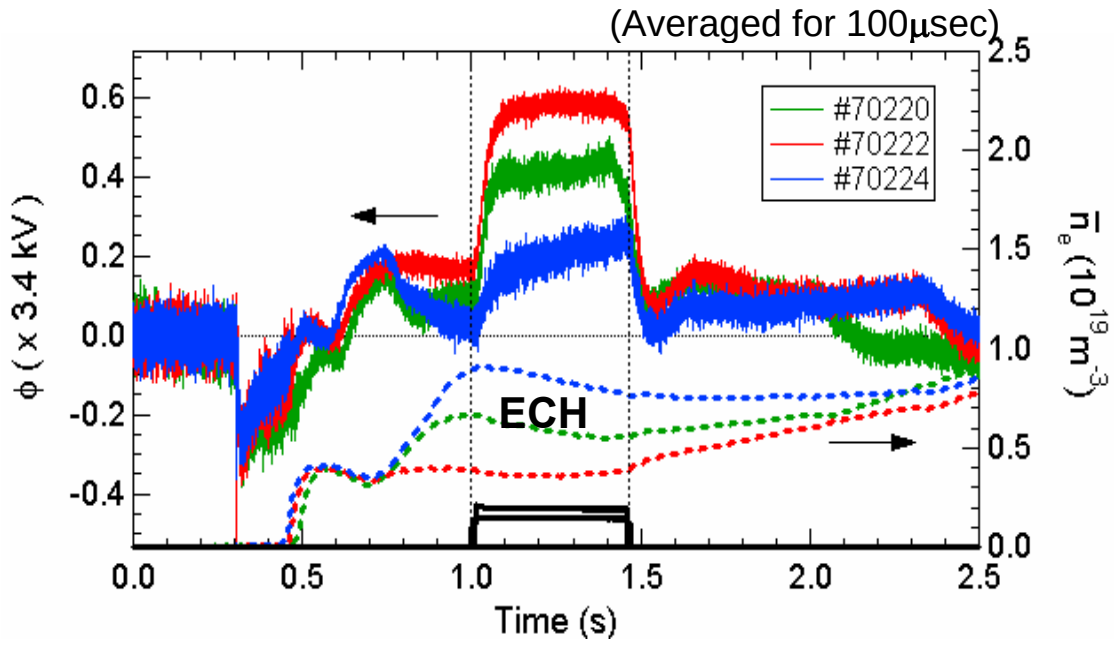

Fig.86 Time diagram of the potential behavior in time (solid lines) and electron density (dashed lines)

As it was mentioned in Chapter 3.5.1 the electron temperature profile may significantly influence on the loss-cone region. Fig.87 demonstrates electron density and temperature profiles for time interval 1 (red dots) and 2 (black dots). It can be seen that in the case when ECH is applied the electron temperature profile is peaked (red dots) and in the case when only NBI4 is working electron temperature profile is smooth and has a hill-shaped form.

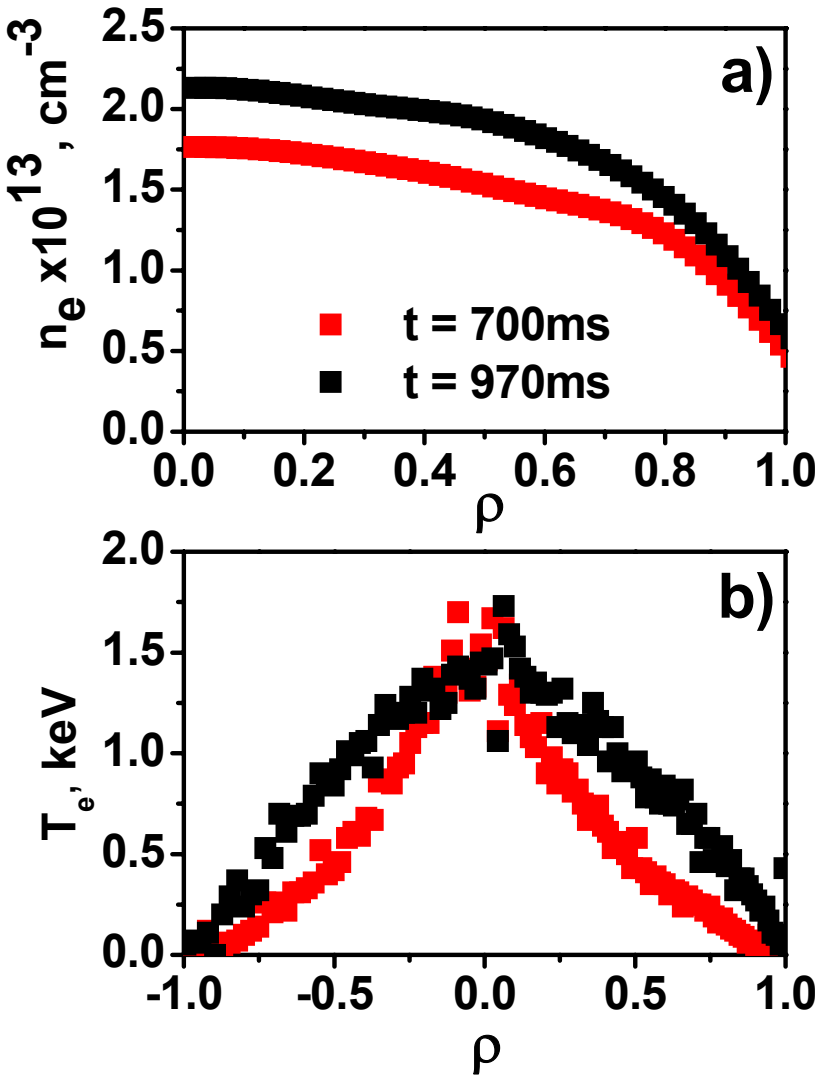

Fig.87 a) electron density profiles for time interval 1 (red dots) and time interval 2 (black dots) of Fig. 83; b) electron temperature profiles for time interval 1 (red dots) and time interval 2 (black dots) of Fig.83.

3.5.3 Comparison of ECH heating effect with NBI4+ICRF heating configuration

Comparison of the fast particle spectra during ECH and perpendicularly-injecting NBI4 was made to check the angular distribution in the same discharge with same plasma conditions and same plasma parameters. Time diagram of the plasma discharge is shown on Fig.88. The energy of particles injected bi NBI4 was 40 keV and the injected power was 5.7MW, the power of ICRF was 1.8MW.

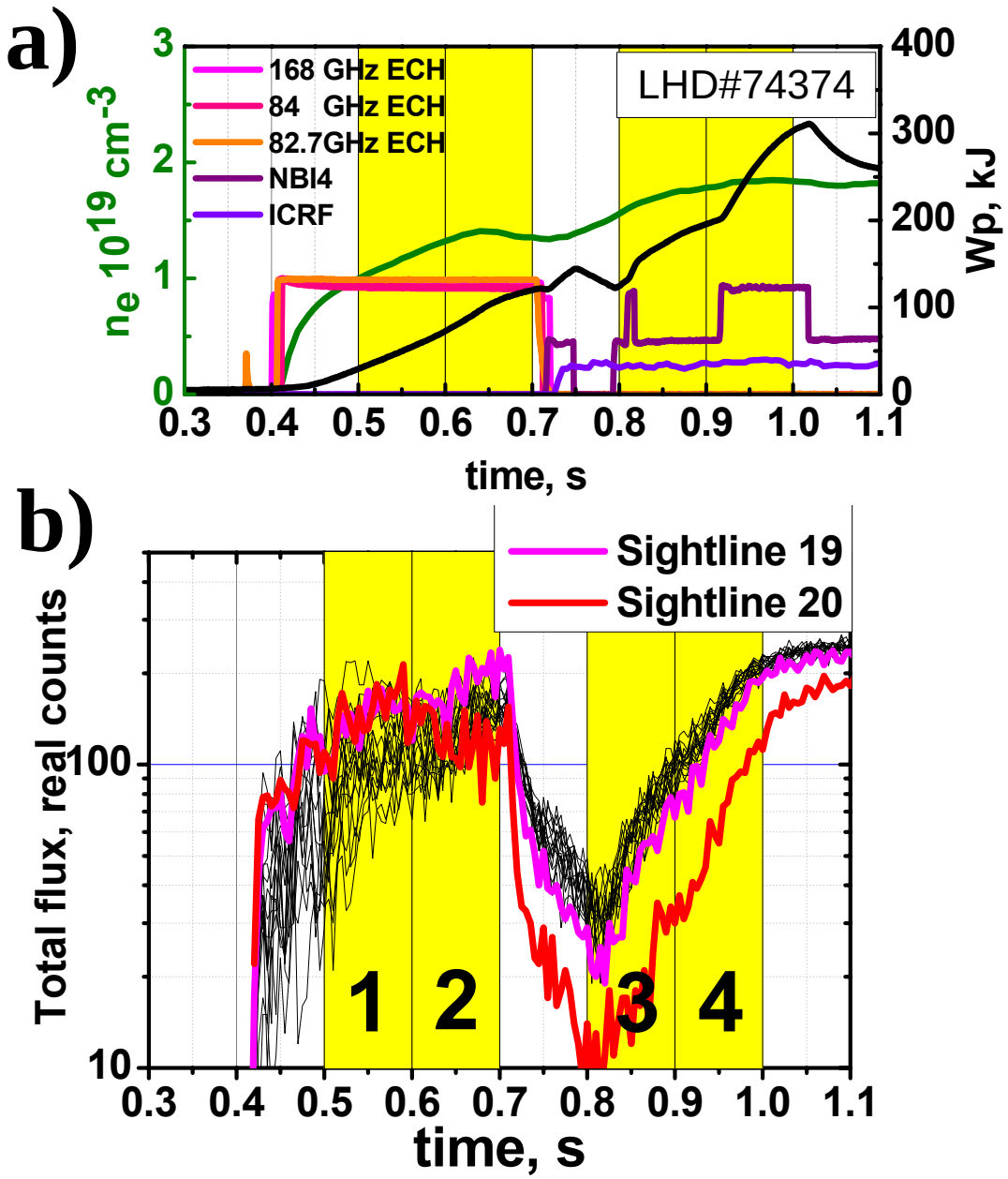

Fig.88 Time diagram of the LHD plasma discharge. (a) Purple - perpendicular NBI4 operation time; violet – ICRF operation time; orange, pink and magenta – ECH operation time; green curve - electron density *ne*; and black curve - stored energy *Wp*. (b) Charge exchange neutral particle flux during the discharge measured by 19 different detector segments (red curve – 20th sightline and magenta curve – 19th sightline).

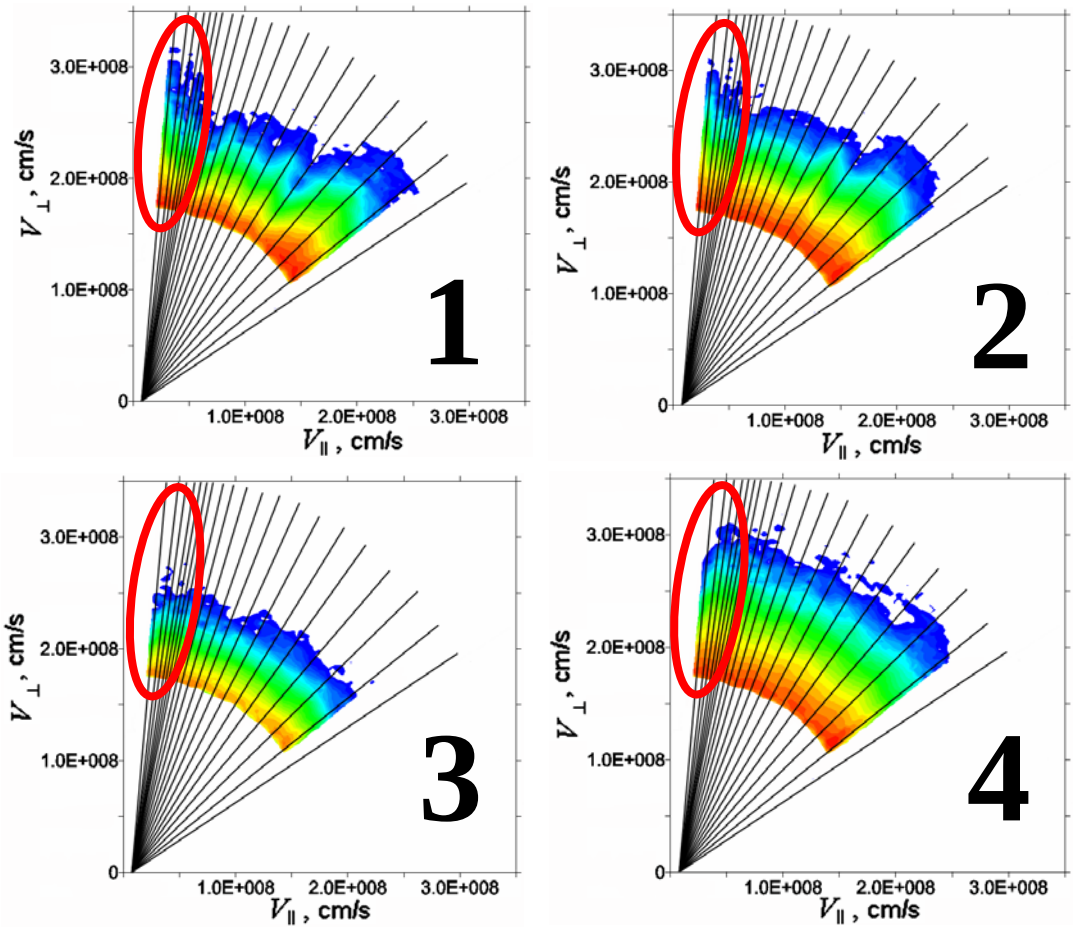

Fig.89 Restored angular-resolved spectra of fast particles for time interval 1, 2, 3 and 4 of the Fig.88 correspondingly.

It can be seen from Fig.88 b) that charge exchange neutral particle flux measured by 19th and 20th sightlines is significantly reduced after ECH switching off and during NBI4+ICRF operation. Restored angular-resolved spectra of fast particles for time interval 1, 2, 3 and 4 (Fig.89) demonstrate that during NBI4+ICRF operation the loss region appears (time interval 3 and 4). Quantitatively perpendicular region is shown on Fig.90, from which it can be seen that during NBI4 and ICRF operation (time interval 3 and 4) the flux of fast particles is increasing at all sightlines and the flux from sightline 19 and 20 always remains below the flux from the 18th sightline. During ECH operation the flux from sightline 19 and 20 is above the flux from the 18th sightline.

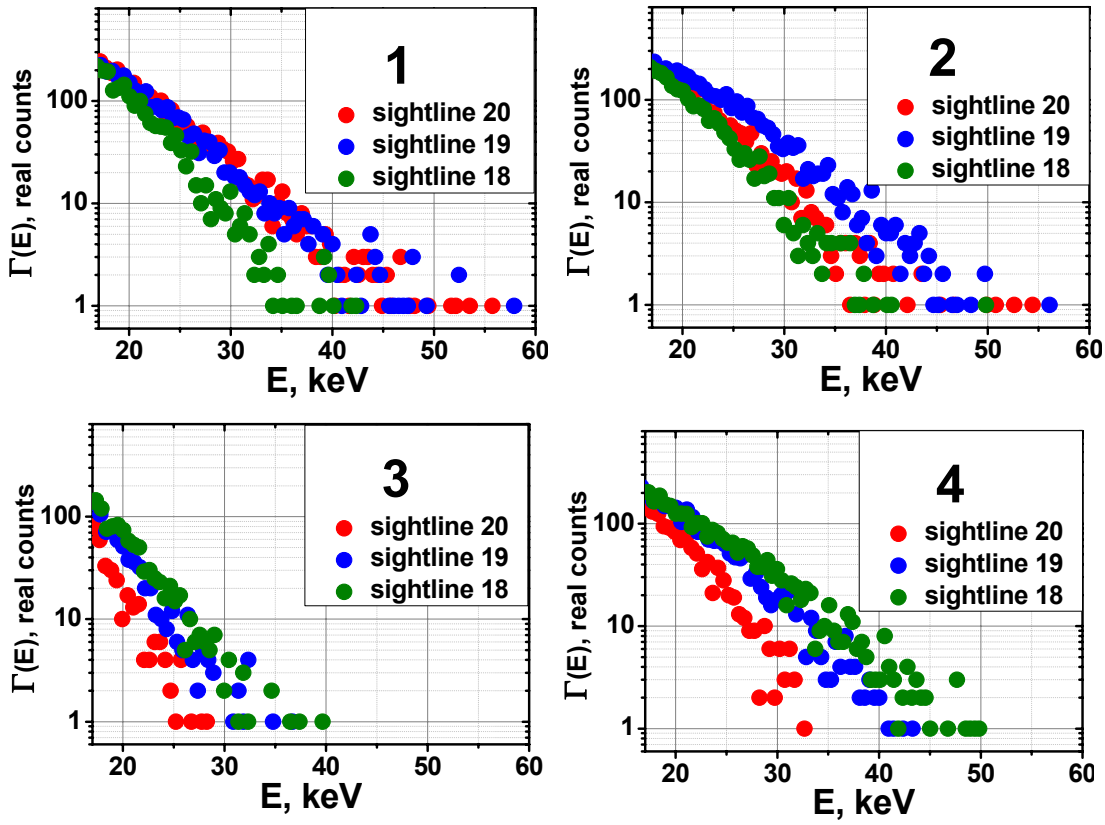

Fig.90 Flux spectra from sightline 20(red dots), 19(blue dots) and 18(green dots) for the case of ECH operation (time interval 1 and 2) and NBI4+ICRF operation (time interval 3 and 4)

Electron temperature profile comparison for all 4 intervals demonstrates (Fig.91) that during ECH operation electron temperature profile has peaked form on the contrast to the regimes with NBI4+ICRF heating. Such a shape electron temperature profile may case changes in electric field. Therefore loss-region in the direction close to perpendicular is very sensitive to the radial electric field.

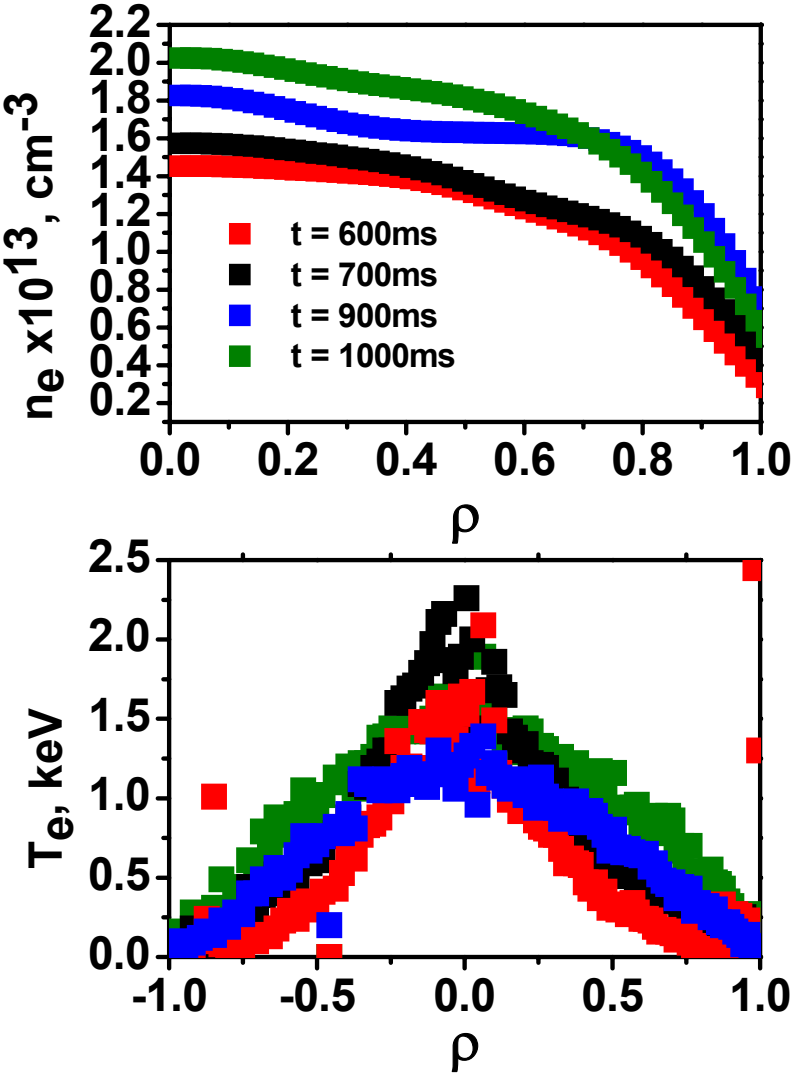

Fig.91 a) electron density profiles for time interval 1 (red dots), time interval 2 (black dots), time interval 3 (blue dots) and time interval 4 (green dots) of Fig. 88; b) electron temperature profiles for time interval 1 (red dots), time interval 2 (black dots), time interval 3 (blue dots) and time interval 4 (green dots) of Fig. 88.

3.5.3 Brief Summary

- Switching on of the ECH significantly influences on the angular distribution of fast particles.
- The change in electron temperature profile may change electric field and influence on the loss-cone region by.
- Peaked electron temperature profile is more favorable for loss-cone suppression.
- Strong positive electric field created by ECH can lead to the disappearance of the loss-cone near $\theta = 85^{\circ}$ pitch angle range.
- Thus ECH may become a powerful tool for suppression of the loss-cones and for improving fast particles confinement. Influence of the radial electric field should be checked. Influence of ECH heating power and heating type (on-axis, off-axis) together with plasma parameters on the loss-cones should be studied more detailed.

3.6 MAGNETIC AXIS SHIFT EFFECT

Comparisons of the fast particle population in plasmas shifted in and out in major radius are important in the suprathermal ion confinement studies. According to the results obtained from theoretical calculation inward shifted magnetic axis configuration lead to reducing of the deviation of fast particles from the magnetic surfaces as it is shown schematically on Fig.92 [33]. In the case of Rax = 3.6m calculations were made for the particle with the energy E = 3.4MeV from the point with radius-vector r_0 = 0.5a (where a is minor plasma radius) and poloidal angle θ_p=0.47π and the velocity direction θ_0= π/2 in poloidal direction and φ = 0 in toroidal direction.

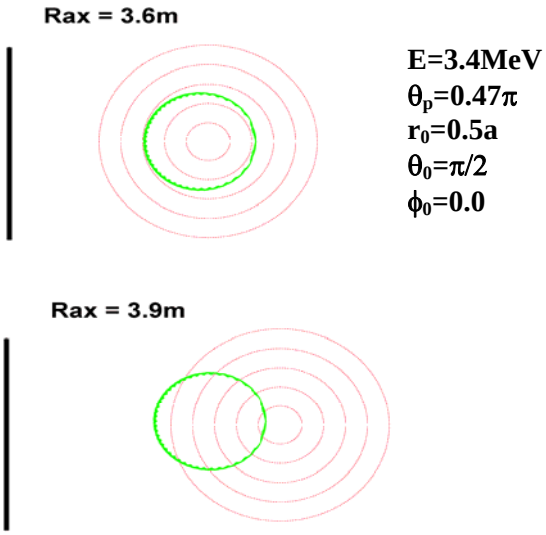

Fig.92 Qualitative illustration of fast particle orbits versus plasma region in two different magnetic axis positions.

Influence of magnetic axis shift on angular distribution of fast particles has been made for R_{axis} = 3.6m B_T = 2.75T and R_{axis} = 3.9m B_T = 2.539T. Measurements were carried out during perpendicular NBI4 operation.

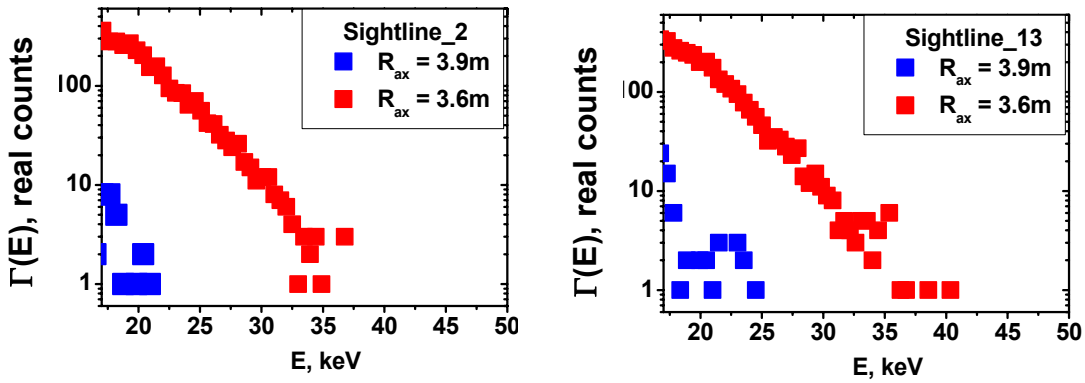

Fig.93 Fast particle spectra measured along SightlineNo.2 and .13 in two different magnetic field configurations R_{axis} = 3.6m B_T = 2.75T and R_{axis} = 3.9m B_T = 2.539T.

Plasma shifted inward in major radius has improved ion confinement with much higher fast particle population (Fig.93) and a uniform distribution in all sightlines (Fig.94) while plasma shifted out has poorer confinement and demonstrates strong angular anisotropy (Fig.95). One of the probable reasons to such anisotropy is the presence of loss-cones.

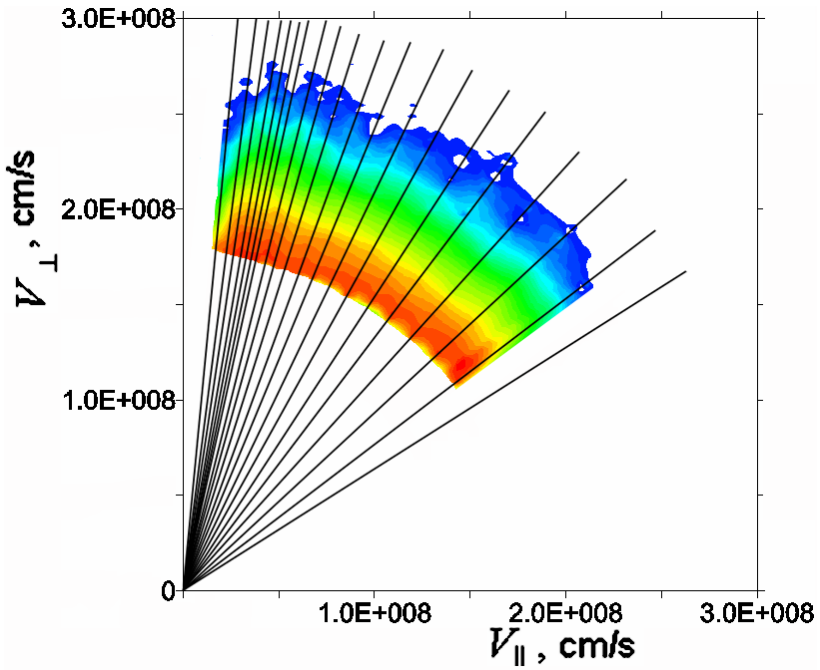

Fig.94 Angular distribution of fast particles for R_{axis} = 3.6m during NBI4 operation.

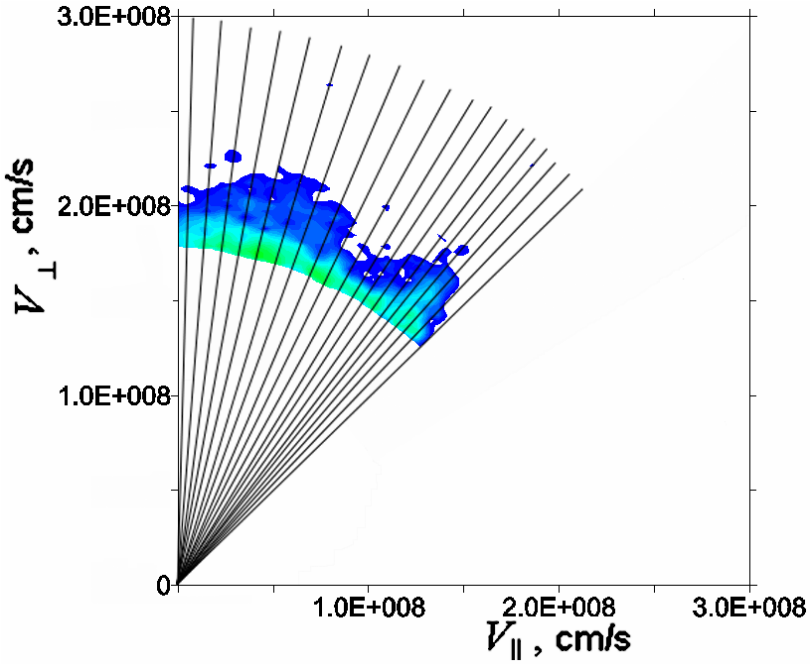

Fig.95 Angular distribution of fast particles for R_{axis} = 3.9m during NBI4 operation.

4. Data Analysis

4.1 NEUTRAL FLUX CALCULATION

4.1.1 ESCAPING ATOM FLUX FORMULATION (neutral source function, sightline integration kernel, paths and pitch angle dependence)

Since the naturally occurring charge exchange neutral particle source is not localized in contrast to the diagnostic neutral beam or pellet charge exchange methods, the correct interpretation of such measurements in a complex toroidal asymmetric geometry requires a careful numerical modeling of the neutral flux formation and the knowledge of the CX target distributions, relevant cross-sections and the magnetic surface structure [34].

A quantitative analysis of the escaping neutral flux from a flat plasma layer, assuming the ion distribution function f_i to be thermal, was offered in earlier studies *e.g.* [35]. Monograph [36] emphasizes the relationship between the central ion temperature in a flat layer and the inverse logarithmic slope of the high energy part of the observable neutral particle spectrum. However, a necessity exists [37, 38] for a more profound escaping neutral flux analysis in the recent experiments on magnetically confined complex 3D shaped plasmas with selective ion heating, *i.e.* orthogonal and tangential NBI and ICRF. A general formulation of neutral particle fluxes from non-axisymmetrical plasma was proposed in [39] for an arbitrary shape of isolines in the diagnostic cross-section. All the relevant plasma parameters were assumed to be functions of the magnetic surface, *i.e.* the flux coordinate $\rho(X) = (\Psi/\Psi_{LCMS})^{1/2}$ calculated along the diagnostic sightline using the MHD equilibrium data.

Thus, the kernel of the sightline integral is defined. The integral expresses the experimentally obtained energy resolved atomic flux via the required local fast atom birth rate in the plasma, which is proportional to the local ion distribution function. This paper addresses the computational modeling of the experimentally observed neutral particle energy spectrum shape, which is required to draw conclusions on physical mechanisms responsible for the ion distribution formation.

The atomic flux $\Gamma(E,\vartheta)$ [$\mathrm{erg^{-1}s^{-1}}$] measured by passive diagnostics of escaping high energy neutral particles is an integral along the sightline L of the local

differential fast atom birth rate in the plasma $g(E,\vartheta,X)$ [erg^{-1}cm^{-3}s^{-1}], which contains the sought ion distribution:

$$g(E,\vartheta,X)=\left(\sum_{(\alpha)} n^{(\alpha)}(X)\left\langle\sigma \mathrm{v}\right\rangle_{cx}^{(\alpha)}\right) n_i(X) f_i(E,\vartheta,X)\,, \tag{1}$$

$$\Gamma(E,\vartheta)=\frac{\Omega S_a}{4\pi}\int_{(\square)} g(E,\vartheta,X) e^{-\int_0^X \frac{dX'}{\lambda_{mfp}(E,X')}} dX\,, \tag{2}$$

where α denotes the summation over charge exchange rates on different targets, $n^{(\alpha)}$ and $\left\langle\sigma \mathrm{v}\right\rangle_{cx}^{(\alpha)}$ are target densities and CX reactivities, $n_i f_i$ is the ion distribution function. The integration variable X is the distance along the diagnostic viewing direction, Ω is the observable solid angle and S_a is the diagnostic aperture area. The exponential factor describes the attenuation of the atomic flux in the plasma. $\lambda_{mfp}^{-1}(E,X')$ is the mean number of ionizations per unit path length. Changing the integration variable in (2) from X to the effective minor radius ρ yields [38, 39]

$$\Gamma(E,\vartheta)=e^{\int_{\rho_{\min}}^{1}\frac{Q^-(\rho')d\rho'}{\lambda_{mfp}(E,\rho')}}\frac{\Omega S_a}{4\pi}\int_{\rho_{\min}}^{1} g\left(E,\vartheta,\rho\right)\times$$

$$\times\left[Q^+(\rho)e^{-\int_{\rho_{\min}}^{\rho}\frac{Q^+(\rho')d\rho'}{\lambda_{mfp}(E,\rho')}}-Q^-(\rho)e^{-\int_{\rho_{\min}}^{\rho}\frac{Q^-(\rho')d\rho'}{\lambda_{mfp}(E,\rho')}}\right]d\rho\,, \tag{3}$$

where $Q^+(\rho)=dX/d\rho>0$ and $Q^-(\rho)=dX/d\rho<0$ on the two intervals between $\rho=1$ and $\rho=\rho_{\min}$.

In a symmetrical case when $Q^+(\rho)=-Q^-(\rho)$ this formula reduces to a generalized form of the so-called Freeman-Katz integral equation [40]. Analytic expressions for the kernel $Q^{+/-}(\rho)$ were found [41] in some particular cases of ρ isoline shape. The general approach implies that the functions $Q^{+/-}(\rho)$ are obtained from the actual structure of the isolines $\rho=const$ in the diagnostic cross-section plane known from VMEC numerical solution of 3D MHD equilibrium equations assuming nested flux surfaces [27]. This enables one to use the relation (3) for computer simulations of the neutral particle diagnostic data. Fig.96 illustrates the sample calculation of the positive Q^+ and negative Q^- branches of the integral transform (3) for one of the silicon detector based neutral particle analyzer (SDNPA) diagnostic sightlines [3].

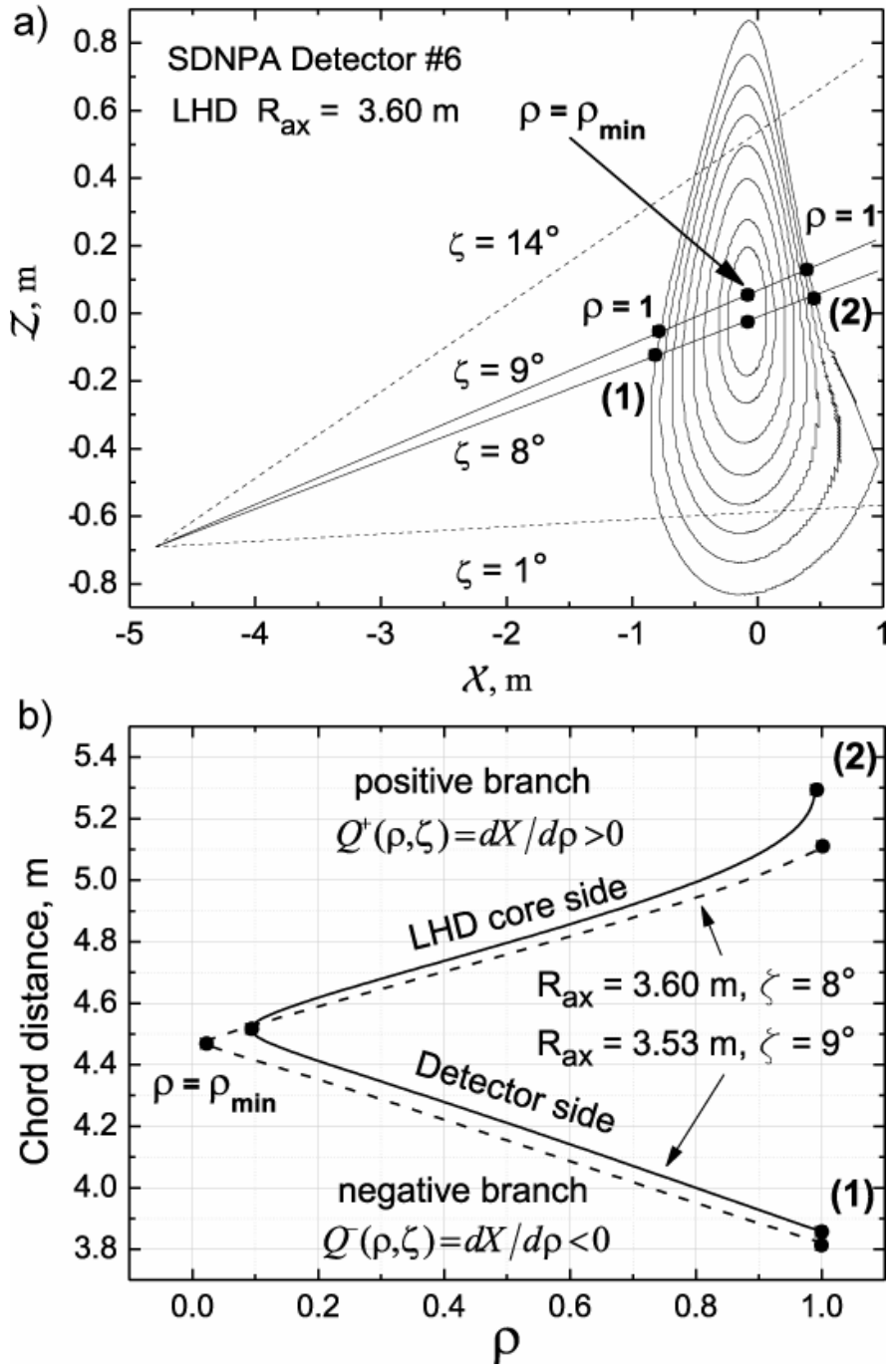

Fig.96 a). Contour lines determined by LHD magnetic surface structure in SDNPA [2] detector #6 diagnostic cross-section; ζ designates the vertical scan angle. b). Integral transform (3) kernel calculation example for SDNPA detector#6 at two vertical scan positions: R_{ax} = 3.53 m, ζ = 9° and R_{ax} = 3.60 m, ζ= 8°.

4.1.2. COMPUTATIONAL MODELING OF ENERGY DISTRIBUTIONS

The experimentally measurable $\Gamma(E,\vartheta)$ has been calculated for hydrogen plasma on the following radial profile shape assumptions:

$$n_e(\rho)=n_e(0)\left(1-\rho^q\right)^s, \qquad n_0(\rho)=n_0(0)\exp\left(B\rho^A\right),$$
$$T_i(\rho)=T_i(0)\left(1-\rho^x\right)^y, \qquad T_e(\rho)=T_e(0)\left(1-\rho^u\right)^w \tag{4}$$

with the unknown values taken as free parameters. The hydrogen charge exchange $H^+ + H^0 \rightarrow H^0 + H^+$ and hydrogen ionization by proton impact $H^+ + H^0 \rightarrow H^+ + H^+ + e^-$ cross-section data were taken from [42].

Computational results for the isotropic Maxwellian plasma ion energy probability density function

$$f_i^{(M)}(E,\rho)=\frac{2\sqrt{E}}{\pi^{1/2}T_i^{3/2}(\rho)}\exp\left(-E/T_i(\rho)\right) \tag{5}$$

are shown in Fig.97 for SDNPA detector #6 chord at the middle vertical scan position and LHD magnetic axis at R_{ax} = 3.60 m.

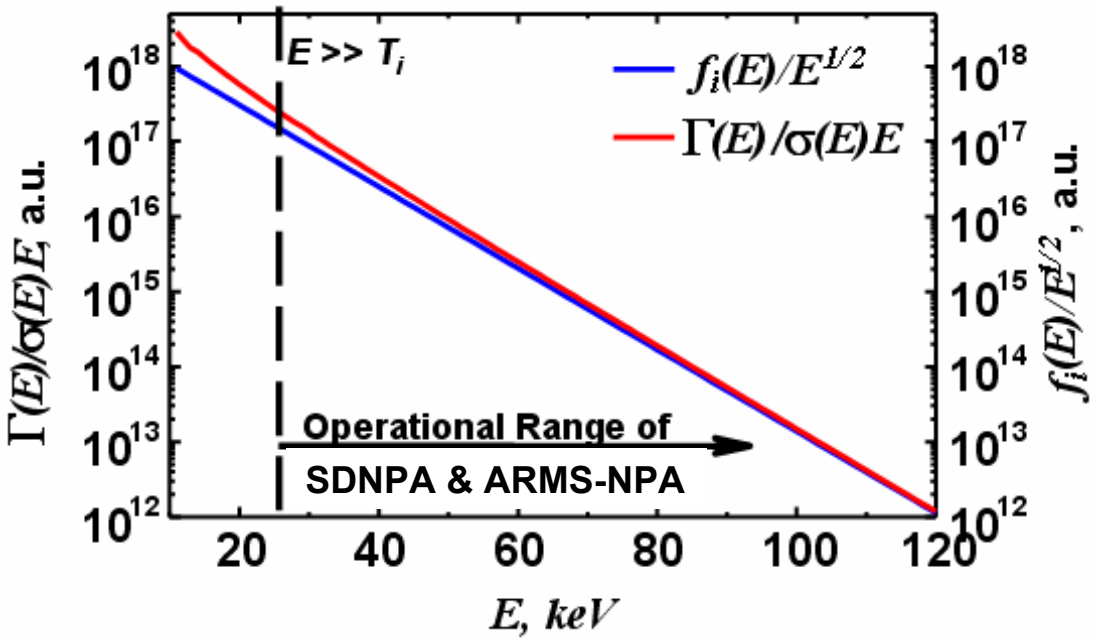

Fig.97 Red curve (left scale) - calculation of the experimentally measurable CX neutral particle spectrum corrected for σE factor; blue curve (right scale) - thermal *exp(-E/T_i(0))* representing the core ion temperature.

The resultant typical neutral hydrogen energy spectrum corrected for the charge exchange reactivity factor $\sigma\sqrt{E}$ combined with the Jacobian $\sqrt{E}$ (solid curve) and the Maxwellian exponent $\exp\left(-E/T_i(0)\right)$ in the core region (dotted curve) are scaled to match at the highest energy in the considered range. The calculation example shown in the plot corresponds to $T_i(0)$ = 10 keV. Taking the inverse logarithmic slope of $\Gamma(E)/\sigma(E)E$ in the energy range below $\approx 5T_i(0)$ as an estimation of the core T_i results in a systematic 10-30% underestimation while at the higher energies this error vanishes. This is consistent with the simplified analysis for a flat plasma layer case [36]. However, in practice either the counting statistics is poor at the highest energies or the high-energy tail becomes substantially non-Maxwellian due to the strong distortion by the NBI heating. For the ICRF accelerated particles at energies much greater than the majority ion temperature the steady state transversal energy distribution exhibits a quasi-Maxwellian asymptotic behavior according to Stix theory [43]. Therefore, this numerical modeling is also relevant to perpendicularly observed fast particle spectra from ICRF heated plasma.

In order to calculate the tangentially measured neutral hydrogen spectrum from tangential NBI heated Maxwellian background plasma a simplified model ion distribution function was taken in the form of the classical fast ion slowing down distribution from a monoenergetic isotropic source [43, 44]

$$S\left(v-v_0\right)=\frac{S_0}{4\pi v^2}\delta\left(v-v_0\right),$$

$$f_i^{(s)}\left(v\right)=\frac{S_0}{4\pi}\frac{\tau_s}{v^3+v_c^3}, \quad \text{for} \quad v<v_0, \tag{6}$$

where S_0 is the source rate, v_0 is the injection velocity, τ_s and v_c are the Spitzer's slowing down time and the critical velocity given by

$$\tau_s=\frac{3m_pT_e^{3/2}}{4\sqrt{2\pi}n_e e^4\Lambda m_e^{1/2}}, \qquad v_c^3=\frac{3\sqrt{2\pi}T_e^{3/2}}{2m_pm_e^{1/2}}, \tag{7}$$

and Λ is the Coulomb logarithm.

The lower curve in Fig.98(a) illustrates the $f_i^{(s)}$ behavior and the two upper curves show the resultant H^0 energy spectra calculated as (3) with the integral kernels corresponding to the SDNPA diagnostic detector #6 sightline at ζ = 9° vertical scan position for LHD R_{ax} = 3.53 m and at ζ = 8° vertical scan position for LHD R_{ax} = 3.60 m. Fig.98 (b) shows the experimental spectra measured along these sightlines from 147 keV H^0 NBI heated n_e=0.5x10^{13} cm^{-3} background plasmas.

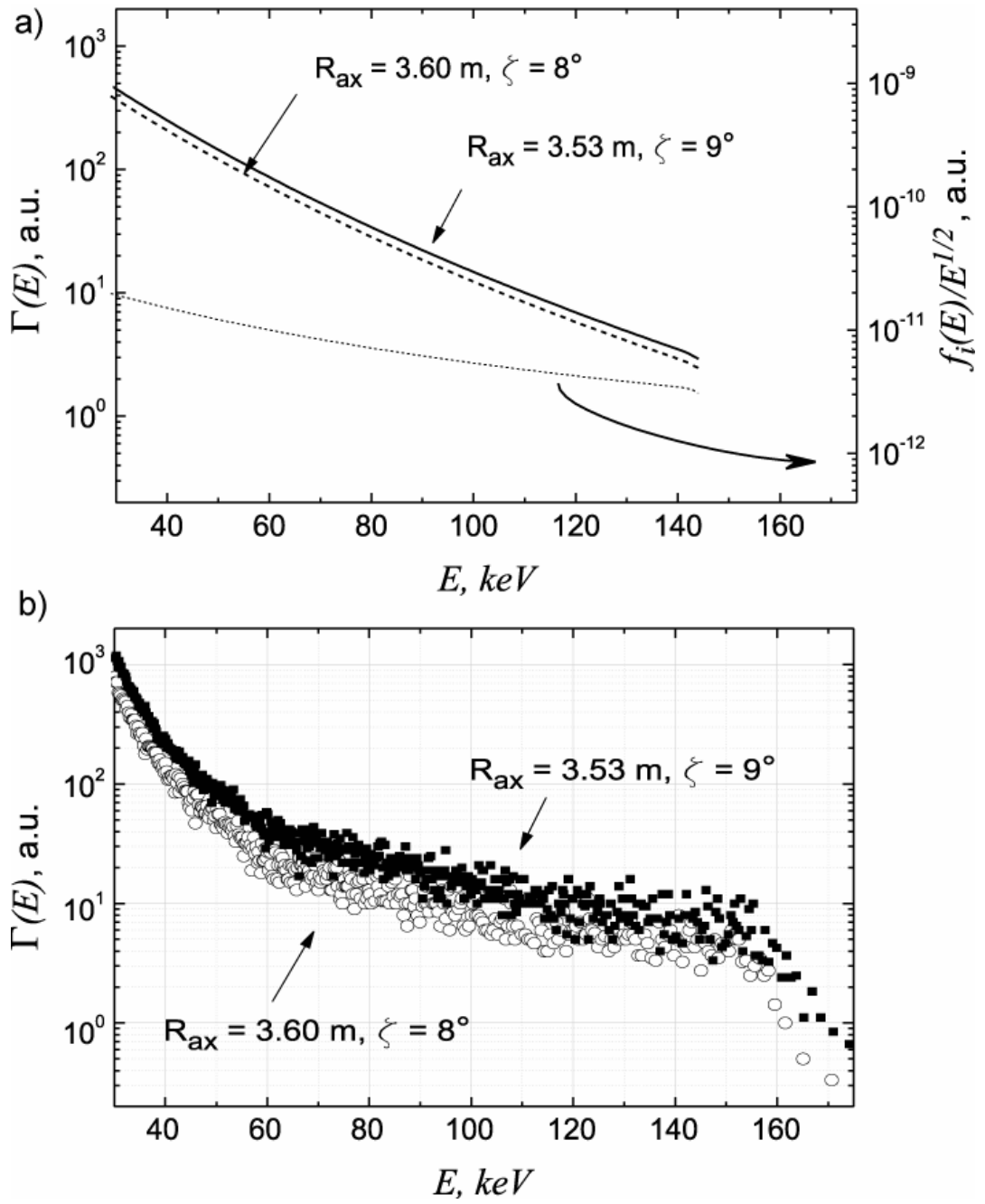

Fig.98 a). Calculation of tangential NBI-induced energetic particle distributions for two variants of SDNPA detector #6 measurement geometry ($n_e(0)$ = 0.5x10^{13} cm^{-3}, q = 6, s = 2; $n_0(0)$ = 3x10^6 cm^{-3}, A = 6, B = 9; $T_e(0)$ = 2 keV, u = 4, w = 2).

b). Experimental fast neutral spectra form 147 keV H^0 tangential NBI heated n_e=0.5x10^{13} cm^{-3} target plasma by SDNPA detector#6 at ζ = 9° for R_{ax} = 3.53 m and at ζ = 8° for R_{ax} = 3.60 m.

As it can be seen from Fig.98 (a) the calculated flux for the case of Rax = 3.53 m magnetic axis position is slightly higher than that one in Rax = 3.6 m configuration due to geometry effect. According to experimental results Fig.98 (b) difference between these two configurations is stronger than in calculations. That means that inward shift is more favorable for fast particle confinement.

According to Fig.98 (a) the chord superposition effect on the relative values of distribution curves obtained in different geometry should be accounted for in data interpretation. The difference between two calculated curves (for Rax = 3.53m and Rax = 3.6m) is slight due to not significant difference between compared magnetic axis positions.

Thus in terms of proceeding studying of magnetic axis shift effect on fast particle confinement and angular distribution calculations were made for significantly different magnetic axis configurations Rax = 3.6 m and Rax = 3.9 m. Calculations were made for isotropic Maxwellian fast particle distribution function with the next parameters:

$$n_e = (n_e(0) - n_{e\_edge})(1 - \rho^{\beta_0})^{\beta} + n_{e\_edge}$$
$$T_e = (T_e(0) - T_{e\_edge})(1 - \rho^{\alpha_0})^{\alpha} + T_{e\_edge} \qquad (8)$$

$n_e(0)$ = 2x10^{13} cm^{-3}, n_{e_edge} = 0.4 x10^{13} cm^{-3}, β_0 = 1.7, β = 1; $n_0(0)$ = 5x10^{7} cm^{-3}, *calculated by Aurora code* (Fig.99); $T_e(0)$ = 1 keV, T_{e_edge} = 0.1 keV, α_0 = 3, α_0 = 2.

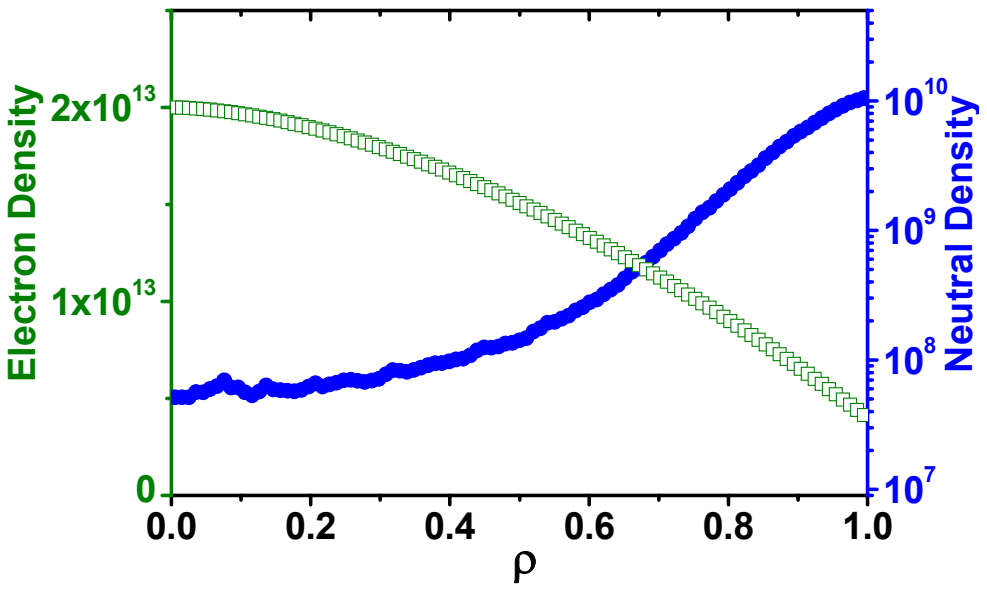

Fig.99 Assumed electron density n_e (green color) and neutral density n_0 (blue color) profiles.

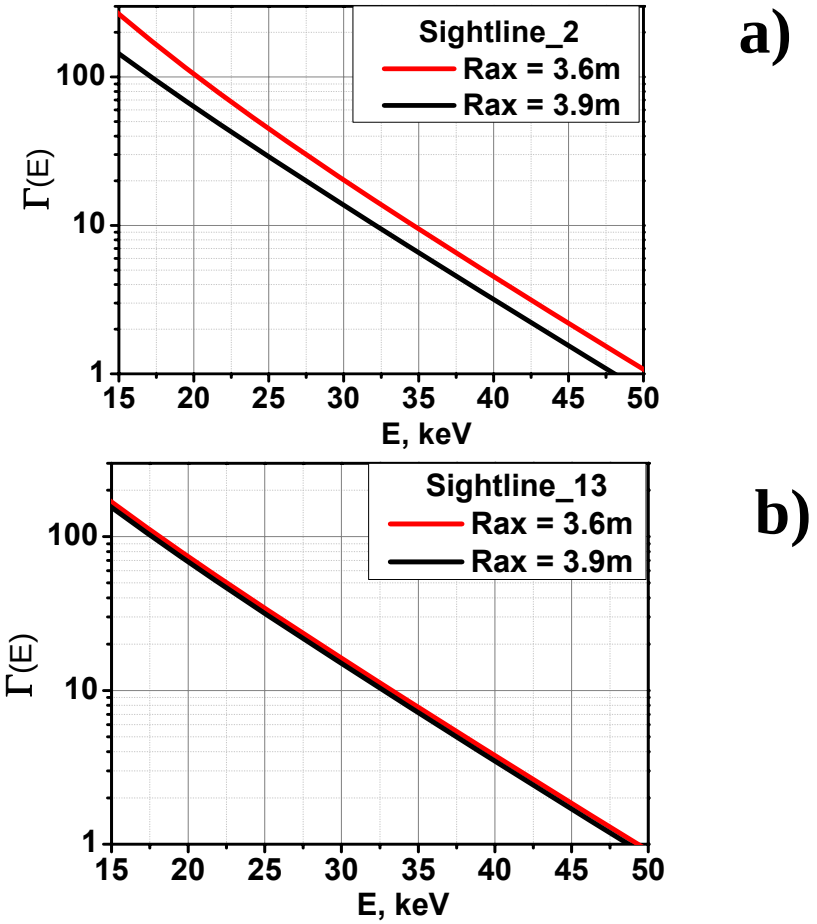

Fig.100 Energy spectra of H^0 calculated for two different sightlines of ARMS-NPA diagnostic (a) SightlineN0.2 and (b) SightlineNo.13 for Rax = 3.6 m and R_{ax} = 3.9 m magnetic axis positions.

Two different sightlines of ARMS-NPA diagnostic (Sightline No2 at Fig.100(a) and Sightline No 13 at Fig.100(b)) were chosen to demonstrate the influence of the geometry of measurements on the measured flux. According to calculation results quantitative difference between fluxes measured by sightline No2 is large then that one of Sightline No13 (Fig.100). This correlates with experimentally measured data (Fig.93).

Angular resolved spectra of fast particles were simulated for Rax = 3.6 m and R_{ax} = 3.9 m magnetic axis position configuration in order to check the influence of the geometry of measurements on the angular dependence of the fast particle flux emitted from plasma (Fig.101 and Fig.102 correspondingly). Both cases demonstrate angular anisotropy due to the geometry of measurements influence.

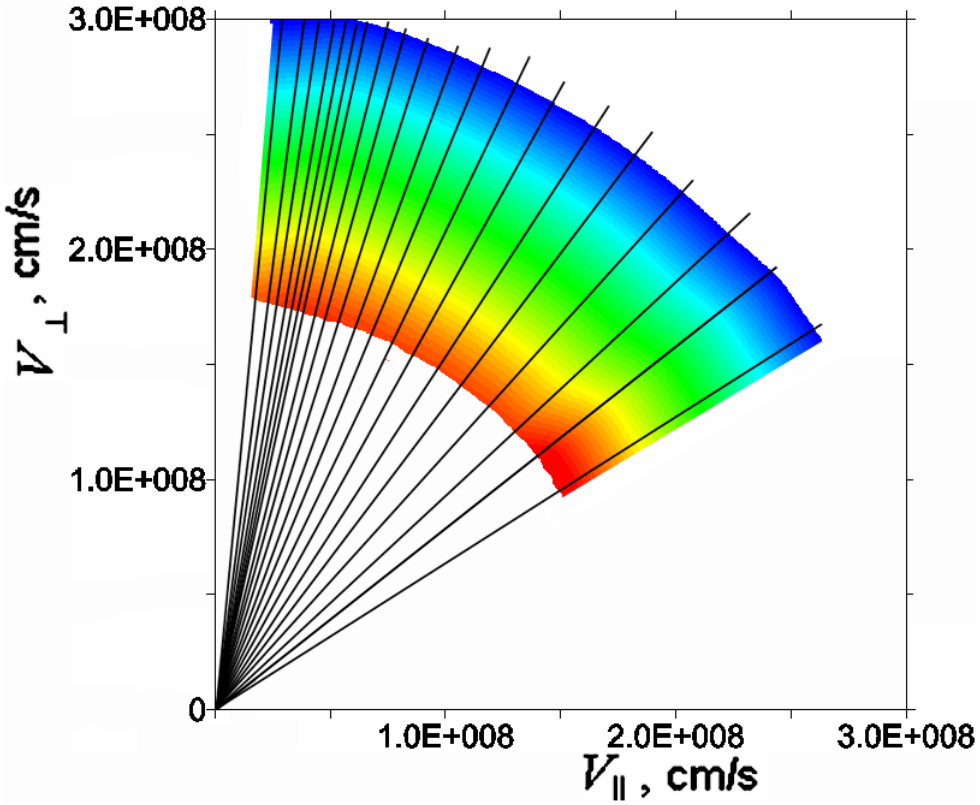

Fig.101 Calculated angular resolved spectra of fast particles were for Rax = 3.6 m magnetic axis position.

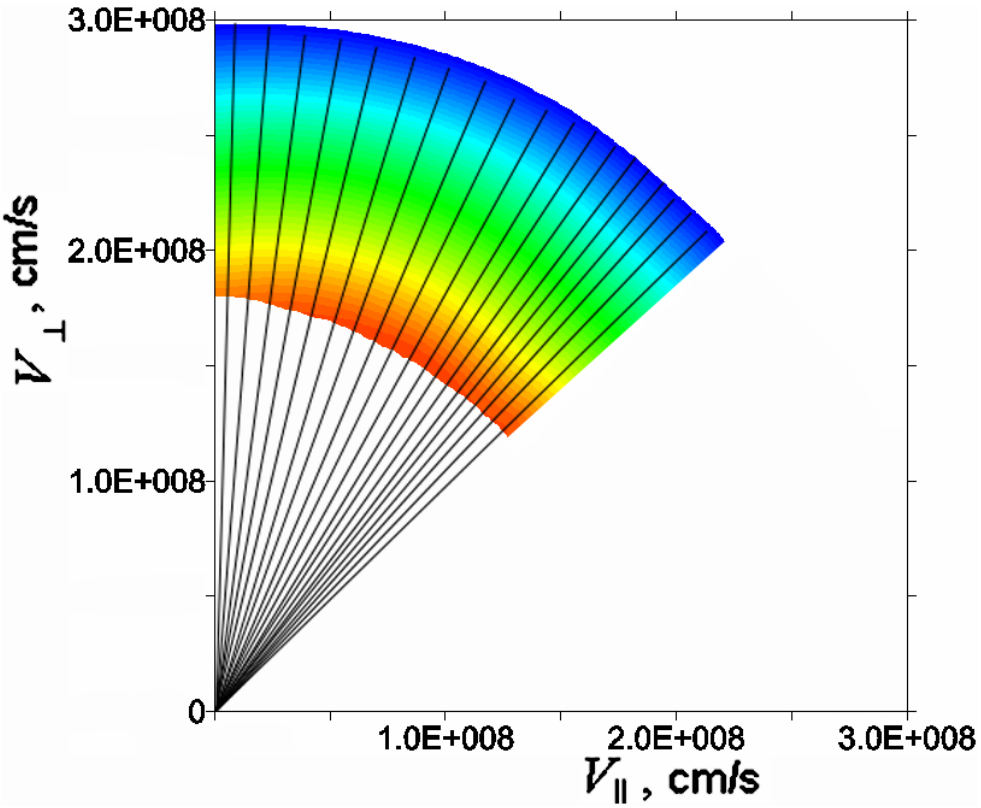

Fig.102 Calculated angular resolved spectra of fast particles were for Rax = 3.9 m magnetic axis position.

Thus for the better understanding of angular distribution of fast particles the geometrical effect should be subtracted from experimental data. As it can be seen from Fig.100 fast particle spectra differ from each other only by relative value, thus for the geometry effect subtraction it will be enough to divide experimental spectra along every sightline by relative values obtained from calculation results with taking into account the geometry effect.

Angular resolved spectra plotted on Fig.103 and Fig.104 represent experimental data of angular distribution of fast particles after the geometry effect subtracting for Rax = 3.6 m and R_{ax} = 3.9 m correspondingly. Both cases still demonstrate angular anisotropy. Fast particle population in Rax = 3.6m configuration measured along four perpendicular sightlines are plotted on Fig.105 and demonstrate reducing of spectra towards the 20th sightline. The case of R_{ax} = 3.9 m in addition to the reducing of the fast particle flux in perpendicular direction (Fig.106) still demonstrates the drop of fast particle population in the region of the 8th channel (Fig.104).

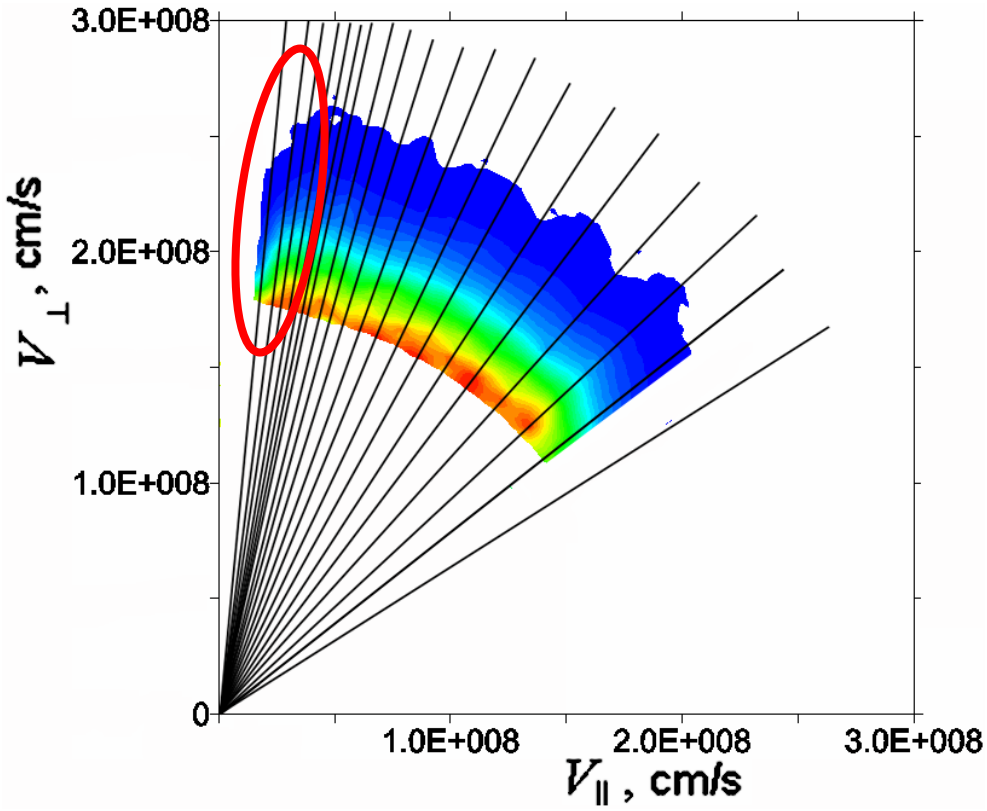

Fig.103 Experimental data of angular distribution of fast particles after the geometry effect subtracting for Rax = 3.6 m B_T = 2.75T.

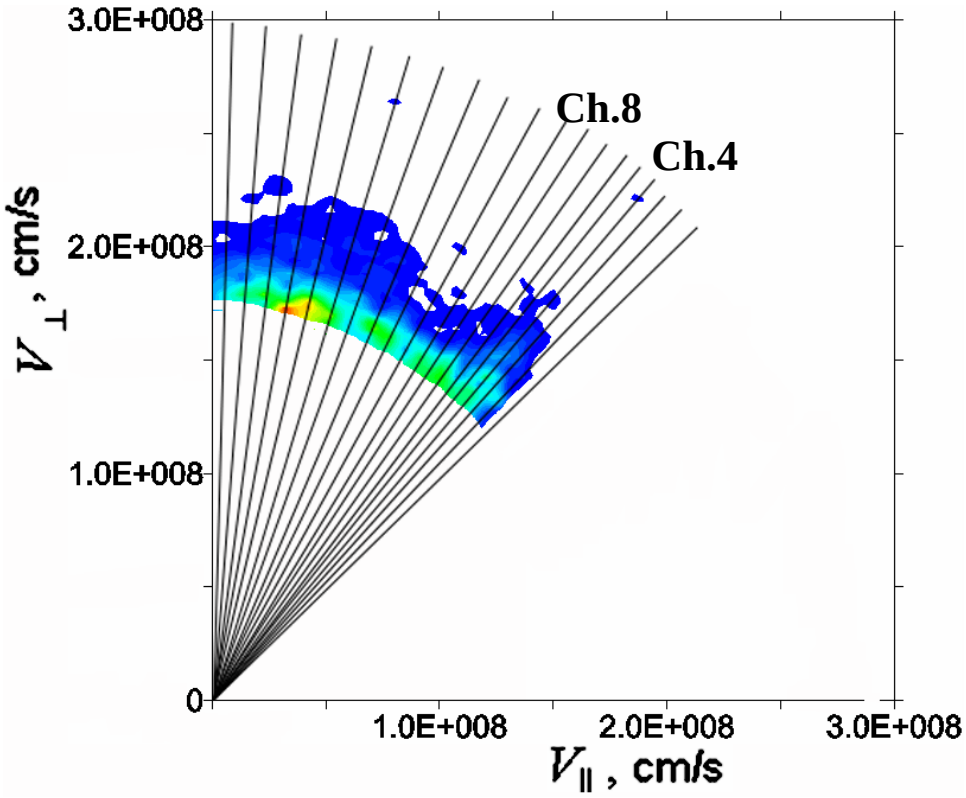

Fig.104 Experimental data of angular distribution of fast particles after the geometry effect subtracting for R_{axis} = 3.9m B_T = 2.539T.

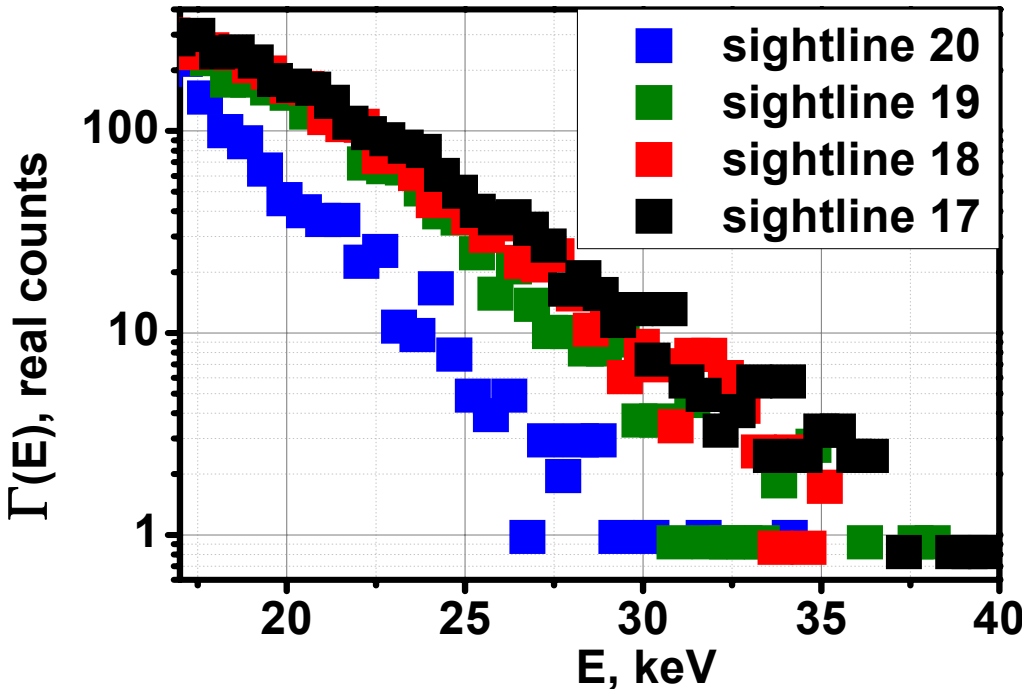

Fig.105 Fast particle spectra for four of the sightlines close to perpendicular direction (sightline 20 is the most perpendicular one) during perpendicularly-injecting NBI4 operation the case of Rax = 3.6 m B_T = 2.75T magnetic field after the geometry effect subtracting.

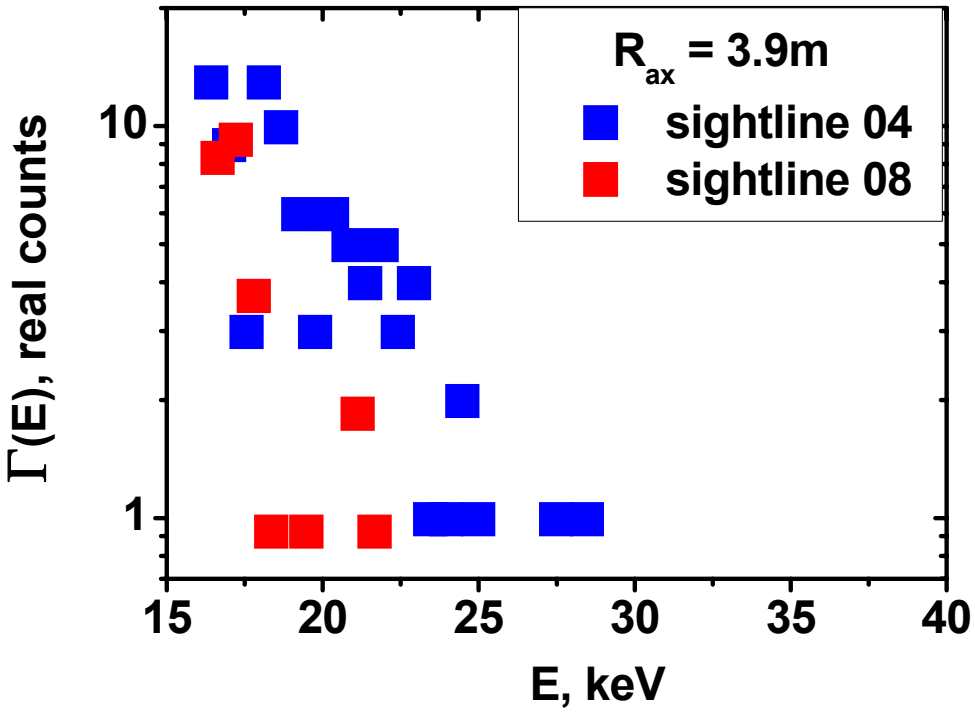

Fig.106 Fast particle spectra for SightlineNo 4 and SightlineNo 8 during perpendicularly-injecting NBI4 operation the case of Rax = 3.9 m B_T = 2.539T magnetic field after the geometry effect subtracting.

4.1.3 Brief Summary

- The chord superposition effect on the relative values of distribution curves obtained in different geometry should be accounted for in data interpretation.
- Magnetic axis shift effect in experiment is slightly larger for Rax = 3.5m magnetic axis configuration rather Rax = 3.6m configuration than in calculations results, therefore inward shift is favorable for fast particle confinement.
- After subtracting of the geometry effect from experimental data the drop of fast particle population at perpendicular sightlines still remains.

4.2 FAST PARTICLE SPECTRA DEPENDANCE ON PLASMA PARAMETERS

4.2.1 Influence of electron and neutral density on the fast particle spectra.

In order to check the influence of plasma parameters on the obtained fast particle flux calculations were made for four cases of central electron density $n_{e1}(0)$ = $1x10^{13}$ cm^{-3}, $n_{e2}(0)$) = $2x10^{13}$ cm^{-3}, $n_{e3}(0)$) = $3x10^{13}$ cm^{-3}, $n_{e4}(0)$) = $4x10^{13}$ cm^{-3}. The electron temperature for all the cases was fixed $T_e(0)$ = 1.5 keV. Formula for electron density and temperature profiles are:

$$n_e = (n_e(0) - n_{e\_edge})(1 - \rho^{\beta_0})^{\beta} + n_{e\_edge}$$
$$T_e = (T_e(0) - T_{e\_edge})(1 - \rho^{\alpha_0})^{\alpha} + T_{e\_edge} \quad (8)$$

where n_{e_edge} = 0.4 $x10^{13}$ cm^{-3}, β_0 = 1.7, β = 1; T_{e_edge} = 0.1 keV, α_0 = 3, α_0 = 2. Neutral density profiles were calculated by Aurora code and shown on Fig.107 together with electron density profiles.

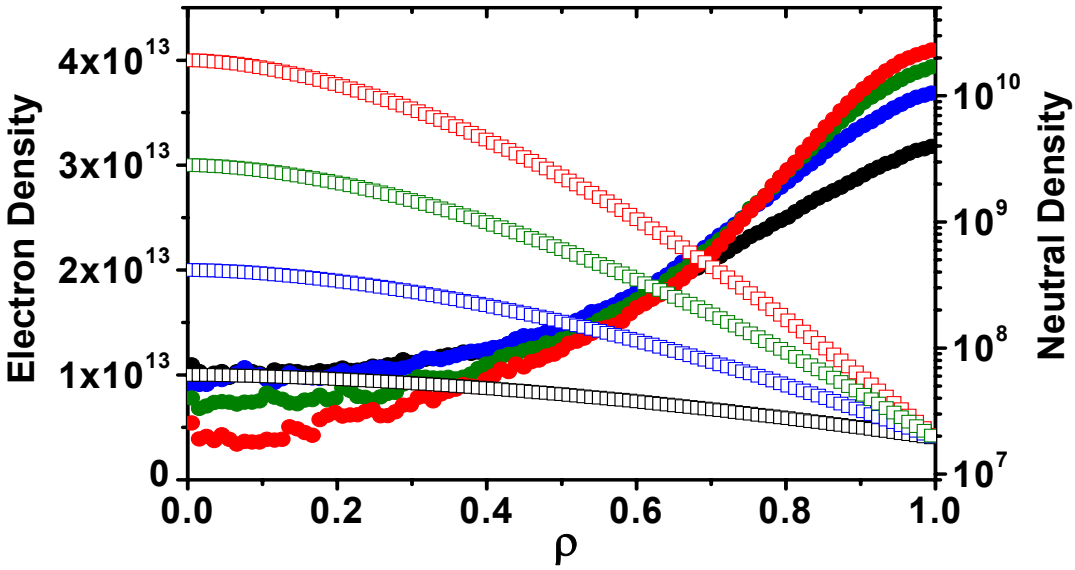

Fig.107 Electron density profiles (empty dots) and corresponding to them calculated by Aurora code neutral density profiles (painted over dots).

Calculations were made for the Maxwellian plasma. The calculated flux for all four cases is shown at Fig.108 and it can be seen that electron and neutral density profiles don't influence significantly on the shape and the slope of the spectra but only on it's the relative values.

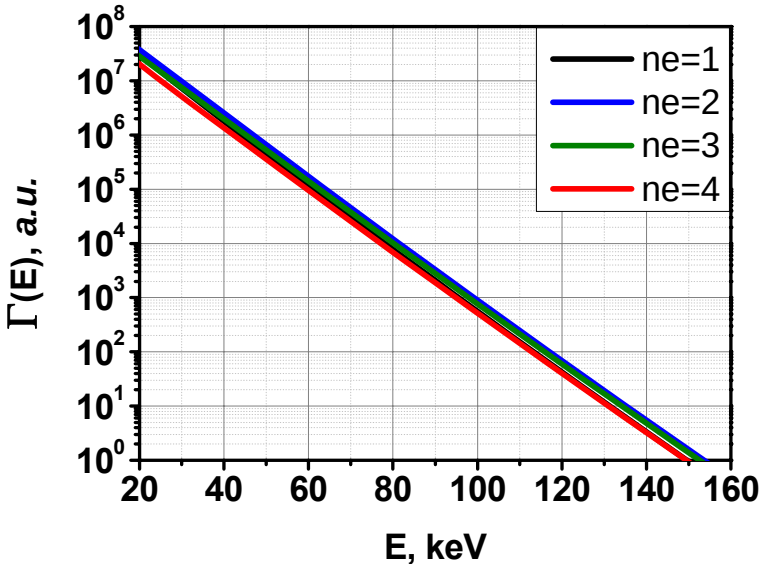

Fig.108 Calculated fast particle flux for four cases of central electron density $n_{e1}(0)$ = $1x10^{13}$ cm^{-3}(black curve), $n_{e2}(0)$) = $2x10^{13}$ cm^{-3}(blue curve), $n_{e3}(0)$) = $3x10^{13}cm^{-3}$ (green curve), $n_{e4}(0)$) = $4x10^{13}$ cm^{-3}(redcurve).

Calculation results were compared with experimental ones measured during joint operation of ICRF and perpendicularly injecting NBI4 in plasma with Rax = 3.6m B=2.85T magnetic axis position. Experimental electron density and temperature profiles for five discharges with different densities are shown on Fig.109

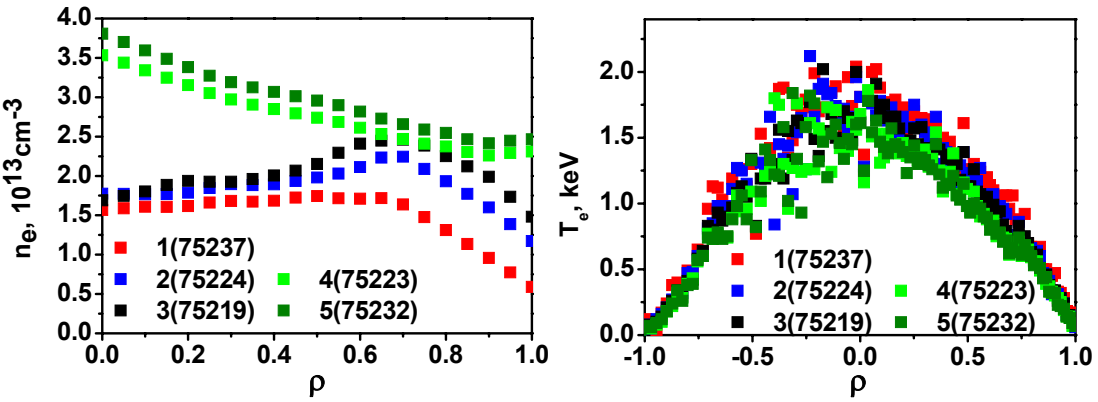

Fig.109 Experimental electron density and temperature profiles.

Restored angular dependent spectra for the discharges 75237, 75224 and 75219 are shown on Fig.110 together with quantitative spectra along sightlines close to perpendicular directions. In all three shots the region of significant reducing of fast particle population still exists for 20th and 19th sightlines. As it can be seen from the quantitative figures for the case of lower electron density with flat profile (ShotNo 75237) the flux of fast particles emitted from plasma is higher. With increasing of the electron density and taking a hollow shape the flux of fast particles is reducing probably due to reducing of the neutral density in the region of increased electron density. In addition to that spectrum from the sightline 17 coincides with 18th one of the ShotNo 75237. Thus the shape of loss-region may by smaller for the case of smaller electron density.

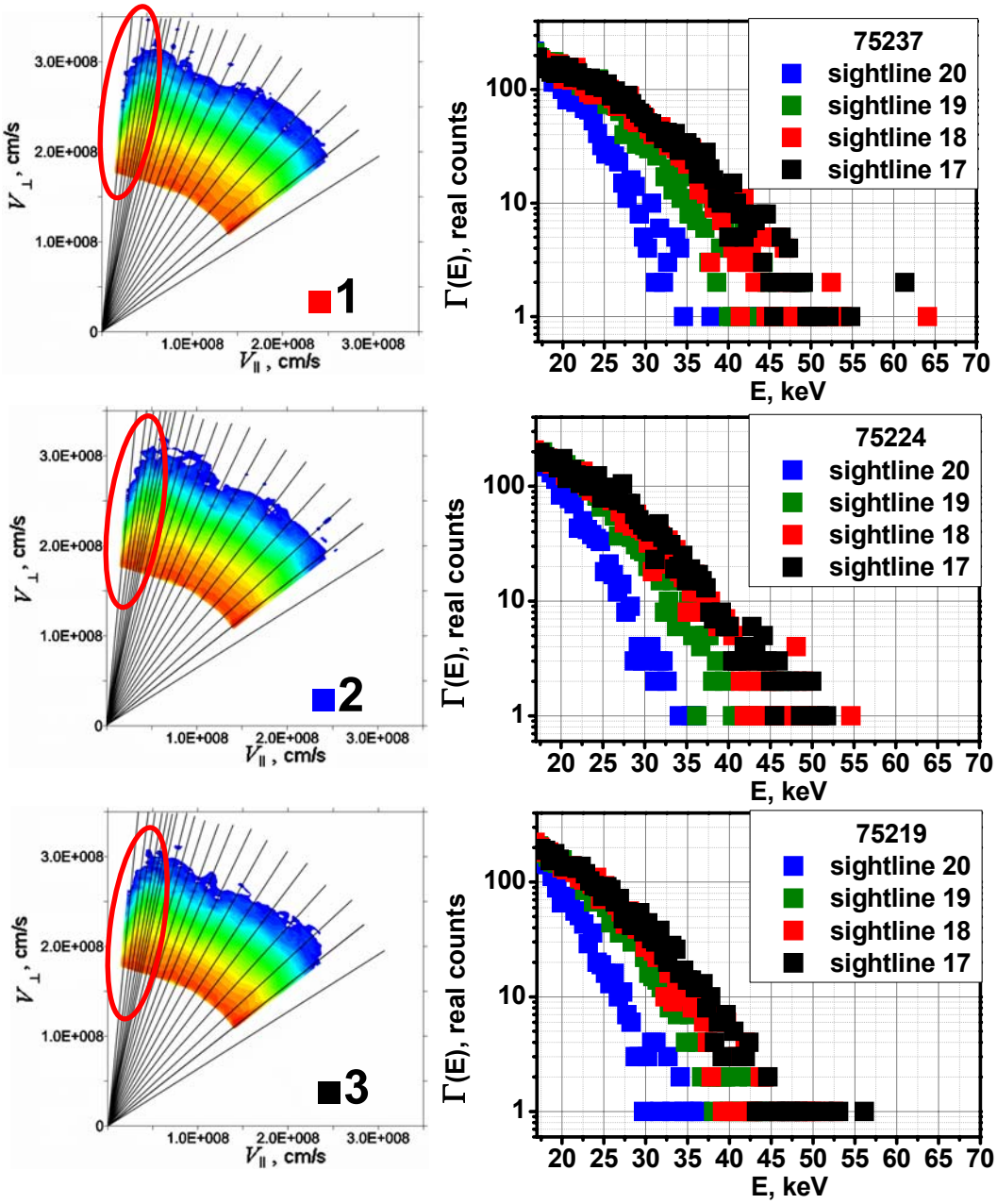

Fig.110 Restored angular dependent spectra for the discharges 75237, 75224 and 75219.

For the case of significantly higher electron density, *i.e.* for discharge 75223 and 75232, the restored angular dependent spectra are shown on Fig.111 together with quantitative spectra along sightlines close to perpendicular directions.

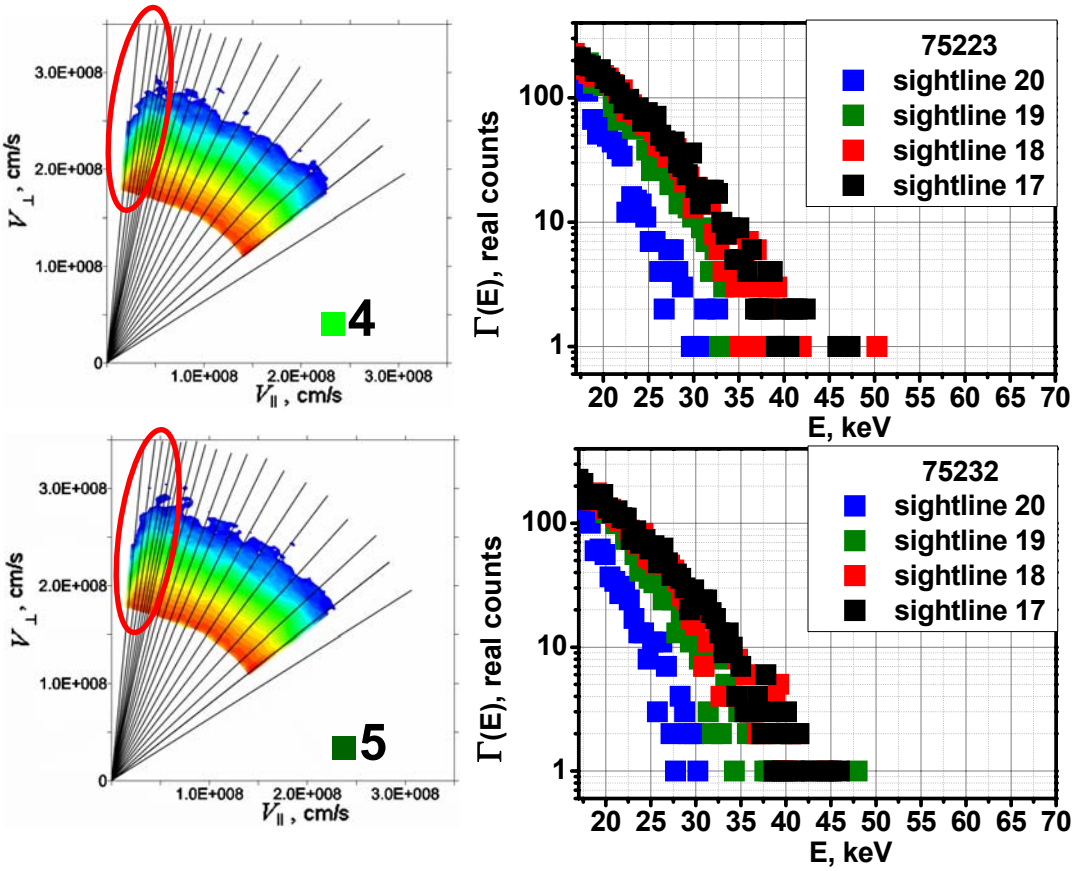

Fig.111 Restored angular dependent spectra for the discharges 75223 and 75232.

Comparison between Fig.110 and Fig.111 shows that the outgoing flux of fast particles for the case of higher electron density is lower. This may be due to reduced neutral density in the case with higher electron density. In addition to that in both discharges 75223 and 75232 Fast particle population along sightline 17 coincides with 18th one and may be evidence of loss-region reducing.

In terms of checking of electron density influence on the fast particle spectra and loss regions another measurements were made also for joint operation of ICRF and perpendicularly injecting NBI4 in plasma with Rax = 3.6m B=2.85T magnetic axis position. The time diagram of discharge is shown on Fig.112 and electron density and temperature profiles are shown on Fig.113. The energy of particles injected bi NBI4 was 40 keV and the injected power was 4.7MW, the power of ICRF was 0.3MW.

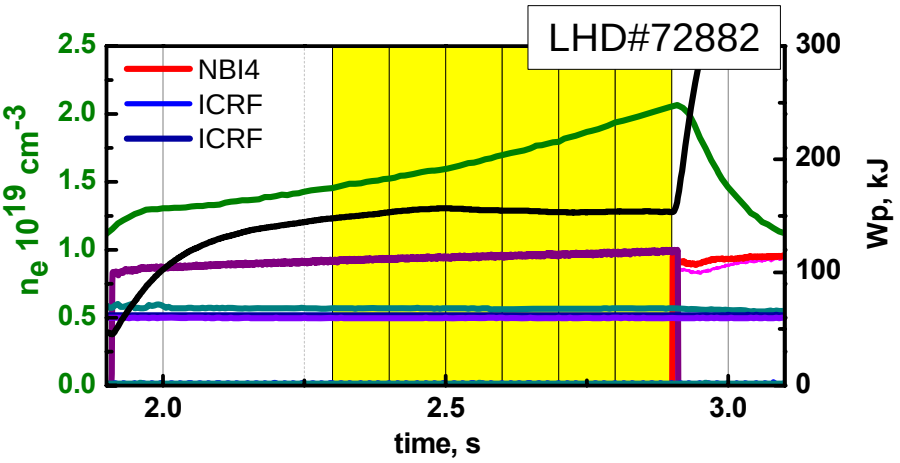

Fig.112 Time diagram of the LHD plasma discharge without ICRF heating.

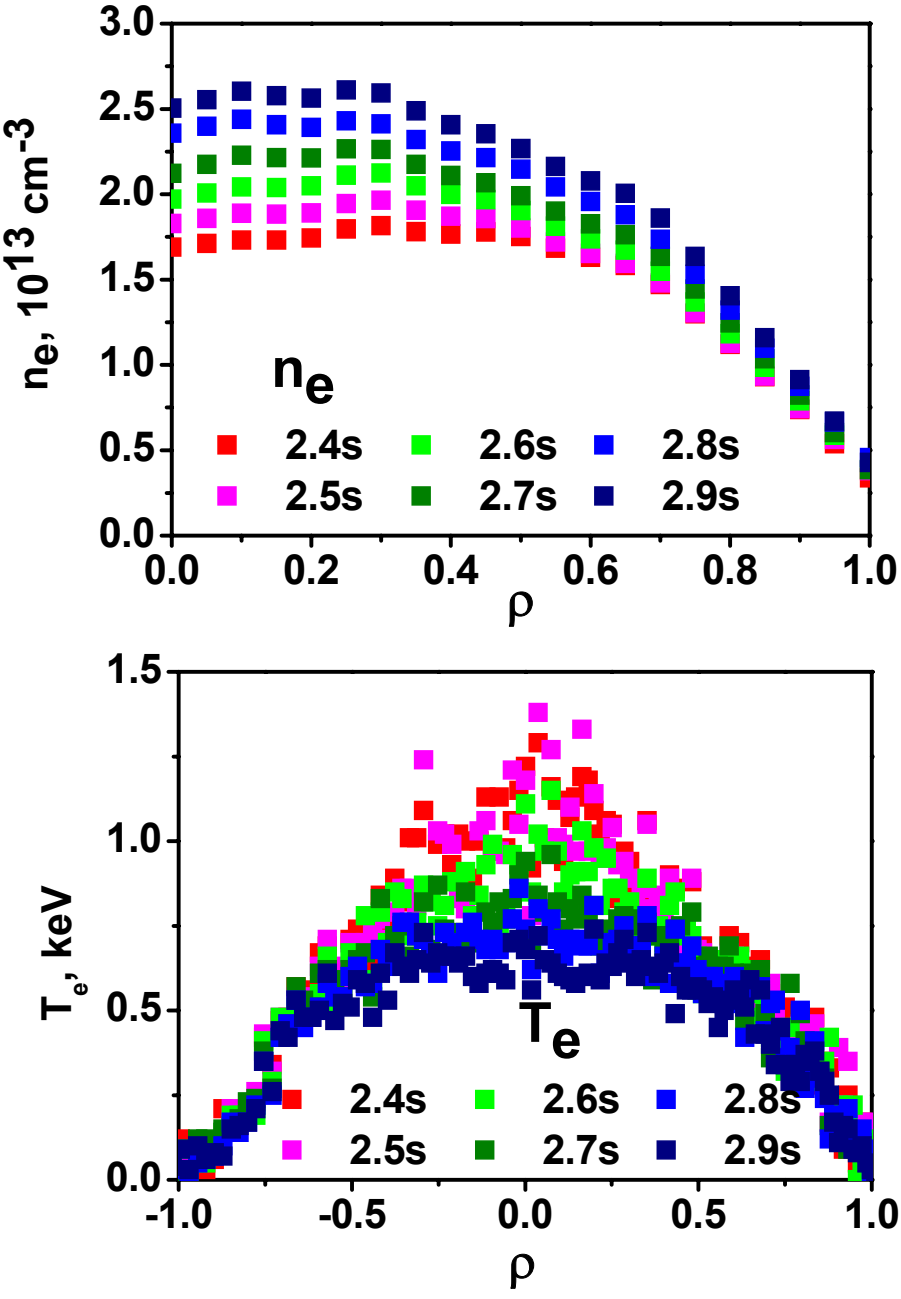

Fig.113 Experimental electron density and temperature profiles for the ShotNo 72882.

Angular distributions of fast particle spectra were restored on the time interval 2.3÷2.9s with 100ms the step Fig.114. As it can be seen during all time intervals the drop of fast particle population still exists. Quantitative spectra along sightlines close to perpendicular directions are shown on Fig.115.

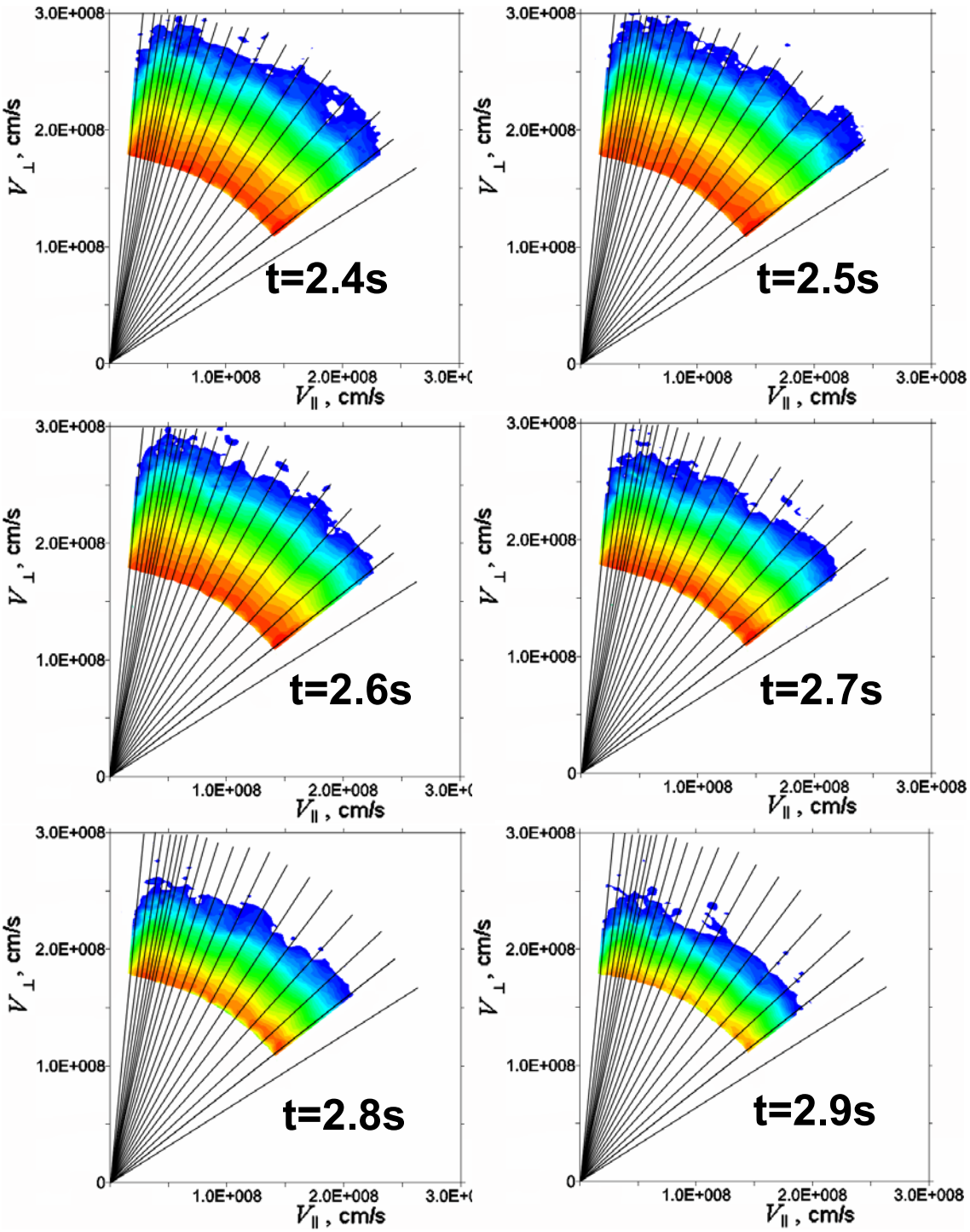

Fig.114 Restored angular dependent spectra for the discharges 75223 and 75232.

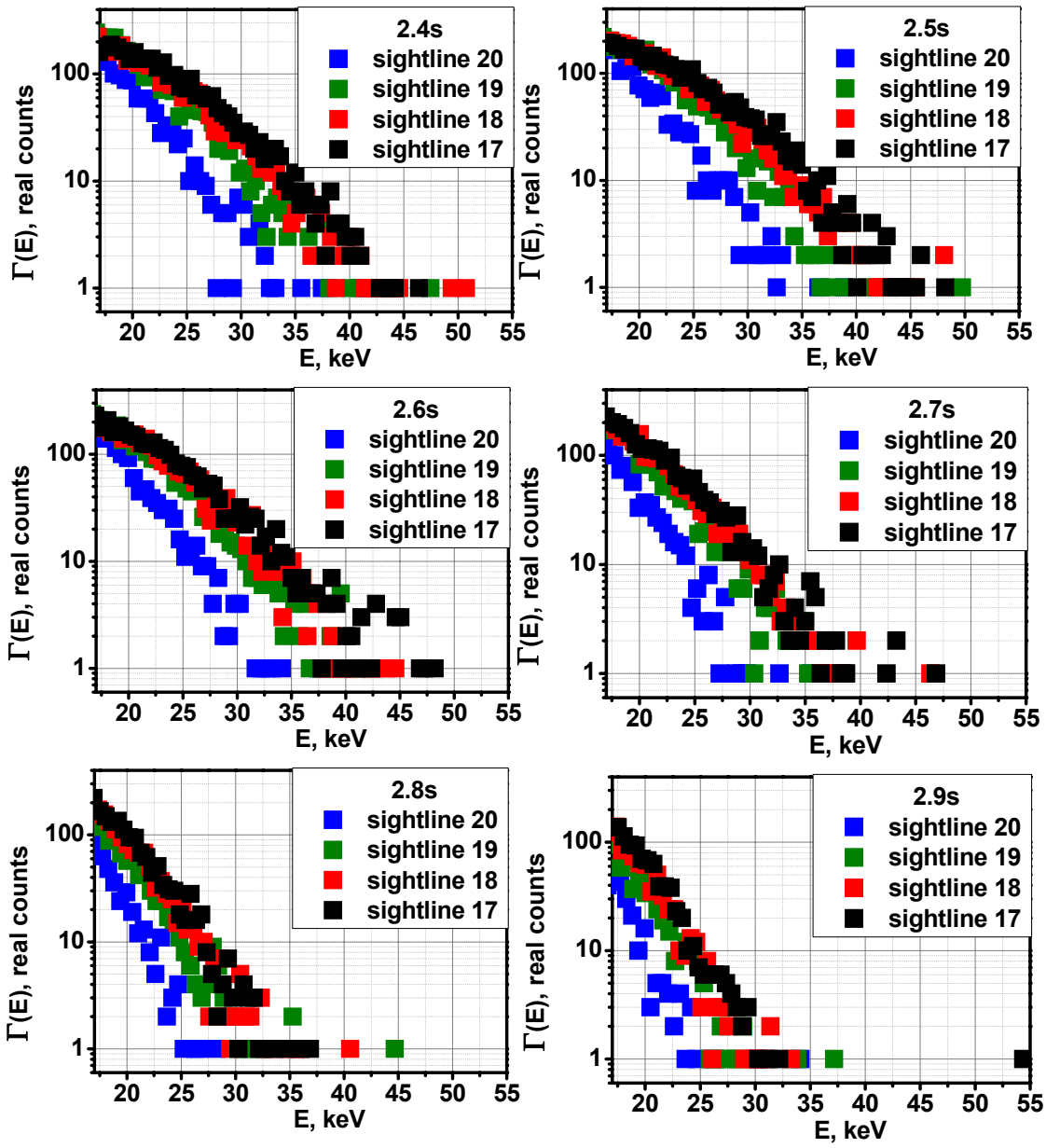

Fig.115 Fast particle spectra for four of the sightlines close to perpendicular direction (sightline 20 is the most perpendicular one) during co-injecting NBI1 operation for three different magnetic field strength values.

As it can be seen from Fig.115 spectrum along the 17th sightline always remains similar to the 18th one during all changes. Thus in the current case the shape of loss region isn't changed with other plasma parameters.

Experimentally measured angular distributions of fast particles for the case of joint operation of NBI4 and ICRF were compared with calculation results of the distribution function (Fig.116) [46].

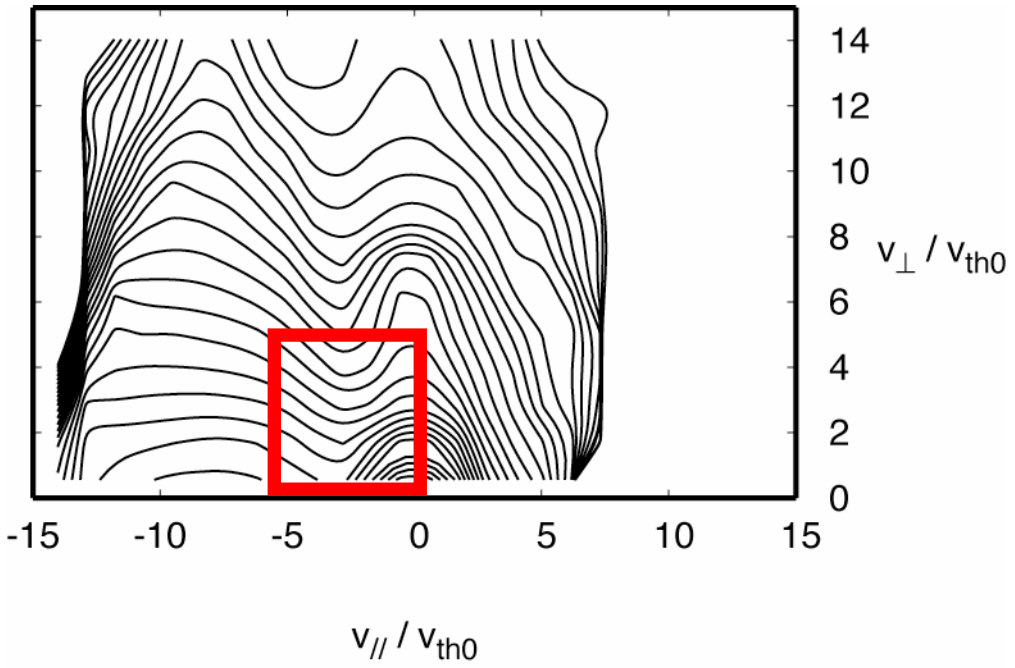

Fig.116 Distribution function of fast particles for the case of NBI4 and ICRF operation. Red square is the region in which experimental data exist.

Red square on Fig.116 is the region in which experimental data exist. It can be seen that there is no drop in the distribution function near the 80º ÷ 85º pitch angle region.

4.2.2 EFFECT OF IMPURITIES ON THE ATTENUATION.

The mean number of ionizations per unit path length λ_{mfp} to be taken into account in (2) during calculation of the atomic flux $\Gamma(E,\vartheta)$ [erg^{-1}s^{-1}] measured by passive diagnostics of escaping high energy neutral particles is:

$$\lambda_{mfp} = \frac{1}{n_e \sigma}, \tag{9}$$

where

$$\sigma = \sum_i \sigma^{(i)}, \tag{10}$$

$\sigma^{(i)}$ is the process taken into account (i.e. charge-exchange, recombination, electron impact ionization, *etc.*)

In this chapter the influence of the attenuation of the emitted from plasma atomic flux on the impurities will be studied. Monograph [45] gives a suitable analytic expression for ionization cross-sections $\sigma_s^{(z)}$(E, n_e,T_e,Z_{eff}) on the impurities for a single-impurity (Z) plasma:

$$\sigma_s^{(Z)}(E,n_e,T_e,Z_{eff}) = \frac{\exp[S_1(E,n_e,T_e)]}{E} * [1+(Z_{eff}-1)S_Z(E,n_e,T_e)] \quad (\times 10^{-16} \quad \text{cm}^{-2}) \tag{11}$$

where

$$S_1 = \sum_i^2 \sum_j^3 \sum_k^2 \{A_{ijk} * (\ln E)^{i-1} [\ln(n/n_0)]^{j-1} (\ln T_e)^{k-1}\} \tag{12}$$

$$S_Z = \sum_i^3 \sum_j^2 \sum_k^2 \{B_{ijk}^{(Z)} * (\ln E)^{i-1} [\ln(n/n_0)]^{j-1} (\ln T_e)^{k-1}\} \tag{13}$$

with E, n_e, T_e expressed in units of keV/u, cm^{-3} and keV, respectively , and n_0=10^{13}cm^{-3}. The function S_1(E, n_e, T_e) together with the E^{-1} factor describes the beam stopping in a pure hydrogenic plasma, while the function (Z_{eff}-1)SZ(E,n_e,T_e) describes the effect of the impurity Z on the beam sopping. Calculations of σ_s have been performed for a pure plasma and for several single-impurity plasmas (with Z=2(He), 6(C) 8(O), and 26(Fe)) by varying E, n_e, T_e and Z_{eff} in the ranges: 100≤E(keV/u)≤10^4, 10^{12}≤n_e(cm^{-3}) ≤10^{15}, 1≤T_e(keV) ≤50, 1<Z_{eff}<Z and 1≤B(T) ≤10.

The data are fitted to Eq.(11) with an overall accuracy of rms = 2% and a maximum deviation of 10%.The fitting coefficients A_{ijk} and $B_{ijk}^{(Z)}$ are given in Table 2 and 3.

Table 2. Values of the coefficients A_{ijk} in Eq.(12).

A_{111}	4.40	A211	2.30×10^{-1}
A_{112}	-2.49×10^{-2}	A212	-1.15×10^{-2}
A_{121}	7.46×10^{-2}	A221	-2.55×10^{-3}
A_{122}	2.27×10^{-3}	A222	-6.20×10^{-4}
A_{131}	3.16×10^{-3}	A231	1.32×10^{-3}
A_{132}	-2.78×10^{-5}	A232	3.38×10^{-5}

Table 3. Values of the coefficients $B_{ijk}^{(Z)}$ in Eq.(13) for He, C, O and Fe impurirties.

$B_{ijk}^{(Z)}$	He	C	O	Fe
B_{111}	-2.36	-1.49	-1.41	-1.03
B_{112}	1.85×10^{-1}	-1.54×10^{-2}	-4.08×10^{-4}	1.06×10^{-1}
B_{121}	-2.50×10^{-1}	-1.19×10^{-1}	-1.08×10^{-1}	-5.58×10^{-2}
B_{122}	-3.81×10^{-2}	-1.50×10^{-2}	-1.38×10^{-2}	-3.72×10^{-3}
B_{211}	8.49×10^{-1}	5.18×10^{-1}	4.77×10^{-1}	3.22×10^{-1}
B_{212}	-4.78×10^{-2}	7.18×10^{-3}	1.57×10^{-3}	-3.75×10^{-2}
B_{221}	6.77×10^{-2}	2.92×10^{-2}	2.59×10^{-2}	1.24×10^{-2}
B_{222}	1.05×10^{-2}	3.66×10^{-3}	3.33×10^{-3}	8.61×10^{-4}
B_{311}	-5.88×10^{-2}	-3.36×10^{-2}	-3.05×10^{-2}	-1.87×10^{-2}
B_{312}	4.34×10^{-3}	3.41×10^{-4}	7.35×10^{-4}	3.53×10^{-3}
B_{321}	-4.48×10^{-3}	-1.79×10^{-3}	-1.57×10^{-3}	-7.43×10^{-4}
B_{322}	-6.76×10^{-4}	-2.04×10^{-4}	-1.86×10^{-4}	-5.12×10^{-5}

For a plasma having an arbitrary mix of N different types of impurities with densities n_q and charges Z_q (q = 1, …, N) the beam stopping cross-section can be represented as the weighted sum of the stopping cross-sections for N reference single-impurity plasmas. In each of these reference plasmas, the electron density and the proton density (including that of deuterium and tritium ions) are the same as in a true plasma. The impurity density, however, is increased in order to satisfy quasi-

neutrality. The weighting function is the electron density n_qZ_q associated with the given impurity (in the true plasma), divided by the sum of these densities. The result is:

$$\sigma_S^{(N)} = \frac{\exp S_1(E, n_e, T_e)}{E} * [1 + \frac{1}{n_e} \sum_q n_q Z_q (Z_q - 1) S_{Z_q}(E, n_e, T_e)] \quad (\times 10^{-16}\ \text{cm}^{-2}) \quad (14)$$

This formula has been tested for a plasma containing He, C, O and Fe impurities over a wide range of relative concentrations, and has been found to be accurate to better than 1%. In particular it reproduces the stopping cross-sections discussed in Section 4 of [45], when E ≥ 100 keV/u.

Current approximations are applicable for completely ionized impurities. The density of every impurity is:

$$n_q = \chi_q k n_e \quad (15)$$

where χ_q is some defined coefficient and k – unknown coefficient.

The equation of plasma quasi-neutrality of plasma can be written as:

$$n_i + (\sum_q Z_q \chi_q) k n_e = n_e \quad (16)$$

and Z_{eff} is:

$$n_i + (\sum_q Z_q^2 \chi_q) k n_e = n_e Z_{eff} \quad (17)$$

By excluding n_i from (16) and (17) the equation for k is obtained:

$$k = \frac{Z_{eff} - 1}{\sum_q \chi_q Z_q (Z_q - 1)} \quad (18)$$

By using (15) and (18) the beam stopping cross-section (14) for a plasma having an arbitrary mix of N different types of impurities can be estimated. In all the following calculations the plasma impurity content was chosen to be with the next χ_q parameters: He : C : O : Fe = 5.0 : 1.5 : 0.5 : 0.05

Calculations were made for plasma with the next parameters:

$$T_e = (T_e(0) - T_{e\_edge})(1 - \rho^{\alpha_0})^{\alpha} + T_{e\_edge} \quad (8)$$

$$n_e = (n_e(0) - n_{e\_edge})(1 - \rho^{\beta_0})^{\beta} + n_{e\_edge}$$

$n_0(0)$ (Fig.93); $T_e(0)$ = 1 keV, T_{e_edge} = 0.1 keV, α_0 = 3, α_0 = 2; $n_{e1}(0)$ = 2x10^{13} cm^{-3}, $n_{e2}(0)$ = 2x10^{13} cm^{-3}, $n_{e3}(0)$ = 2x10^{13} cm^{-3}, $n_{e4}(0)$ = 2x10^{13} cm^{-3}, n_{e_edge}=0.4 x10^{13}cm^{-3}, β_0 = 1.7, β = 1.

Fig.117 illustrates the influence of varied Z_{eff} on the spectra of fast particles emitted from plasma for four cases of electron density and Fig.118 illustrates the influence of electron density on the spectra for different cases of Z_{eff}.

It can be seen that the shape of spectra isn't changed in the high energy region. The Z_{eff} and electron density slightly influences only on the relative value of spectra. Discrepancy in the low energy region appears due to the an-applicability of the approximating formula to the low energy region.

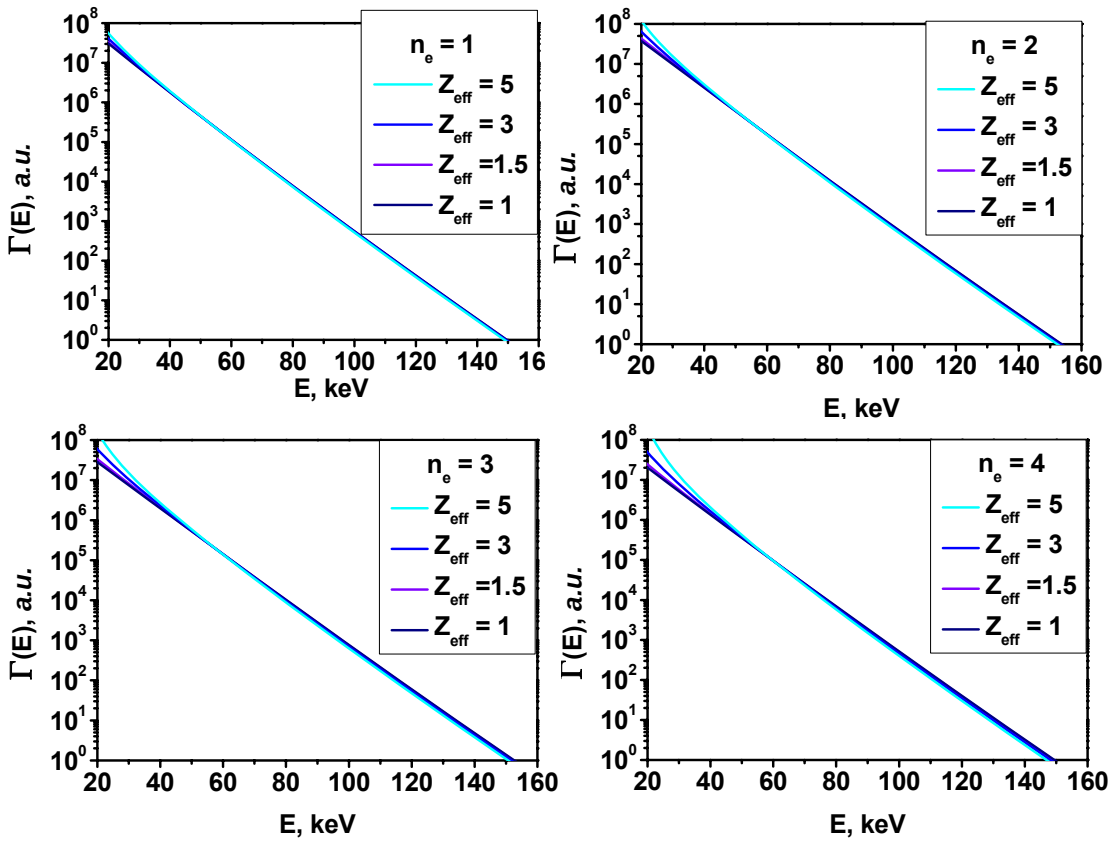

Fig.117 Influence of varied Z_{eff} on the spectra of fast particles emitted from plasma for four cases of electron density.

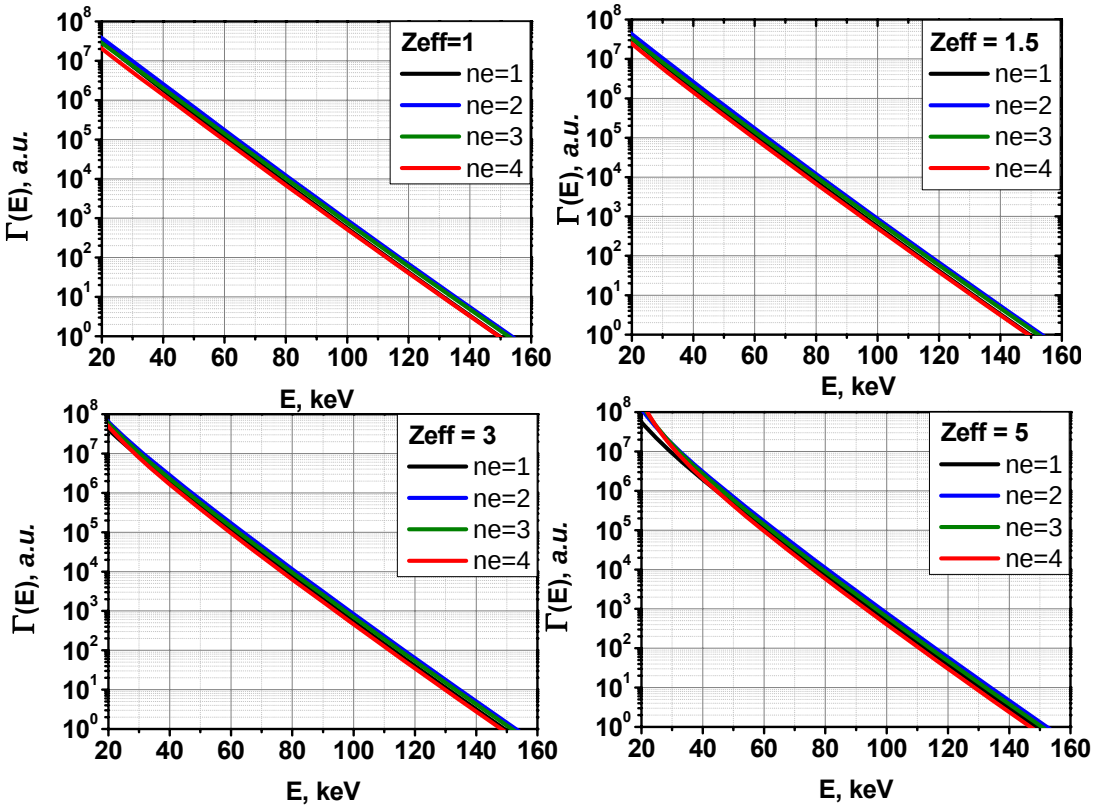

Fig.118 Influence of electron density on the spectra for different cases of Z_{eff}.

4.2.2 Brief Summary

- Electron density growth doesn't lead to significant change of fast particle spectra shape according to calculation results. Only relative values of spectra are changed.
- Electron density growth leads to reducing of the fast particle flux along all directions due to reducing of the neutral density.
- Experimental data for ICRF and perpendicular NBI4 demonstrate the drop of fast particle in the pitch angle region of 80º ÷ 85º. Such a drop can't be observed in calculation results.
- In the case of plasma with Rax = 3.6m B=2.85T magnetic axis position the region of losses may be changed during by density variation may be due to electric field change.
- In the case of plasma with Rax = 3.6m B=1.375T magnetic axis position the region of losses remains the same during density variation.
- Calculations with Z_{eff} varying demonstrate that it doesn't influence on the shape of fast particle spectra in high energy range.

5. CONCLUSION

The novel Angular-Resolved Multi-Sightline Neutral Particle Analyzer (ARMS-NPA) for fast ion distribution studies has been designed, developed installed and successful measurements have been made on LHD in different plasma heating conditions. The main advantage of this novel measurement concept is the possibility to make time, energy, and angle-resolved measurements of escaping charge exchange neutral particle fluxes in a single plasma discharge. This unique feature makes the new diagnostic a very helpful and powerful tool intended to contribute to the understanding of fast ion behavior in a complex helical plasma geometry like the one of LHD.

This new informative diagnostic of kinetic energy distributions of neutral atoms escaping from magnetically confined plasma can be used in modern controlled fusion experiments as a comprehensive method to investigate the anisotropic ion distribution function and its evolution due to the application of various plasma heating schemes. This is especially important towards the achievement of the ignition criterion and a steady state reactor. The ion distribution function reflects the kinetic effects, the single particle confinement properties depending on the particular magnetic configuration, the finite β effects such as MHD induced fast ion losses, radial electric field effects, etc. The nuclear fusion reaction rate is determined by the ion distribution and thus its studies at suprathermal energies near the rate coefficient curve maximum are of primary importance in present day experiments when plasma parameters approach fusion-relevant values.

Among the NPA diagnostics used on tokamaks only few can make angular resolved measurements of fast particles along several sightlines simultaneously. For example one of NPA system used on TFTR operates six sightlines in equatorial plane which are capable of being scanned in both toroidal and vertical direction. Solid state neutral particle analyzer array on NSTX consists only of four viewing chords. Multi-channel SDNPA on LHD can scan plasma by six sightlines. Thus in the light of multi-sightline NPA systems available to make angular-resolved measurements of fast particles a new ARMS-NPA Diagnostic with its 20 channels of scanning is going to become a powerful tool for fast particles study. AXUV detector has been successfully used for the first time for fast particles measurements in plasma devices.

Fast particle measurements by the novel ARMS-NPA were made in the wide variety of plasma parameters and heating regimes such as NBI, ICRF and ECH. In the majority of analyzed experimental data the possible presence of the loss-cone region

has been found in the 80º-85º pitch-angle range. In all cases with positive or negative magnetic field direction, inward or outward magnetic axis shift, co- or counter- NBI injection, with or without ICRF heating the significant reducing of the fast particle flux was observed at the sightlines close to perpendicular direction at 80º÷85º pitch-angle range that may be due to the presence of loss-cone in this region.

It was found that switching on of the ECH may significantly influence on the angular distribution of fast particles. ECH may cause the electron temperature profile to change that leads to the change of electric field and the loss-cone reducing near θ = 85º pitch angle range. Peaked electron temperature profile is more favorable for loss-cone suppression. Thus ECH may become a powerful tool for suppression of the loss-cones and for improving fast particles confinement.

Since the naturally occurring charge exchange neutral particle source is not localized in contrast to the diagnostic neutral beam or pellet charge exchange methods, the correct interpretation of such measurements in a complex toroidal asymmetric geometry requires a careful numerical modeling of the neutral flux formation and the knowledge of the charge-exchange (CX) target distributions, relevant cross sections, and the magnetic surface structure. A model for the particle flux of neutrals, escaping from plasma column due to CX has been derived and applied for the LHD geometry. It was shown that the chord superposition effect on the relative values of distribution curves obtained in different geometry should be accounted for in data interpretation. However after subtracting of the geometry effect from experimental data, the drop of fast particle population at perpendicular sightlines still remained. Same time it was shown that magnetic axis shift effect in experiment is slightly larger for Rax = 3.5m magnetic axis configuration rather Rax = 3.6m configuration than in calculations results, therefore inward shift is favorable for fast particle confinement.

Bibliography

[1] P.R. Goncharov *et al.*, Rev. Sci. Instrum., **77**, 10F119-1 (2006)

[2] T. Ozaki *et al.*, Rev. Sci. Instrum., **71**, 2698 (2000)

[3] J.F. Lyon *et al.*, Rev. Sci. Instrum., **74**, 1873 (2003).

[4] K. Khlopenkov and S.Sudo , Plasma Phys. Control. Fusion **43** 1547 (2001)

[5] R. Bartiromo, G. Bracco *et al.*, Rev. Sci. Instrum., **58** 788 (1987).

[6] S.S. Medley *et al.*, Rev. Sci. Instrum., **74**(3), 1896 (2003)

[7] K. Shinohara *et al.*, Rev. Sci. Instrum., **75**, 3640 (2004).

[8] S.S. Medley and A.L. Roquemore, Rev. Sci. Instrum., **69**, 2651 (1998).

[9] ITER design description document (DDD), Neutral particle analyzers, WBS 5.5.E.08, RV4, 26 Nov.1996

[10] H. Matsushita *et al.*, Rev. Sci. Instrum., **75**, 3607 (2004)

[11] K. Matsuoka *et al.*, *Plasma Physics and Controlled Nuclear Fusion Research 1998*, Proceedings 12th International Conference Nice, 1988, (IAEA, Vienna, 1989), Vol. 2, p. 411.

[12] K. Nishimura *et al.*, Fusion Technol. **17**, 86 (1990)

[13] T. Obiki *et al*., Nucl. Fusion, **41**, 833 (2001).

[14] M. Kaneko *et. al.*, Fusion Science and Technology **50**, 428 (2006)

[15] M.R. Toutnianski *et al.*, *31st EPS Conference on Plasma Phys. London, 28 June - 2 July 2004 ECA Vol.**28G**, P-4.193 (2004)*

[16] V. Tang *et al.*, Rev. Sci. Instrum., **77**, 083501 (2006)

[17] R.L. Boivin and M. Koltonyuk, Rev. Sci. Instrum., **68** (1), 982 (1997)

[18] A.G. Alekseyev *et al.*, Rev. Sci. Instrum., **74**, 1905 (2003).

[19] M. Isobe *et al.*, Rev. Sci. Instrum., **72**, 611 (2003).

[20] A.V. Krasilnikov *et al*, Nucl.Fusion, **39,** 1111 (1999).

[21] M. Ishikawa *et al.*, Rev. Sci. Instrum., **75**, 3643 (2004).

[22] A. V. Krasilnikov *et al.*, Rev. Sci. Instrum. **68**, 1720 (1997).

[23] A. V. Krasilnikov *et al.*, IEEE Trans. Nucl. Sci. **45**, 385 (1998).

[24] A. V. Krasilnikov *et al.*, J. Plasma Fusion Res. **75**, 967 (1999).

[25] T.Kamimura et. al, "Numerical Studies of Particle Drift Orbits in Helical System" private communication (1987).

[26] T. Watanabe, Y. Matsumoto *et al*, Nucl.Fusion, **46,** 291 (2006)

[27] S.P. Hirshman, J.C. Whitson, Phys. Fluids, **26**, 3553 (1983)

[28] http://www.ird-inc.com/axuvarr.html

[29] E.A.Veshchev, T.Ozaki *et al.*, Rev. Sci. Instrum., **77**, 10F129 (2006).

[30] J. F. Ziegler, *Handbook of Stopping Cross-Sections for Energetic Ions in all Elements* (Pergamon, New York, 1980).

[31] J. F. Ziegler, J. P. Biersack, and U. Littmark, *The Stopping and Range of Ions in Solids* (Pergamon, New York, 1985).

[32] H.Sanuki, J.Todoroki and T.Kamimura. Phys. Fluids B **2** (9), 2155 (1990)

[33] S.Murakami Fusion Sci. Tech., **46**, No. 2, pp. 241-247 (2004)

[34] E.A.Veshchev, P.R. Concharov *et al.*, Rev. Sci. Instrum., **77**, 10F116 (2006).

[35] Yu.N. Dnestrovskij *et al.*, Nucl.Fusion, **19**, 293 (1979).

[36] I.H. Hutchinson, *Principles of plasma diagnostics*, *2nd ed.*, Cambridge University Press (2002).

[37] J.M. Fontdecaba *et al.*, Fusion Sci. and Technol., **46**, 271 (2004).

[38] P.R. Goncharov, *et al.*, Proc. 31st EPS Conference on Plasma Physics and Controlled Fusion, ECA vol. **28G**, P-5.112 (London, 2004).

[39] P.R. Goncharov *et al.*, J. Plasma Fusion Res. Series, **6**, 314 (2003).

[40] M. Freeman, S. Katz, J. Opt. Soc. Amer., **50**, 826 (1960).

[41] V.V. Pickalov, T.S. Melnikova, *Plasma Tomography*, Nauka, Novosibirsk (1995).

[42] C.F. Barnett, ed., *Atomic Data for Fusion*, ORNL-6086, USA (1990).

[43] T.H. Stix, Nucl.Fusion, **15**, 737 (1975).

[44] J.G.. Cordey, M.J. Houghton, Nucl. Fusion, **13**, 215 (1973).

[45] R.K. Janev, C.D. Boley *et.al.*, Nucl. Fusion, Vol.**29**, No.12 2125 (1989).

[46] S.Murakami, private communication.

[47] T.Ido, private communication.

ACKNOWLEDGEMENTS

In my opinion this is the most important part of Doctoral Thesis because on these pages I would like to express my thanks to all the people who helped me and made this Thesis possible.

I'm really appreciated to my scientific adviser Prof.Sudo, who invited me to and let me to take a closer look at such an amazing country as JAPAN. I really like people with self-confident positive and optimistic way of thinking and I am really glad that such a person was my scientific advisor Prof.Sudo. Along with plasma research I was growing up these strains in myself and Prof.Sudo was always the good example for me.

I would like to tell the sincerest words of thanks to Prof.Ozaki, to his splendid idea which he presented to me and which we realized during my Ph.D course – the idea about creation of such an interesting diagnostic! The great experimental experience of Prof.Ozaki helped to avoid many mistakes in creating of the novel diagnostics and to prepare the unique powerful tool for plasma research. I really respect Prof.Ozaki for his patience and self-restrain. I will always align myself on Prof.Ozaki in these strains. It was a pleasure to work together.

I have too many words of gratitude to Dr.Goncharov Pavel, for his help and support of me any time. Dr.Goncharov is a very intelligent and interesting person. I was always interested in his opinion and always consulted with him. We had many interesting discussions from physics to literature. Neatness, kindness and modesty these are basic strains of Dr.Goncharov which I learnt and still continue to develop in myself.

I am thankful to Dr.Tamura Naoki for his help and advices.

My appreciations to committee members Prof.Sanuki, Prof.Okamura, Prof.Murakami for their time patience and the ability to teach and help. Their comments and advices were very helpful and significantly improved my Thesis.

My special thanks to Prof.Motojima for the opportunity to be proud that I work on such a splendid device like LHD. I will always remember the Kashikojima seminars, it was unforgotten and enjoyable time together with a good opportunity to practice in making presentations.

The significant help in experiment preparations was provided by LHD experimental group and LHD technical staff. I was really impressed by their neat and well coordinated work. My greatest gratitude to them.

My special thanks to my parents and relatives who always supported me. I could feel their love and care for the whole time of my Thesis preparations.

It would be difficult to survive without my numerous friends. And I will always keep in my heart all of you. Thank you so much!

I would like to extend my gratitude to Prof. B.V.Kuteev and Dr. N.A.Kirneva for their faith in me.

And finally, last but not least my greatest thanks to my wife. Her kindness, comprehension and womanhood helped me so much! Such a care allowed me to be completely absorbed in my Thesis preparations.

Actually my final gratitude is to my life and to the God. I'm really happy that I can live such a life, can meet such wonderful people! Everybody was my teacher and will always be. It is really difficult for me to express my own gratitude personally. At least I am happy, that I've made it on these couple pages. But still, all theses gratitude words can not express the whole deepness of my feelings to all of you. You have occupied the space in my heart forever. Thank you very much!

Evgeny Veshchev